BOSTON UNIVERSITY

GRADUATE SCHOOL OF ARTS AND SCIENCES

Dissertation

PRECISE STUDY OF THE ATMOSPHERIC NEUTRINO OSCILLATION PATTERN USING SUPER-KAMIOKANDE I AND II

by

FANNY MAUDE DUFOUR

B.S., Université libre de Bruxelles, 2003

Submitted in partial fulfillment of the

requirements for the degree of

Doctor of Philosophy

2009

Approved by

First Reader

Edward T. Kearns, Ph.D.
Professor of Physics

Second Reader

Tulika Bose, Ph.D.
Assistant Professor of Physics

Acknowledgments

I would like to thank my parents and my brother for their support, and for not complaining too much about the fact that I came to study particle physics in the US, on a detector located in Japan, while I was born 30 km away from CERN. Then of course I want to thank Vishal for his love and endless support.

The BU physics grad students made life in Boston real treat. The Friday nights at The Other Side, the parties at Silvia, Jason, Claudio and countless others, and the summer trips to Singing Beach; all these moments were vital to my mental health. I also want to thank my friends in Switzerland, Anouk, Manu et les autres.. pour vos emails, vos lettres, votre accueil pendant mes vacances, et le fait qu'après onze ans d'absence nous sommes toujours si proches.

My friends on the second floor of PRB deserve a special acknowledgment: Jason for making my cubicle less dull once in a while, Jen for teaching me emacs keyboard shortcuts and how to knit, Mike for teaching me the rules of baseball during the 2003 post-season so that I could enjoy 2004, Dan for hanging out at ERC in the morning, Wei for giving me PC reduction, and Brian, for making PRB 268 less lonely after everybody had moved to the lab or to Geneva. Thank you to Mirtha Cabello, superwoman to all grad students in Physics at BU.

Naturally, not much of this thesis would have been achieved without the help of my advisor, Ed Kearns. Thanks for teaching us how to present good talks and teaching all of us to become better physicists. Many thanks to my committee members for their time and comments: Tulika Bose, Lee Roberts, Sheldon Glashow and Anders Sandvik. Finally, I wanted to thank our colleagues in the US and in Japan, Kate Scholberg, Roger Wendell, Naho Tanimoto, Shigetaka Moriyama, Takaaki Kajita for their help inside and outside Mozumi. And a special thanks to Piotr for taking over PC reduction!

PRECISE STUDY OF THE ATMOSPHERIC NEUTRINO OSCILLATION PATTERN USING SUPER-KAMIOKANDE I AND II

(Order No.   )

FANNY DUFOUR

Boston University Graduate School of Arts and Sciences, 2009

Major Professor: Edward T. Kearns, Professor of Physics

ABSTRACT

Neutrino oscillation arises because the mass eigenstates of neutrinos are not identical to the flavor eigenstates, and it is described by the PMNS (Pontecorvo, Maki, Nakagawa and Sakata) flavor mixing matrix. This matrix contains 6 parameters: 3 angles, 2 mass splittings and one CP violating phase. Using the atmospheric neutrino data collected by the Super-Kamiokande water Cherenkov detector, we can measure two of these parameters, Δm^2_{23} and $\sin^2 2\theta_{23}$, which govern the oscillation of $\nu_\mu \rightarrow \nu_\tau$.

The L/E analysis studies the ratio of flight length (L) to energy (E) and is the only analysis which is able to resolve the expected oscillatory pattern of the survival probability: $P(\nu_\mu \rightarrow \nu_\mu) = 1 - \sin^2(2\theta) \times \sin^2\left(1.27 \times \Delta m^2 \frac{L(km)}{E(GeV)}\right)$. To observe this oscillation pattern, we divide the L/E distribution of muon neutrino data by a normalized unoscillated set of Monte Carlo. Events used in this analysis need good flight length and energy resolution, therefore strict resolution cuts are applied. Hence, the data sample is smaller than the sample used in the other Super-Kamiokande analysis [1]. Despite the smaller sample, the L/E analysis gives a stronger constraint on Δm^2_{23}.

This thesis covers the L/E analysis of the Super-Kamiokande atmospheric data collected during the Super-Kamiokande I (SK1: 1996-2001, 1489 days) and Super-Kamiokande II (SK2: 2003-2005, 804 days) data-taking periods. The final values of the oscillation parameters for the combined SK1+SK2 datasets, at 90% confidence level, are $\sin^2 2\theta_{23} > 0.94$ and $1.85 \times 10^{-3}\ eV^2 < \Delta m^2_{23} < 2.65 \times 10^{-3}\ eV^2$. The χ^2 obtained

with the oscillation hypothesis is lower than when we assume other models like neutrino decay (3.7σ) or neutrino decoherence (4.7σ).

A significant part of this work was the improvement of the partially contained (PC) event sample. This sample consists of neutrino events in which the outgoing charged lepton exits the inner detector and deposits energy in the outer detector. These events are very valuable to the L/E analysis because of their good flight length resolution. The selection of PC events was improved from an 85% selection efficiency to a 97% efficiency for the Super-Kamiokande III (SK3: 2006-2008, 526 days) dataset which will be used in future analyses.

Preface

About sixty billion through one's thumb every second.

The history of the solar neutrino problem is one of the most inspiring episodes of particle physics. It is the story of a theorist, John Bahcall, an experimentalist Ray Davis and the Homestake experiment which had been off by a factor of three for twenty-four years. For twenty-four years, theorists and experimentalists worked to resolve this discrepancy. The physics community considered that getting as close as a factor of three was an achievement in itself, given the difficulty of the task. The factor of three was probably just a little fluke somewhere. But both protagonists were convinced that they were exactly right, not right up to a little fluke! The work continued until the idea of neutrino oscillation presented by Pontecorvo, Maki, Nakagawa and Sakata [2, 3] was being given a second chance. It allowed both the solar neutrino flux theoretical calculation and the observation to be correct at the same time.

The Kamiokande experiment was first designed to look for proton decay. As you well know, proton decay was never found. But the solar neutrino flux was measured and was consistent with the Homestake experiment result. In addition, the atmospheric neutrino flux was also measured, and as in the case of the solar neutrino flux, the theory and the measurement were off by some factor. The neutrino oscillation model had just been given another push.

In order to try to solve once and for all this discrepancy, Super-Kamiokande was designed, and started operating in 1996. Two years later, neutrino oscillation was discovered in both solar and atmospheric neutrino. The thirty years old disagreement between a theorist and an experimentalist had produced two winners, and an inspiring story about patience and hard work to the freshman physics student that I was then.

Contents

List of Tables

List of Figures

List of Abbreviations

ADC . . . . . . Analog to Digital Converter

ATM . . . . . . Analog Timing Module

BG . . . . . . Background

CC . . . . . . Charged Current

CCD . . . . . . Charge-Coupled Device

CCQE . . . . . . Charged Current Quasi-Elastic

CL . . . . . . Confidence Level

DAQ . . . . . . Data Acquisition

DIS . . . . . . Deep Inelastic Scattering

EM . . . . . . Electromagnetism

FRP . . . . . . Fiber-Reinforced Plastic

GONG . . . . . . GO-NoGo

GUT . . . . . . Grand Unified Theory

ID . . . . . . Inner Detector

IMB . . . . . . Irvine Michigan Brookhaven

KAMLAND . . . . . . Kamioka Liquid Scintillator Anti-Neutrino Detector

LHC . . . . . . Large Hadron Collider

LINAC . . . . . . Linear Accelerator

MC . . . . . . Monte Carlo

MS-fit . . . . . . Muon-Shower Fitter

NC . . . . . . Neutral Current

OD . . . . . . Outer Detector

PDF . . . . . . Probability Density Function

PE . . . . . . Photoelectrons

PID . . . . . . Particle identification

PMT .... Photomultiplier tube

QAC .... Charge-to-Analog Converter

QE .... Quasi-Elastic

QTC .... Charge-to-Time Converter

SK .... Super-Kamiokande

SK1 .... Super-Kamiokande I

SK2 .... Super-Kamiokande II

SK3 .... Super-Kamiokande III

SM .... Standard Model

SNO .... Sudbury Neutrino Observatory

Super-K .... Super-Kamiokande

TAC .... Time-to-Analog Converter

TDC .... Time-to-Digital Converter

TKO .... Tristan KEK Online

VME .... Versa Module Europa

Chapter 1

Introduction

The neutrino was first introduced by Wolfgang Pauli in 1930 [7] to explain the continuous β decay ($n \rightarrow p + e^- + \nu$) spectrum and to conserve energy and momentum. When the energy of the outgoing electron is measured, the result is a continuous spectrum. This result would not conserve energy and momentum if β decay were a two-body decay. Pauli's solution was to introduce a nearly massless neutral particle to make β decay a three-body decay. Pauli announced his idea in a letter and a translation of his letter is shown in Fig. 1.1.

Two decades after this first proposal, in 1956, Reines and Cowan [8] were able to observe neutrinos for the first time through an inverse β decay process: $\overline{\nu_e} + p \rightarrow n + e^+$. Ten years later, in 1962, Lederman, Schwartz and Steinberger [9] discovered the muon neutrino, through the decay of the pion ($\pi \rightarrow \mu + \nu_\mu$). And finally in 2000 at Fermilab, the expected τ neutrino was observed by the DONUT experiment [10], 25 years after the discovery of the τ lepton.

In the 1970's, the Homestake experiment [11] measured the solar neutrino flux and its result disagreed with the solar neutrino flux calculation done by John Bahcall [12]. This was called the "solar neutrino problem" and it was the first hint that neutrinos might oscillate, as proposed earlier by Maki, Nakagawa and Sakata in 1962 [2] and Pontecorvo in 1968 [3].

Dear Radioactive Ladies and Gentlemen,

As the bearer of these lines, to whom I graciously ask you to listen, will explain to you in more detail, how because of the "wrong" statistics of the N and Li6 nuclei and the continuous beta spectrum, I have hit upon a desperate remedy to save the "exchange theorem" of statistics and the law of conservation of energy. Namely, the possibility that there could exist in the nuclei electrically neutral particles, that I wish to call neutrons, which have spin 1/2 and obey the exclusion principle and which further differ from light quanta in that they do not travel with the velocity of light. The mass of the neutrons should be of the same order of magnitude as the electron mass and in any event not larger than 0.01 proton masses. The continuous beta spectrum would then become understandable by the assumption that in beta decay a neutron is emitted in addition to the electron such that the sum of the energies of the neutron and the electron is constant...

I agree that my remedy could seem incredible because one should have seen these neutrons much earlier if they really exist. But only the one who dare can win and the difficult situation, due to the continuous structure of the beta spectrum, is lighted by a remark of my honoured predecessor, Mr Debye, who told me recently in Bruxelles: "Oh, It's well better not to think about this at all, like new taxes". From now on, every solution to the issue must be discussed. Thus, dear radioactive people, look and judge.

Unfortunately, I cannot appear in Tubingen personally since I am indispensable here in Zurich because of a ball on the night of 6/7 December. With my best regards to you, and also to Mr Back.

Your humble servant,

W. Pauli

Figure 1.1: Translation of Pauli's famous letter about his proposal of neutrinos (called neutrons in the letter) [7]

In the 1980's several experiments were built to study solar and atmospheric neutrinos. Kamiokande [13] in Japan, and IMB [14] in the United States. In addition studying solar and atmospheric neutrinos, both detectors were able to observe neutrinos coming from the supernova SN1987A. These neutrinos are the only extra-galactic neutrinos observed so far.

In 1998, when the Super-Kamiokande collaboration presented its atmospheric neutrino data analysis showing a deficit of upward going muon neutrinos, the physics com-

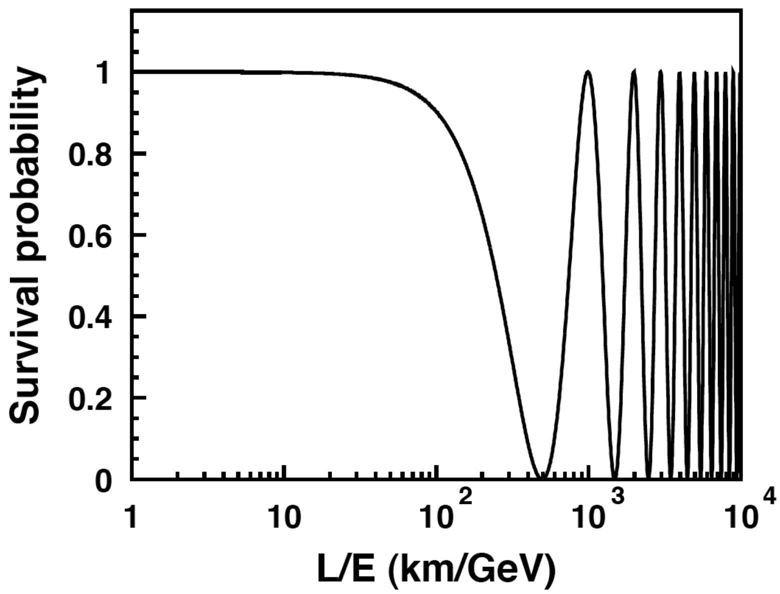

Figure 1.2: Survival probability of $\nu_\mu \rightarrow \nu_\mu$, without any detector effect as a function of L/E.

munity was convinced that neutrino oscillation was the solution to the “solar neutrino problem,” and explained the atmospheric neutrino data.

However, at this point, nobody had seen the oscillatory pattern predicted by the theory. Only a deficit of upward-going neutrinos was observed and other theories like neutrino decay or neutrino decoherence could explain the atmospheric neutrino data.

In the two flavor approximation, the survival probability of the muon neutrino is written as: $P(\nu_\mu \rightarrow \nu_\mu) = 1 - \sin^2(2\theta_{23}) \times \sin^2\left(1.27 \times \Delta m^2_{23} \times \frac{L(km)}{E(GeV)}\right)$ and is shown in Fig. 1.2.

Atmospheric neutrinos have a wide range of energies (E), from a few MeV to several GeV, and a wide range of flight lengths (L) from about 10 km for downward-going neutrinos to about 10000 km for upward-going neutrinos. Thanks to these wide ranges in L and E, we have access to neutrinos with a wide range of L/E values. Using atmospheric muon neutrinos collected by the Super-Kamiokande detector, we can therefore directly observe the oscillatory pattern of survival probability as a function of L/E as shown in Fig. 1.2.

Because the energy and flight length resolutions are not perfect, the resulting L/E resolution only allows us to see the first minimum in the survival probability and the rise after this minimum before the oscillation pattern is no longer distinguishable and only the average value of the survival probability is observed. The position of the minimum is a direct measurement of Δm^2_{23}, and the level at which the probability averages out is a measurement of $\sin^2(2\theta_{23})$.

Chapter 2

Neutrino Theory

For many years, neutrinos were assumed to be massless, but the observation of atmospheric muon neutrino disappearance by the Super-Kamiokande collaboration in 1998 [1] changed the game. Physicists were now seeing both atmospheric and solar neutrinos behaving differently from what was expected. Neutrino oscillations could explain both the solar and the atmospheric data, but these oscillations required neutrinos to be massive, and that the mass eigenstates be different from the flavor eigenstates.

2.1 The mass of the neutrino

After the discovery of muon neutrino disappearance by the Super-Kamiokande experiment, the most widely accepted explanation was neutrino oscillation. Since oscillation is possible only with massive neutrino, it is interesting to study how the neutrino mass term is introduced in the Standard Model. Usually, in the Standard Model, spin-1/2 particles acquire their mass through interaction with the Higgs background field, as shown in Fig. 2.1.

These mass terms are called Dirac mass terms and are presented in Eq. 2.1. One of their characteristics is that they change the handedness of particles; a left-handed electron becomes a right-handed electron through its interaction with the Higgs field [15]:

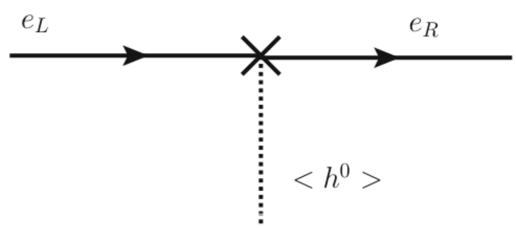

Figure 2.1: Dirac mass term for an electron.

$$\mathcal{L}_{fermions} = -G_e \left[(\overline{\nu_e}, \overline{e})_L \begin{pmatrix} h^+ \\ h^0 \end{pmatrix} e_R + \overline{e_R}(h^-, \overline{h^0}) \begin{pmatrix} \nu_e \\ e \end{pmatrix}_L \right], \tag{2.1}$$

where G_e is an arbitrary Yukawa coupling that can be chosen to be $m_e = \frac{G_e v}{\sqrt{2}}$, $(\overline{\nu_e}, \overline{e})_L$, is the weak isospin doublet, h is the Higgs doublet and e_r an isospin singlet. For massless neutrinos, the Higgs doublet is rewritten as:

$$h = \sqrt{\frac{1}{2}} \begin{pmatrix} 0 \\ v + h(x) \end{pmatrix}, \tag{2.2}$$

where v is the non-zero vacuum expectation value of the Higgs field. In the Standard Model, the electron mass comes from the Yukawa coupling of the electron to the Higgs vacuum expectation.

Dirac mass terms conserve electric charge, and they conserve lepton number; a particle does not become an anti-particle when it interacts with the vacuum expectation of the Higgs field $< h^0 >= \frac{v}{\sqrt{2}}$. Dirac particles have four states, for example: e_L, $\overline{e_R}$, e_R and $\overline{e_L}$. Only the first two states interact weakly and each are part of a weak isospin doublet with its neutrino counterpart. The last two states are weak isospin singlets. The Dirac states of leptons are summarized in Table 2.1.

So far we have seen only the left-handed neutrino and the right-handed anti-neutrino. If neutrinos behave like all other spin-1/2 particles and are Dirac particles then two new states need to be introduced: the right-handed neutrino and the left-handed anti-

Particle Number	Handedness	Particle States	Weak Isospin Charge	Electric Charge
$+1$	L	e_L	$-1/2$	-1
$+1$	L	ν_L	$+1/2$	0
-1	R	$\overline{e_R}$	$+1/2$	$+1$
-1	R	$\overline{\nu_R}$	$-1/2$	0
+1	R	e_R	0	-1
-1	L	$\overline{e_L}$	0	+1
+1	R	ν_R	0	0
-1	L	$\overline{\nu_L}$	0	0

Table 2.1: Dirac lepton states

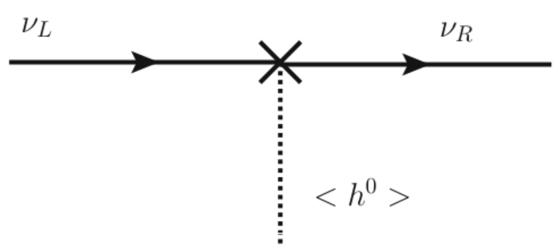

Figure 2.2: Dirac mass term for neutrino.

neutrino. These two states are called sterile, as they do not even interact weakly. In that case the neutrinos would get their mass through the usual Higgs mechanism as shown in Fig. 2.2. We use the process which gives mass to the upper member of the quark doublet. With Dirac masses, nothing explains why the masses of the neutrinos are so much smaller than the masses of their associated leptons.

As mentioned earlier, we have so far only observed two states of neutrinos, not four. If we do not want to introduce the two extra states, then neutrinos cannot have Dirac mass terms as this would violate the conservation of lepton number assumed for such terms. But if we allow lepton number violation, the 2-state neutrinos can acquire mass through the interaction with the Higgs background field as shown in Fig. 2.3. These are Majorana mass terms and they change both handedness and lepton number. Since the lagrangian density has units of E^4, the fermion fields of $E^{3/2}$ and the Higgs field of E^1,

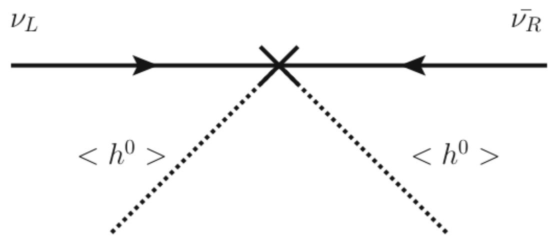

Figure 2.3: Majorana mass term for neutrino.

we can see that an energy scale needs to be introduced. Therefore, this is an effective theory.

The most widely accepted explanation for this difference in masses is the seesaw mechanism [16–19]. In that case, neutrinos have both Dirac and Majorana mass terms, and they acquire their mass through their interaction with the Higgs field as shown in Fig. 2.4. The coefficient of the Majorana mass term M can be very large, and the coefficient of the Dirac mass term m can be of the order of the other lepton mass. The neutrino would not have states of definite mass, but would split into two neutrinos having a mass of m^2/M and two neutrinos of mass M. This is explained in more details in Ref. [20]. The very light neutrino would be mostly the left-handed neutrino and the very heavy would be the sterile right-handed neutrino. Similarly, the very light anti-neutrino would the right-handed one, the very heavy, the left-handed one. The feature of a very light mass and a very heavy mass balancing each other is what gave its name to the seesaw mechanism. (Reading "the oscillating neutrino" [21] was very helpful to write this section.)

2.2 Neutrino oscillation

The idea that neutrinos oscillate was first proposed separately by Pontecorvo and by Maki, Nakagawa and Sakata [2, 3]. In the 1960's and was later a good explanation for the disappearance of both solar and atmospheric neutrino observed by several experiments.

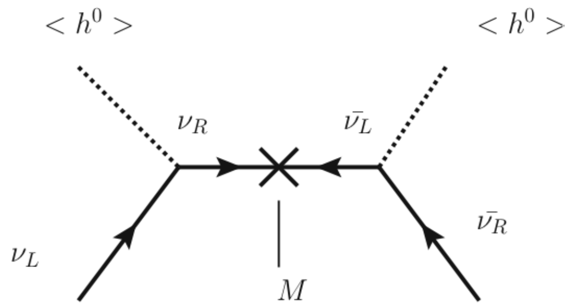

Figure 2.4: Schematic of the seesaw mechanism.

Neutrino oscillation relies on the fact that the mass eigenstates are not identical to the flavor eigenstates. This is similar to what happens in the quark sector because of the CKM matrix [22, 23], but in this case it involves the weak interaction instead of the strong interaction. Mass and flavor eigenstates are related as in the following equation by the PMNS matrix U, where $S_{ij}(C_{ij})$ stands for $\sin\theta_{ij}$ $(\cos\theta_{ij})$, and δ is the CP violating phase:

$$\begin{pmatrix} \nu_e \\ \nu_\mu \\ \nu_\tau \end{pmatrix} = \begin{bmatrix} U_{e1} & U_{e2} & U_{e3} \\ U_{\mu 1} & U_{\mu 2} & U_{\mu 3} \\ U_{\tau 1} & U_{\tau 2} & U_{\tau 3} \end{bmatrix} \begin{pmatrix} \nu_1 \\ \nu_2 \\ \nu_3 \end{pmatrix} \tag{2.3}$$

$$U = \begin{pmatrix} 1 & 0 & 0 \\ 0 & C_{23} & S_{23} \\ 0 & -S_{23} & C_{23} \end{pmatrix} \begin{pmatrix} C_{13} & 0 & S_{13}e^{-i\delta} \\ 0 & 1 & 0 \\ -S_{13}e^{i\delta} & 0 & C_{13} \end{pmatrix} \begin{pmatrix} C_{12} & S_{12} & 0 \\ -S_{12} & C_{12} & 0 \\ 0 & 0 & 1 \end{pmatrix} \tag{2.4}$$

As for all fermions and taking into account the PMNS matrix, the wave function of a neutrino in the flavor eigenstate α can be written as:

$$\Psi_\alpha(\overline{x}, t) = \sum_i U_{\alpha i} \exp^{-ip_i x} \nu_i = \sum_i U_{\alpha i} \exp^{-iE_i t + ip_\nu \overline{x}} \nu_i. \tag{2.5}$$

Since the masses of the neutrinos are very small, we know that $E_i \approx p_\nu + \frac{m_i^2}{2p_\nu}$ and therefore:

$$\Psi_\alpha(\overline{x},t) = \exp^{ip_\nu(x-t)}(\sum_i U_{\alpha i}\exp^{-\frac{im_i^2 t}{2p_\nu}})\nu_i. \tag{2.6}$$

Assuming that a neutrino of flavor α is traveling at the speed of light c for a distance L, we can write its probability to be in a flavor eigenstate β at time t as:

$$\begin{aligned} P(\nu_\alpha \to \nu_\beta) &= |\sum_i U_{\alpha i}U^*_{i\beta}\exp^{-\frac{im_i^2 t}{2p_\nu}}|^2 \\ &= \sum_i |U_{\alpha i}U^*_{i\beta}|^2 + Re\sum_i\sum_{i\neq j} U_{\alpha i}U^*_{i\beta}U_{\alpha j}U^*_{j\beta}\exp^{\frac{i|m_i^2-m_j^2|L}{2p_\nu}}. \end{aligned} \tag{2.7}$$

We can also reformulate this expression to write the oscillation probability of a neutrino of a given flavor eigenstate oscillating into another flavor eigenstate in a way where the oscillatory pattern is more explicit:

$$\begin{aligned} P(\nu_\alpha \to \nu_\beta) = \delta_{\alpha\beta} &- 4\sum_{i>j} Re(U^*_{\beta i}U_{\alpha i}U_{\beta j}U^*_{\alpha j}) \centerdot \sin^2\Phi_{ij} \\ &\pm 2\sum_{i>j} Im(U^*_{\beta i}U_{\alpha i}U_{\beta j}U^*_{\alpha j}) \centerdot \sin 2\Phi_{ij}, \end{aligned} \tag{2.8}$$

where $\Phi_{ij} = \frac{\Delta m_{ij}^2 L}{4E} = \frac{1.27\Delta m_{ij}^2(eV^2)L(km)}{E(GeV)}$ and $\Delta m_{ij}^2 = m_j^2 - m_i^2$. When studying atmospheric neutrinos, it is common to simplify Eq. (2.8) to its two-flavor equivalent (*i.e.*). This is allowed since the two mass splittings and therefore the two oscillation frequencies are very different. In the two-flavor approximation, the PMNS matrix simply becomes a 2×2 rotation matrix) for oscillation of ν_μ to ν_τ as follows:

$$
\begin{aligned}
P(\nu_\mu \to \nu_\tau) &= \sin^2 2\theta_{23} \sin^2 \left(\frac{\Delta m^2_{23} L_\nu}{4E_\nu} \right) \\
&= \sin^2 2\theta_{23} \sin^2 \left(\frac{1.27 \Delta m^2_{23}(eV^2) L_\nu(km)}{E_\nu(GeV)} \right),
\end{aligned} \tag{2.9}
$$

where the last step just takes into account the factors of $\hbar$ and c that have been neglected so far.

This derivation has been done several times in the past [24]. In this derivation, it is assumed that a beam of neutrinos of flavor α has a common momentum p_ν. This "common momentum" treatment where the neutrinos are in a linear superposition of mass eigenstates with equal momenta is incorrect. A derivation with a proper treatment of entanglement was done recently [25].

Two methods have been developed to measure θ_{23} and Δm^2_{23}. The first one uses the zenith angle distribution of several neutrino samples, and searches for different rates between the upward going neutrinos which have to travel a distance of about 10000 km and the downward going neutrinos which only travel about 20 km. This method has given excellent results to prove neutrino disappearance [1]. Another method is to select muon neutrino events that have a good resolution in energy E and flight length L, and to plot the L/E distribution for that sample of events. As you can see from Eq. 2.9, the position of the first oscillation minimum is a direct measurement of Δm^2_{23} and therefore this method will give better results for a measurement of Δm^2_{23}. In addition, the L/E analysis is an analysis that actually see an oscillatory pattern.

2.3 Importance of precise θ_{23} and Δm^2_{23} measurement

The current measurement of θ_{23} is compatible with θ_{23} being maximal. If θ_{23} were conclusively found to be maximal, this could be a hint of new symmetries in the leptons sector such as the $\mu - \tau$ interchange symmetry [26]. One prediction of the $\mu - \tau$ interchange symmetry is that $\theta_{13} \approx 0$ and that the deviation of θ_{23} from maximum and of θ_{13} from zero is related to the ratio of the solar mass mixing to the atmospheric mass mixing ($\epsilon \sim \sqrt{\Delta m_{12}^2/\Delta m_{23}^2}$).

Measuring Δm_{23}^2 to an extreme precision is not as compelling as the precision measurement of θ_{23}. Our current measurement is already good to about 10 percent, and improving this measurement is only interesting for comparison with measurements made by other experiments like MINOS [27]. However, as in the CKM case, over-constraining the parameter space can be an efficient way to find hints of new physics. Finally if the precision of the Δm_{23}^2 measurement was smaller than the value of Δm_{12}^2, the mass hierarchy of neutrino could be resolved.

2.4 Remaining open questions

After the measurement of θ_{23} through atmospheric neutrinos and θ_{12} through solar and reactor neutrinos, the remaining open questions are about θ_{13}, the CP phase δ, and the mass hierarchy of neutrinos. We already know that θ_{13} is small but it is not known yet whether it is zero or not. The current best limit on θ_{13} is $\theta_{13} < 0.04$ at 2σ and it is given by the Chooz experiment [28]. The oscillation of ν_μ to ν_e is a good probe of θ_{13}. The next generation of neutrino experiments will use this oscillation to try to measure θ_{13}.

The T2K experiment (Tokai to Kamioka) [29] is an electron neutrino appearance experiment; it uses a beam of muon neutrinos starting at J-PARC (Japan Proton Accelerator Research Complex) in Tokai, directed at Kamioka. The Double Chooz experiment [30] is an upgrade of the current Chooz experiment and makes use of reactor neutrinos.

If θ_{13} is found to be non-zero, then the search for the CP phase δ will start. One way to measure δ is through long-baseline neutrino appearance experiments. These kinds of experiments will be well-suited to solving the mass hierarchy. Several proposals for such experiments already exist in Japan with the T2KK proposal [31], in the US with the Fermilab to DUSEL proposal [32], and in Europe with the CERN-MEMPHYS proposal [33].

Chapter 3

Other neutrino oscillation experiments

In this Chapter I will very briefly review the other neutrino experiments that measure parameters from the PMNS matrix and that have presented results as of spring 2009. Different experiments are able to probe different sectors of the PMNS matrix. Atmospheric neutrinos probe mainly the 2-3 sector (which involves Δm^2_{23} and $\sin^2 2\theta_{23}$), solar neutrinos mainly the 1-2 sector. The flight length of reactor neutrinos can be adjusted to probe either the 1-2 or the 1-3 sector. And finally, the flight length and the energy of neutrino beam can be adjusted to probe the 2-3 or the 1-3 sector. There are experiments designed to make use of each of these configurations.

For results from LSND [34] and from MiniBooNE [35] please see their respective references.

3.1 Solar neutrinos θ_{12}: Homestake, Kamiokande, IMB, SNO, Borexino

The Homestake experiment [11] is radiochemical experiment using chlorine that was built in 1965-67 and operated until 1984. It was the first to attempt to measure the solar neutrino flux. Their result is famous as it is the first one to notice an discrepancy between the solar neutrino flux calculation and the solar neutrino flux measurement. This discrepancy is often referred to as the "solar neutrino problem. Their results was then confirmed by water Cherenkov detectors like Kamiokande [13] in Japan, IMB [14] in the United States and finally the Super-Kamiokande solar analysis [36].

The Sudbury Neutrino Observatory (SNO) experiment confirmed Super-Kamiokande results about solar neutrino [37]. The SNO results were a very nice confirmation of the neutrino oscillation theory. SNO was able to study both neutral current interactions and charged current interactions. In the case of charged current interactions, the outgoing lepton is studied, and it is therefore possible to tell the flavor of the neutrino at the time of the interaction. Disappearance of electron neutrinos was studied through charged current interactions. In the case of neutral current interactions on the other hand, the flavor of the neutrino cannot be determined as the recoiling nucleon is observed instead of the outgoing neutrino. Therefore, when studying neutral currents, one studies the total number of neutrinos regardless of the flavor. SNO found that the total number of neutrinos is consistent with the expected solar flux, and thus the disappearing electron neutrino must be oscillating into neutrinos of another flavor [37].

Finally Borexino [38] is one of the "next generation" solar neutrino experiment. It uses liquid scintillators to study neutrino oscillation through the measurement the Be-7 line neutrino flux ($E = 0.861\ MeV$).

3.2 KamLAND (Δm_{12}^2) and Chooz (θ_{13})

KamLAND, Chooz are two experiments which uses neutrinos from nearby nuclear reactors. The experiments are located at different distances from the nuclear plants, and therefore probe different oscillation parameters. KamLAND probes the $1-2$ sector while Chooz probes the $1-3$ sector. These two experiments use electron anti-neutrinos detected via inverse beta decay to do their measurement.

KamLAND is located in the Kamioka mine and uses neutrinos coming from 55 nuclear reactors distributed all around Japan. The latest KamLAND results are presented in Ref. [39] and the best fit values are $\Delta m_{12}^2 = 7.58^{+0.14}_{-0.13}(stat)^{+0.15}_{-0.15}(sys) \times 10^{-5}\ eV^2$ and $\tan^2(\theta_{12}) = 0.56^{+0.10}_{-0.07}\ (stat)^{+0.10}_{-0.06}\ (sys)$. Combining their results with the solar neutrino data from SNO and Super-Kamiokande the best fit results are $\Delta m_{12}^2 = 7.59^{+0.21}_{-0.21} \times 10^{-5}\ eV^2$ and $\tan^2(\theta_{12}) = 0.47^{+0.06}_{-0.05}$.

Chooz is located in the north of France, and uses neutrinos coming from a reactor located 1km away from the detector and is sensitive to the value of θ_{13}. So far Chooz results are consistent with $\theta_{13} = 0$ [28]. An upgrade of the experiment, double-Chooz [30] is planned. The upgrade involves a second detector located at 300 m from the nuclear cores, and an improved detector at the site of the Chooz experiment (at 1 km from the cores). The experiment is scheduled to start running with one detector in 2009 and with the second detector in 2010.

3.3 K2K and MINOS

All the past and current beam experiments are muon neutrino beam experiments looking at muon neutrino disappearance. K2K is located in Japan while MINOS is an American project. K2K finished running in 2004, while MINOS is currently taking data. There are two future experiments (T2K and NOνA) which will be looking for electron neutrino

Parameter	best fit	2σ	3σ
Δm^2_{12} $[10^{-5}\ eV^2]$	$7.65^{+0.23}_{-0.20}$	7.25-8.11	7.05-8.34
$\lvert\Delta m^2_{23}\rvert$ $[10^{-3}\ eV^2]$	$2.40^{+0.12}_{-0.11}$	2.18-2.64	2.07-2.75
$\sin^2\theta_{12}$	$0.304^{+0.022}_{-0.016}$	0.27-0.35	0.25-0.37
$\sin^2\theta_{23}$	$0.50^{+0.07}_{-0.06}$	0.39-0.63	0.36-0.67
$\sin^2\theta_{13}$	$0.01^{+0.016}_{-0.011}$	≤ 0.040	≤ 0.056

Table 3.1: Current status of oscillation parameter measurements (Ref.[4]).

appearance in a muon neutrino beam in order to measure θ_{13}.

K2K (KEK to Kamioka) was the first muon neutrino beam experiment and the first to provide a measurement of θ_{23} which did not involve atmospheric neutrinos [40]. It used a muon neutrino beam of about 1.3 GeV produced at KEK detected in the Super-Kamiokande detector located 250 km away from KEK. Their best fit point for $\sin^2 2\theta_{23}$ is 1 and their best fit point for Δm^2_{23} is $2.8 \times 10^{-3}\ eV^2$ [40].

MINOS uses the Fermilab NuMI beam and detects neutrinos using two detectors: a close detector located at 1.04 km from the NuMI target and a far detector located at 735 km. The ν_μ energy is around 5-10 GeV. The latest best fit results from MINOS are $|\Delta m^2_{23}| = 2.43 \pm 0.13 \times 10^{-3}\ eV^2$ at 68% confidence level and $\sin^2(2\theta_{23}) > 0.90$ at 90% confidence level. More details about the MINOS results can be found in [27].

3.4 Current neutrino oscillation results

The current status of the measurements of neutrino oscillation parameters is described by T.Schwetz *et al.* [4]. They perform global fits to all the data currently available to give the best measurements of the parameters in the 1-2 sector and the 2-3 sector. They also set a limit on θ_{13}. Their results are summarized in Table 3.1 and figures of the global fits are presented in Fig. 3.1-3.3.

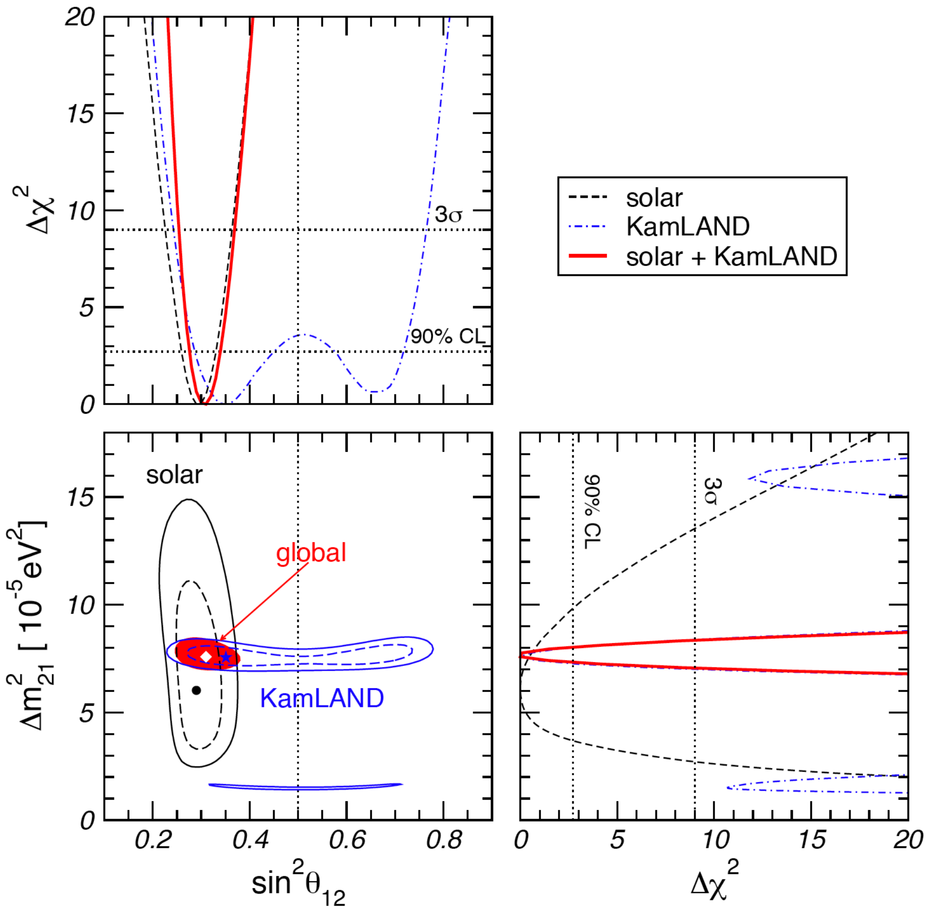

Figure 3.1: Determination of the leading "solar" oscillation from the interplay of data from artificial and natural neutrino sources. The χ^2-profiles and allowed regions at 90% and 99.73% confidence level are shown for solar and KamLAND, as well as the 99.73% C.L. region for the combined analysis. The dot, star and diamond indicate the best fit points of solar data, KamLAND and global data respectively. The fit was always minimized with respect to Δm^2_{31}, θ_{23} and θ_{13}, including always atmospheric, MINOS, K2K and Chooz data.(Ref.[4])

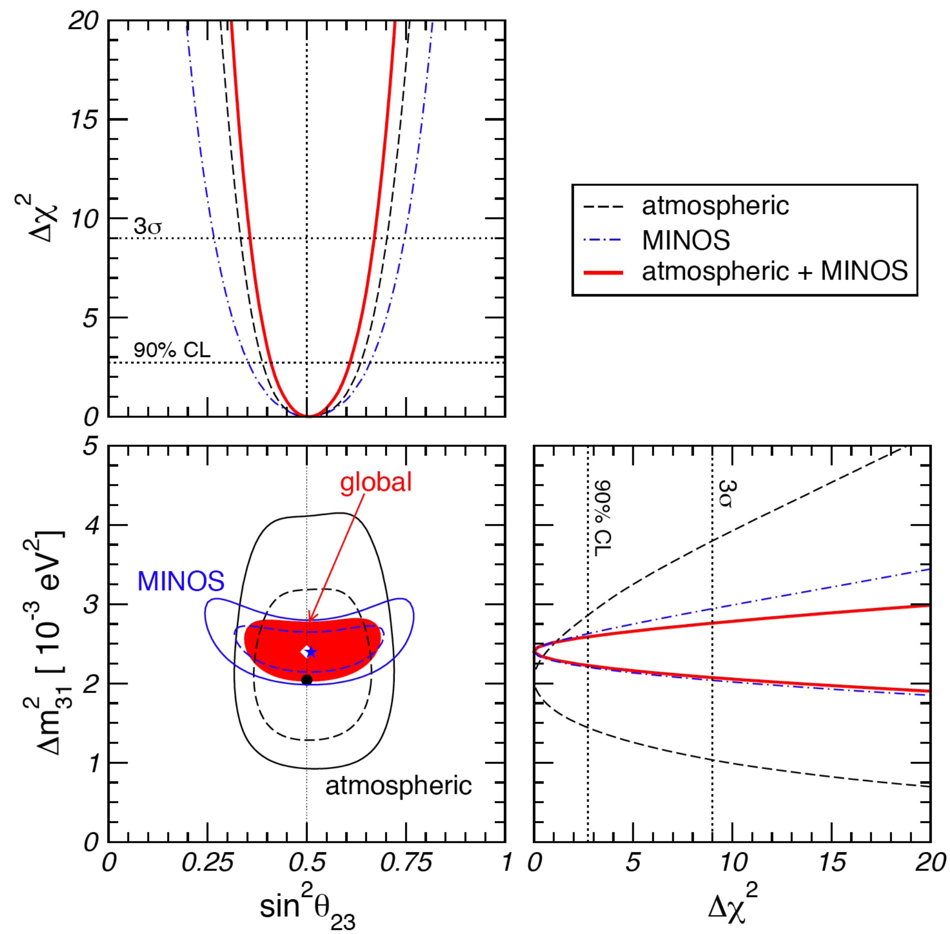

Figure 3.2: Determination of the leading "atmospheric" oscillation from the interplay of data from artificial and natural neutrino sources. The χ^2-profiles and allowed regions at 90% and 99.73% confidence level are shown for atmospheric and MINOS, as well as the 99.73% C.L. region for the combined analysis (including also K2K). The dot, star and diamond indicate the best fit points of atmospheric data, MINOS and global data respectively. The fit was always minimized with respect to Δm^2_{21}, θ_{13} and θ_{13}, including always solar, KamLAND and Chooz data.(Ref.[4])

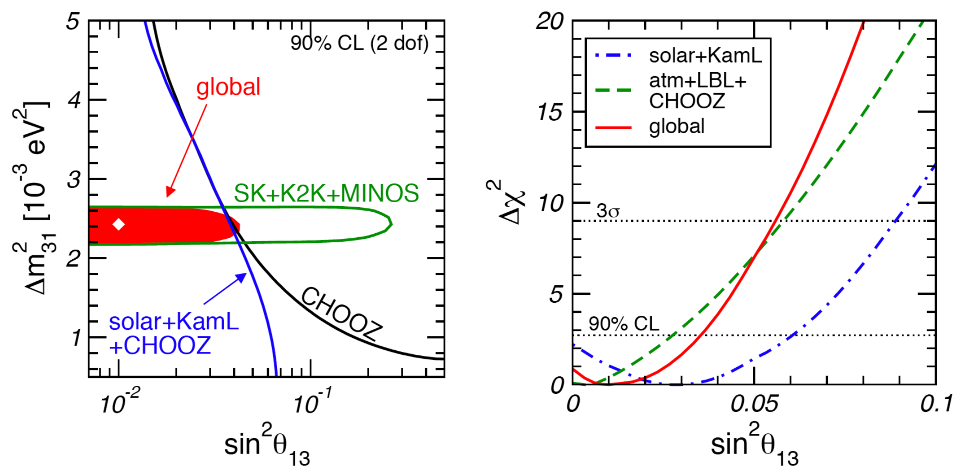

Figure 3.3: Constraints on $\sin^2\theta_{13}$ from global data.(Ref.[4])

Chapter 4

The Super-Kamiokande Detector

The Super-Kamiokande detector is a 50 kilo-tonne water Cherenkov detector located in a zinc mine, close to the town of Kamioka in the prefecture of Gifu, Japan. It is part of the Kamioka neutrino observatory which is operated by the Institute for Cosmic Ray Research (ICRR) of the University of Tokyo. It is about 1 km underground, which corresponds to about 2700 m of water overburden. The Super-Kamiokande detector uses Cherenkov light to detect solar and atmospheric neutrinos, and to search for nucleon decay. There are three distinct data-taking periods (SK1, SK2 and SK3), and the detector changed between each of them. First, I will describe the Cherenkov effect in Section 4.1 and then I will describe the detector and the changes made to the detector between each data-taking period in Section 4.2.

4.1 Cherenkov effect

When an electro-magnetically charged particle travels faster than the speed of light in a given medium, a cone of Cherenkov light is emitted. The aperture of the cone θ depends on the refractive index of the medium and the velocity of the particle: $\cos\theta \equiv \frac{1}{n\beta}$ where n is the refractive index of the medium and $\beta \equiv v/c$. In the case of water, where $n = 1.34$ in the visible range, the Cherenkov angle is 42° for a particle traveling at

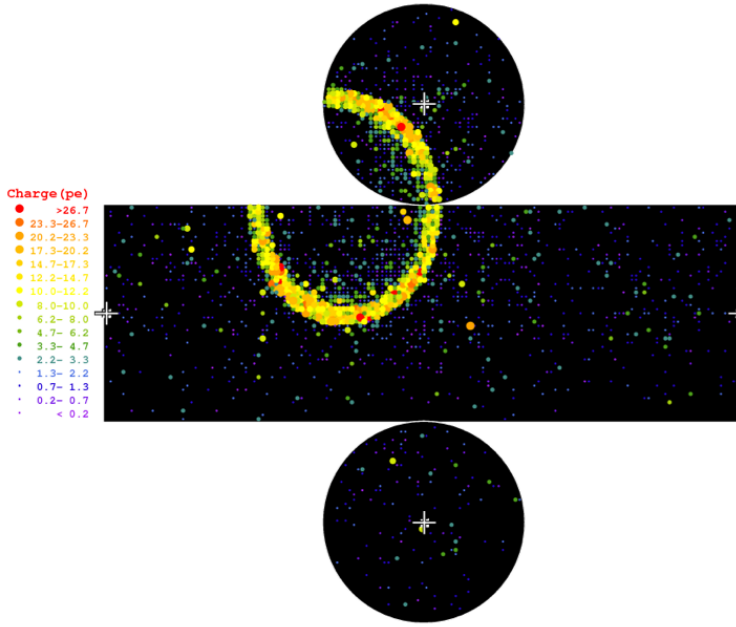

Figure 4.1: Example a Cherenkov ring created by a 1 GeV muon in the Super-Kamiokande detector (SK1)

nearly the speed of light.

The Cherenkov threshold is defined as the velocity at which a particle travels at the speed of light in the medium. This is the velocity at which the opening angle of the Cherenkov ring is zero and above which the particle will start to emit light. The velocity threshold is simply given by $\beta_t \equiv 1/n$ and thus $\gamma_t \equiv \frac{1}{\sqrt{1-\beta_t^2}}$. We can now easily calculate the momentum threshold of different particles as $\bar{p}_{threshold} \equiv \gamma_t mc$ and the energy threshold is given by $E_{threshold} \equiv \gamma_t mc^2$. In water where $\gamma_t = 1.5$, the momentum threshold for an electron and a muon are 0.57 MeV/c and 120 MeV/c, respectively.

In the Super-Kamiokande detector, if an event is fully contained inside the inner detector, a Cherenkov cone appears as a ring on the wall of the detector as it can be seen in Fig. 4.1. The axis of the cone corresponds to the direction of the particle, and by measuring the number of photoelectrons detected in the photomultiplier tubes (PMTs), we are able to reconstruct the energy of the particle.

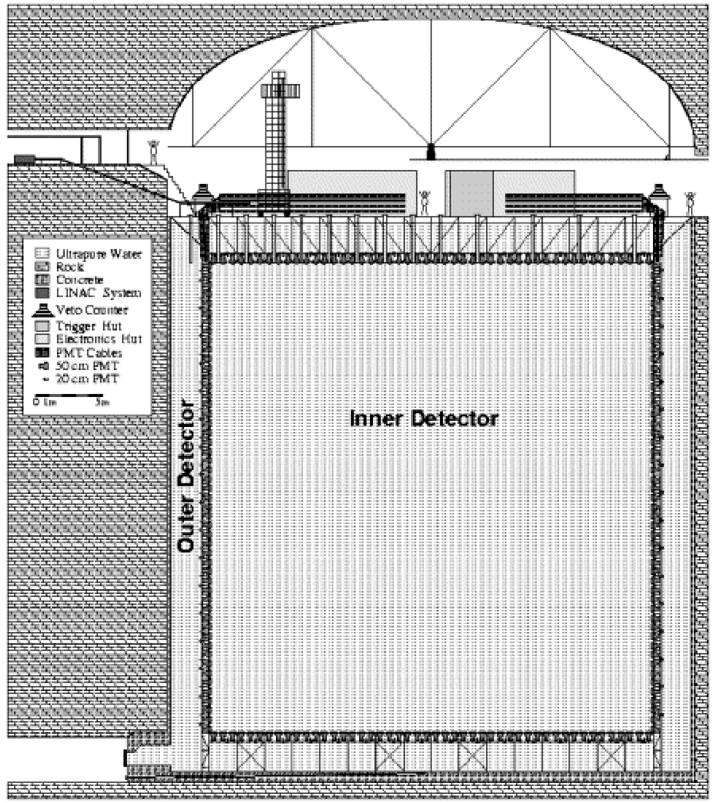

Figure 4.2: Schematic view of the Super-Kamiokande detector [5].

4.2 Overview of the detector

The water tank is 42 meters high, 39 meters in diameter and made of stainless steel. The detector is separated into an inner detector (ID) and an outer detector (OD). The inner detector is where most of the interesting physics happens, where we can reconstruct energy and direction with good accuracy. The outer detector is a shell of about 2.5 meters and is mainly a veto region for cosmic ray muons, but it can also be used to reconstruct the direction of particles that have enough energy to exit the inner detector. A general view of the detector is shown in Fig. 4.2.

The inner detector is covered with 11146 (5182) 20 inches photomultiplier tubes (Hamamatsu R3600) for SK1 (SK2) while the OD uses 1885 8 inches photomultiplier tubes (Hamamatsu R1408 for SK1 and R5912 for tubes added for SK2 and SK3).

Wavelength shifter plates are attached to the OD PMTs as it was done in the IMB

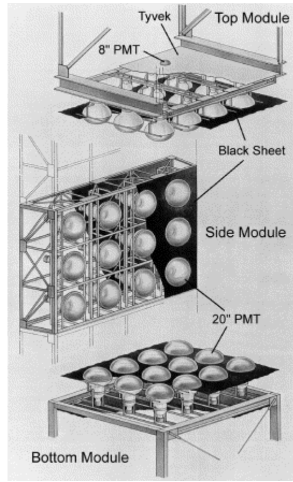

Figure 4.3: Details of the stainless steel structure, and mounting of the PMT [5].

experiment [41]. This increases their collection efficiency by about a factor of 1.5 but the wavelength shifter plates also broaden the timing resolution of the OD PMT by about 2 ns. This is a reasonable price to pay for the gain in collection efficiency since the main purpose of the OD is to act as a veto counter.

All the PMTs are mounted on the same stainless steel structure. The inner PMTs are facing inwards and the outer PMTs outwards. The inner and outer detectors are separated by two layers of polyethylene terephthalate sheets, referred to as “black sheets” mounted on each side of the structure that holds the PMTs. The walls of the outer detector are covered with white Tyvek sheets in order to reflect photons towards the OD PMTs. Tyvek is a paper-like material that is very solid and reflects light in the UV with a good efficiency. Details of the stainless steel structure, and the mounting of the PMT is shown in Fig. 4.3.

The cables that connect the PMTs to the electronic huts located on the top of the detector pass through 12 cable holes. Four of these twelve holes are above the ID and would prevent Cherenkov light from being seen in the OD. In order to detect cosmic ray muons that enter the detector through one of these cable hole, veto counters were added in April 1997 and are presented in Fig. 4.4.

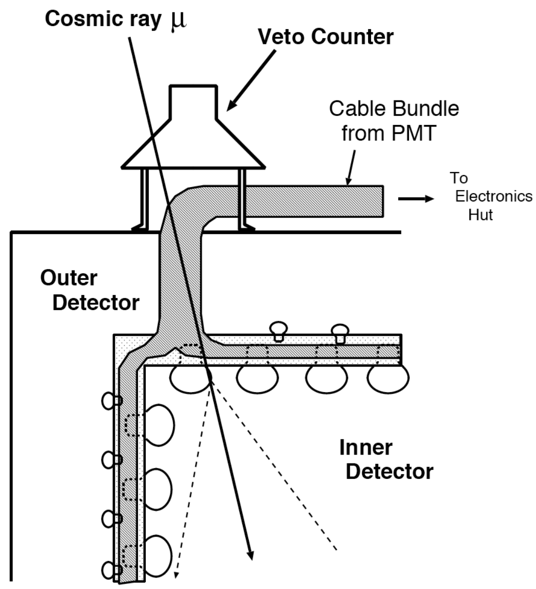

Figure 4.4: Veto counters placed above the cable bundles to reject cosmic ray muons.

4.2.1 History of the Super-Kamiokande detector and differences in the detector between each data-taking period

There are differences in the SK detector between the three data-taking periods completed as of September 2008. SK1 is the original design with a 40% photo-coverage of the ID and it is extensively described in the SK NIM paper published in 2003 [5]. After five years of data-taking with the SK1 detector, it was decided to replace the failed OD PMTs with newer tubes. To do so, the detector had to be switched off and emptied. This happend in 2001 andthis is the end of the SK1 data-taking period. In November 2001, during the refilling operation that followed the upgrade, there was an accident where half of the PMTs were destroyed by a chain reaction initiated by the implosion of one of the bottom ID PMTs. In order to restart operation quickly after the accident, the remaining PMTs were redistributed in the whole ID, and therefore the SK2 data-taking period has a 20% photo-coverage. The OD could be restored to its full coverage immediatly since less PMTs were necessary. At that time, it was also decided to add

Figure 4.5: 20 inch PMT in its acrylic shell. Shell was added after SK1.

an acrylic shell around each ID PMT in order to avoid another accident of the same kind. The acrylic shells are a source of radioactive background for analyses that use solar neutrinos. A 20 inch ID PMT with the acrylic shell is shown in Fig. 4.5.

While during the SK1 period all the OD PMTs came from the IMB experiment [42], after the accident only 650 OD PMTs were IMB PMTs, the rest of the OD coverage was done using a new model of Hamamatsu 8 inches PMT. Since new OD PMTs have a better timing resolution than the IMB PMTs, there are differences in the SK software that concerns the OD. (See Chapter 6 about Reduction and Chapter 7 about Reconstruction.) After two and a half years of data-taking with half the ID photo-coverage, enough new ID PMTs had been produced to recover the full photo-coverage of the inner detector, and therefore in October 2005, SK2 ended and in July 2006, SK3 started. For SK3 it was also decided to segment the outer detector in order to better reject cosmic ray muons which clip the corner of the detector ("corner clipper muon" events). More details about the OD segmentation for SK3 can be found in Appendix A. Because of the acrylic shells the number of ID PMTs in the SK3 period is not exactly the same as in the SK1 period. In Fig. 4.6, I present the map of old versus new OD tubes for the SK2 data-taking period and in Table 4.1 I summarize the differences between each data-taking period.

Characteristics Livetime	SK1 (1996-2001) 1489 days	SK2 (2002-2005) 803 days	SK3 (2006-2008) 550 days
Photo-coverage	40%	20%	40%
Acrylic shells	no	yes	yes
Number of ID PMTs	11146	5182	11129
Number of OD PMTs	1885	1885	1885
# of R1408 OD PMTs	1885	650	611
# of R5912 OD PMTs	0	1235	1274
OD segmentation	no	no	yes

Table 4.1: Summary of differences between the SK1, SK2 and SK3 data-taking periods

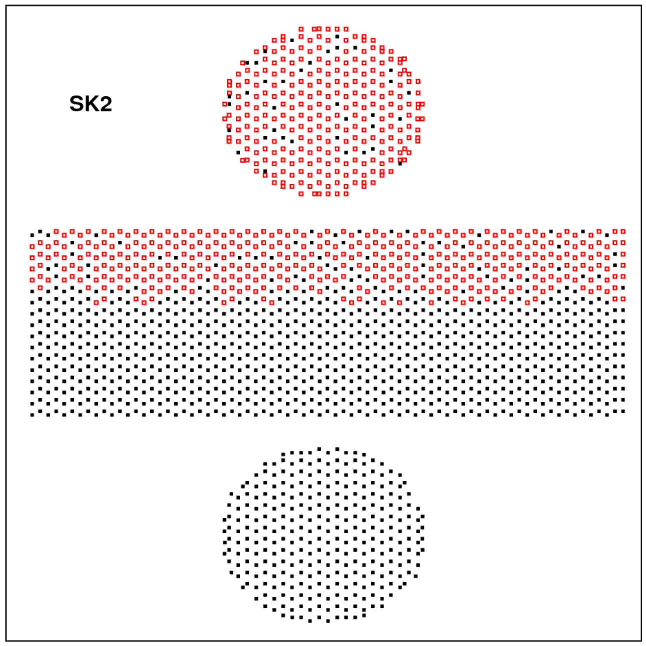

Figure 4.6: Old (red empty squares) and new (full black square) PMTs for the SK2 period. The SK1 period uses only old tubes, and the SK3 period is very similar to SK2.

4.2.2 Description of the PMTs

A photomultiplier tube works by accelerating single photoelectrons created on the cathodic surface of the tube towards the center of the tube. Then, this signal is amplified through an array of dynodes such that a big enough electrical signal can be read out of the PMT. A photomultiplier tube is characterized by its single photoelectron efficiency, (ie, how good it is at detecting single photon), its peak quantum efficiency, its collection

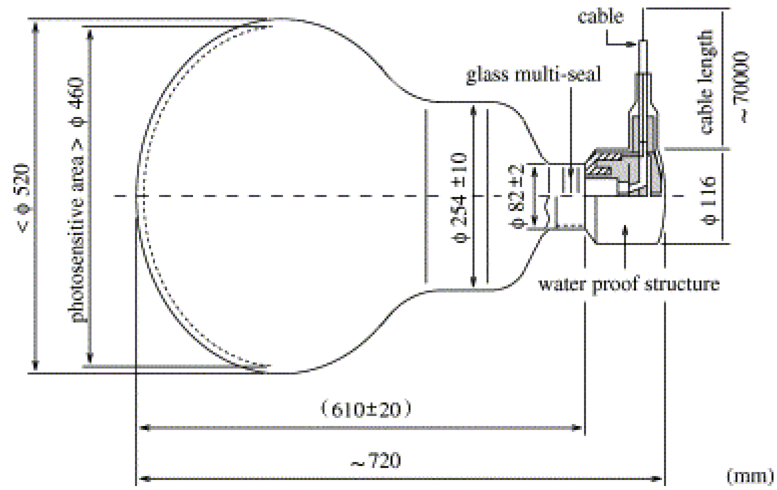

Figure 4.7: Schematic of a 20 inch ID PMT [5].

efficiency and its gain, (ie, for a given photoelectron, how much is the signal amplified). The characteristics of both kinds of PMTs used in the Super-Kamiokande detector can be found in the next two subsections. More details about the PMTs can be found in the SK NIM paper [5].

Inner PMTs

The PMTs used in the inner detector are 20 inches in diameter (Hamamatsu R3600). The dynamic range of the ID PMTs goes from a single photoelectron (pe) to about 300 pe. The peak quantum efficiency is about 21% at 360-400nm and the collection efficiency is 70% at the first dynode. The gain is of the order of 10^7 when the PMTs are operated with a high voltage supply ranging from 1700 V to 2000 V. Finally, the timing resolution of an ID PMT is 2.2 ns. A schematic view of the 20 inch ID PMT is presented in Fig. 4.7.

Outer PMTs

We have two kinds of OD PMTs. When the Super-Kamiokande detector was first built, the old IMB [42] tubes were used in the outer detector, but after the accident, most

Hamamatsu 8-inch PMT	R1408 (IMB)	R5912 (new)
Peak wavelength	420 nm	420 nm
Spectral response	300 nm - 650 nm	300 nm - 650 nm
Peak quantum efficiency at 390 nm	25%	25%
Power needed	1500V	1500 V
Transit time spread (FWHM)	7.5 ns	2.4 ns
Gain	10^8	10^7
Number of stages	13	10
Dynode structure	venetian blind	box and line

Table 4.2: Specifications of Hamamatsu R1408 8-inch PMT and R5912 8-inch PMT.

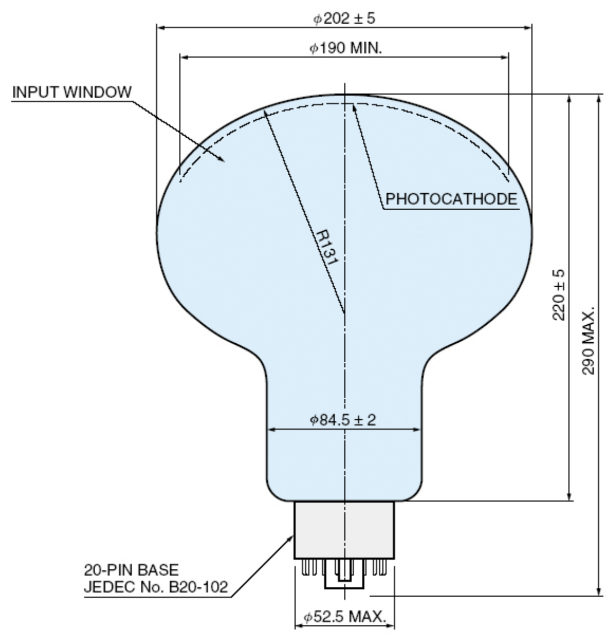

Figure 4.8: Schematic of a 8 inch R5912 OD PMT. (Picture taken from the Hamamatsu website [43])

of the tubes had to be replaced. The IMB tubes are Hamamatsu R1408, and the new tubes are Hamamatsu R5912. Specifications for both kinds of tubes are presented in Table 4.2, and a schematic view of the R5912 PMT is shown in Fig. 4.8.

It was often quoted [5, 42] that the timing resolution (transit time spread) of the R1408 PMT is 13 ns without the wavelength shifter plates. This is the timing resolution for a single pe illumination. The value given in Table 4.2 is the value given on the specification sheet of Hamamatsu. The quantum efficiency for both kind of tubes is

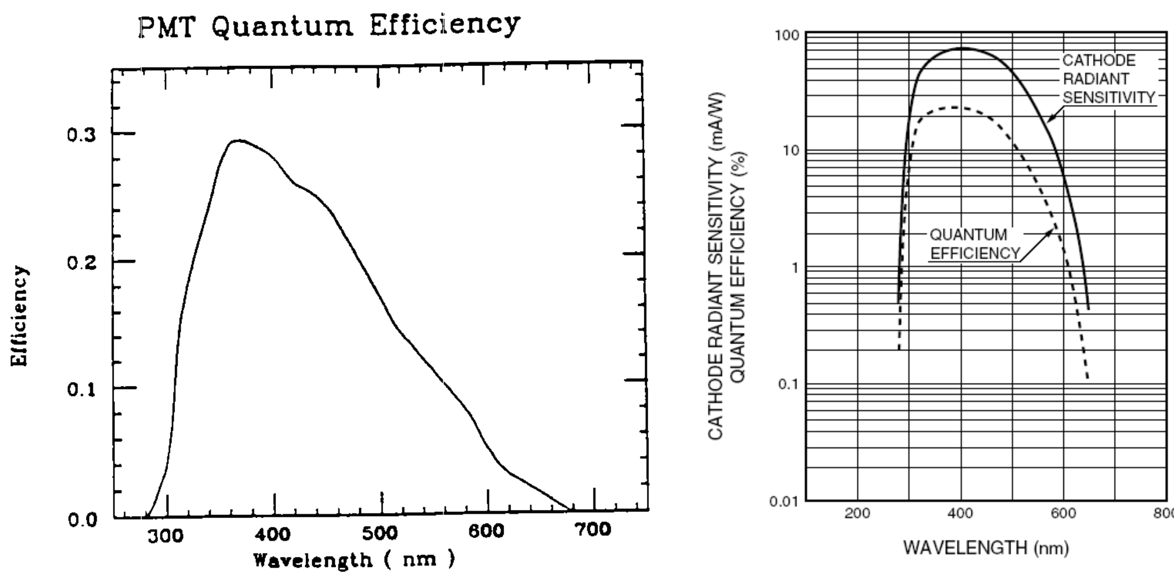

Figure 4.9: Quantum efficiency for R1408 8-inch tubes (left) (figure taken from [42]) and R5912 8-inch tubes (right) from Hamamatsu specifications sheet [43]).

shown in Fig. 4.9. (Better plot available on spec sheet of R1408, but need to be scanned)

4.3 Overview of electronics and DAQ

In this Section, I will describe the electronics and the data acquisition (DAQ) system. This section is highly inspired from the Super-Kamiokande NIM paper [5]. All the DAQ electronics for the Super-Kamiokande detector are located on top of the detector in four "electronic huts." Each huts corresponds to one quadrant of the detector. Each PMT is connected to its hut by a coaxial cable. The cables run on the outer side of the stainless steel structure. The data acquisition system for the ID PMTs and for the OD PMTs are separated.

4.3.1 ID electronics and DAQ

A schematic view of the ID data acquisition system can be found in Fig. 4.11. The PMT cables are connected to a TKO (Tristan KEK online) module called ATM (Analog Tim-

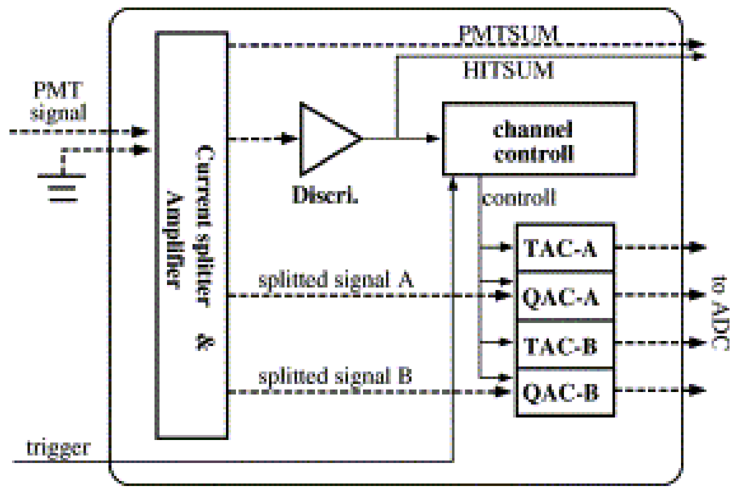

Figure 4.10: A schematic view of the analog input block of the ATM. Only one channel is shown in the figure. Dashed arrows show the PMT signal, its split signals, and accumulated TAC/QAC signals. Solid arrows show the logic signals which control the processing of the analog signals [5].

ing Module) and shown in Fig. 4.10. The purpose of the ATM is to convert the analog signal of each PMT into a digitized signal containing the charge and time information.

There is one ATM for every 12 PMTs. The signal for each PMT is split into four so that it can be used by several sub-systems. Part of the signal is used to build a variable called HITSUM which will be used for the trigger. The trigger is described in more details later in this chapter. If the charge deposited in one PMT is greater than 1/4 pe then the PMT was "hit". If a PMT was hit then the ATM generates a 15 mV pulse with a 200 ns width, these pulses are gathered at the front of the ATM and added to the global HITSUM. Another part of the signal is integrated in charge by a Charge-to-Analog converter (QAC) and in time by a Time-to-Analog converter (TAC) so that if a trigger is received the signal can be digitized and stored. There are two QAC and TAC for each channel so that if two events occur very close to each other, they can both be stored. The last fourth of the signal is used to build up the PMTSUM (total number of PMT that were hit).

The high voltage supply for the ID is provided by 48 CAEN SY527 main frames. Each of the frames supports 10 high voltage cards which can distribute power to 24

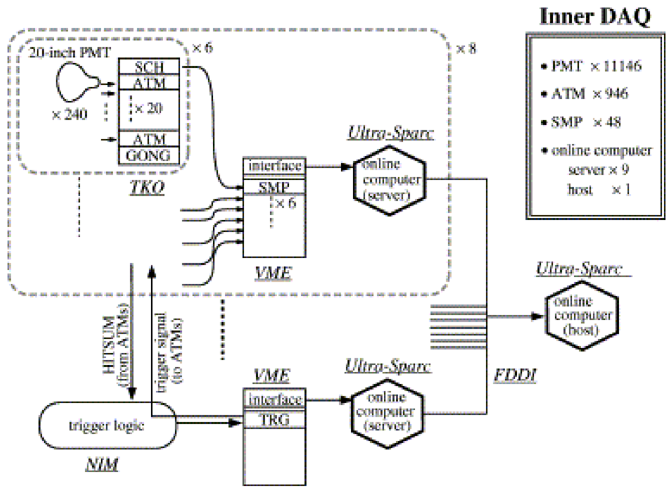

Figure 4.11: The ID data acquisition system [5].

channels. The high voltage supplies are monitored and can be operated remotely by a slow control monitor.

There are 946 ATM modules distributed in the four quadrant huts. If a trigger occurs, the trigger module generates an event number and pass this information to the ATM module.

4.3.2 OD electronics and DAQ

The OD data acquisition system is similar to the ID system. The signal from each PMT is digitized, then combined into a HITSUM and if the HITSUM is larger than a given threshold or if there was on ID trigger, the information is read out. Each OD PMT is supplied with high voltage through a coaxial cable and the same cable carries the analog signal back to the corresponding quadrant hut. There is one high voltage mainframe in each quadrant hut and each mainframe controls 48 channels. Each channel is connected to a "paddle card" which distributes the power to 12 PMTs. The paddle cards were built at BU (check). At the end of the SK1 period, the paddle cards were upgraded such that it was easier to disable dead or noisy channels. Zener diode jumpers were also added so that the high voltage could be fine tuned for a single PMT. Instead of ATMs, the OD uses charge-to-time conversion modules called QTC in order to measure the hit and charge of each PMT and to convert this information into a format which can be read and stored by the Time-to-Digital converters (TDC). A more complete description of the OD DAQ can be found in the SK NIM paper [5].

4.3.3 Trigger

There are two kinds of trigger, a hardware trigger, and a software trigger. The software trigger called the Intelligent trigger is designed to select low energy events from solar neutrinos. It is not used in the atmospheric neutrino analysis and therefore I will not describe it here in detail. More information about the Intelligent trigger can be found in the SK NIM paper [5].

There are two possible hardware triggers. One uses the ID information with three different energy thresholds, while the other one uses the OD information. The ID triggers use the HITSUM signal generated by the ATM module. The HITSUM signal is equivalent to counting the number of hits in the detector. For example when the HITSUM signal crosses -320 mV this is equivalent to having 29 hits in ID PMTs. We can also convert the number of hit PMTs into the amount of Cherenkov photons produced by an electron, assuming a 50% collection efficiency. For example, 29 hits in the ID PMTs correspond to a 5.7 MeV electron.

All triggers look for coincidence of hit PMTs in a 200 ns time window. The Super Low Energy (SLE) trigger requires a hit threshold corresponding to a 4.6 MeV electron, the Low Energy (LE) trigger requires 29 hits in the 200 ns time window, which is equivalent to a 5.7 MeV electron being detected. The High Energy (HE) trigger requires that the HITSUM threshold crosses -340 mV which is equivalent to 31 hit ID PMTs. Finally, the OD trigger requires 19 hits in the OD in the 200 ns time window. Each trigger, including the OD trigger, will trigger the readout of the entire detector. For SK2, the trigger threshold for LE was set to 8 MeV equivalent and the HE trigger to 10 MeV.

The SLE threshold was suppressed. For SK3, the threshold of the triggers were set back to their original SK1 values.

4.4 Radon hut and water purification

For the study of solar neutrinos, it is crucial to have energy thresholds as low as possible. The main challenges for attaining these low energy thresholds come from radioactive sources that emit photons in the detector and poor water transparency that prevents low energy Cherenkov photons from reaching the wall PMTs.

One of the major sources of radioactivity in the Super-Kamiokande detector is the radon that is present in the air of the mine. In order to remove this radon, fresh air is brought from the outside of the mine, through a pipe that runs along the Atotsu tunnel. The radon system is located in the radon "hut", outside the Atotsu entrance. To improve the water transparency, the water is purified by a multi-step purification system.

More information about the radon hut and the water purification system can be found in the Super-Kamiokande NIM paper [5].

4.5 Calibration

There are several parameters that need to be measured or calibrated in the Super-Kamiokande experiment: the water transparency, the light scattering, the relative gain and timing of the PMTs, and the absolute energy scale. There are several methods for calibrating these parameters. I will give a brief overview of these methods, but more details can be found in the Super-Kamiokande NIM paper [5].

The water transparency is characterized by the attenuation length of light in water. Two methods are used to measure this attenuation length. A direct measurement is

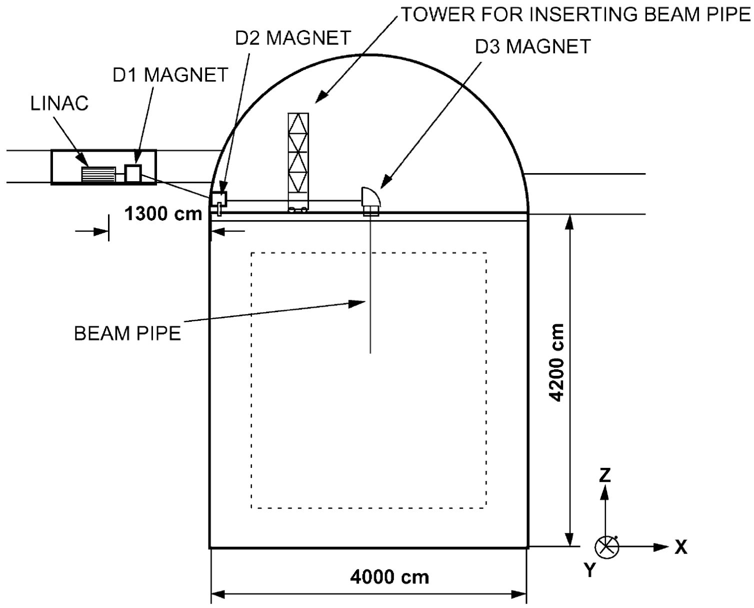

Figure 4.12: Linac system [5].

done using a laser ball, and an indirect measurement using cosmic rays.

The light scattering and absorption parameters are measured using a combination of dye and N_2 lasers that are fired in the detector though optical fibers during normal data taking.

The high voltage values recommended for PMTs were adjusted at the factory such that each PMT has equal gain. Before starting the SK1 data-taking period, those values were recalculated using a Xenon lamp setup. Since it is not possible to retake this measurement during data taking, the measurement was redone before the SK2 and SK3 data-taking period, and the high voltage of each PMT was adjusted accordingly.

Measuring the relative timing of PMTs is crucial for good timing resolution and thus for good event time reconstruction. A N_2 laser is used for the timing calibration.

There are several ways of measuring the absolute energy scale. The electron LINAC system (see Fig. 4.12) is good for a low energy direct measurement. This measurement is cross-checked with the study of the decay of ^{16}N. Low energy calibration is important for solar neutrinos which have energies in the 5-20 MeV range. Electrons produced in the decay of cosmic ray stopping muons are a good tool to measure the absolute energy scale in the 20-60 MeV range. Comparing decay electrons of data and Monte Carlo simulation (MC) allows an energy resolution of a few tens of MeV. Stopping muons are a good tool for a wide range of energies. From 60 to 400 MeV the momentum of the muon is low enough such that the Cherenkov angle has not yet reached its limit of 42°. Therefore, we can use the fact that the Cherenkov angle is given by $\cos\theta \equiv \sqrt{p^2+m^2}/np$ where p is the momentum, m the mass, and n the refractive index of water to measure precisely the momentum of the muon. Comparing data and MC for stopping muons in that energy range gives an energy resolution of about 1.5%. At higher energy, we can use the fact that the track length of the muon is proportional to its momentum. Finally, events that are identified as π^0 are used to probe the 150-600 MeV range, by reconstructing the π^0 mass peak.

In summary, the energy calibration is done through LINAC data at low energy and the resulting resolution is better than 1%, while the energy calibration at higher energy is done through data/Monte Carlo agreement and the resulting resolution is of the order of 2.6%. A summary of the energy resolution for the energy range where we use data/MC comparison to do the calibration is presented in Fig. 4.13.

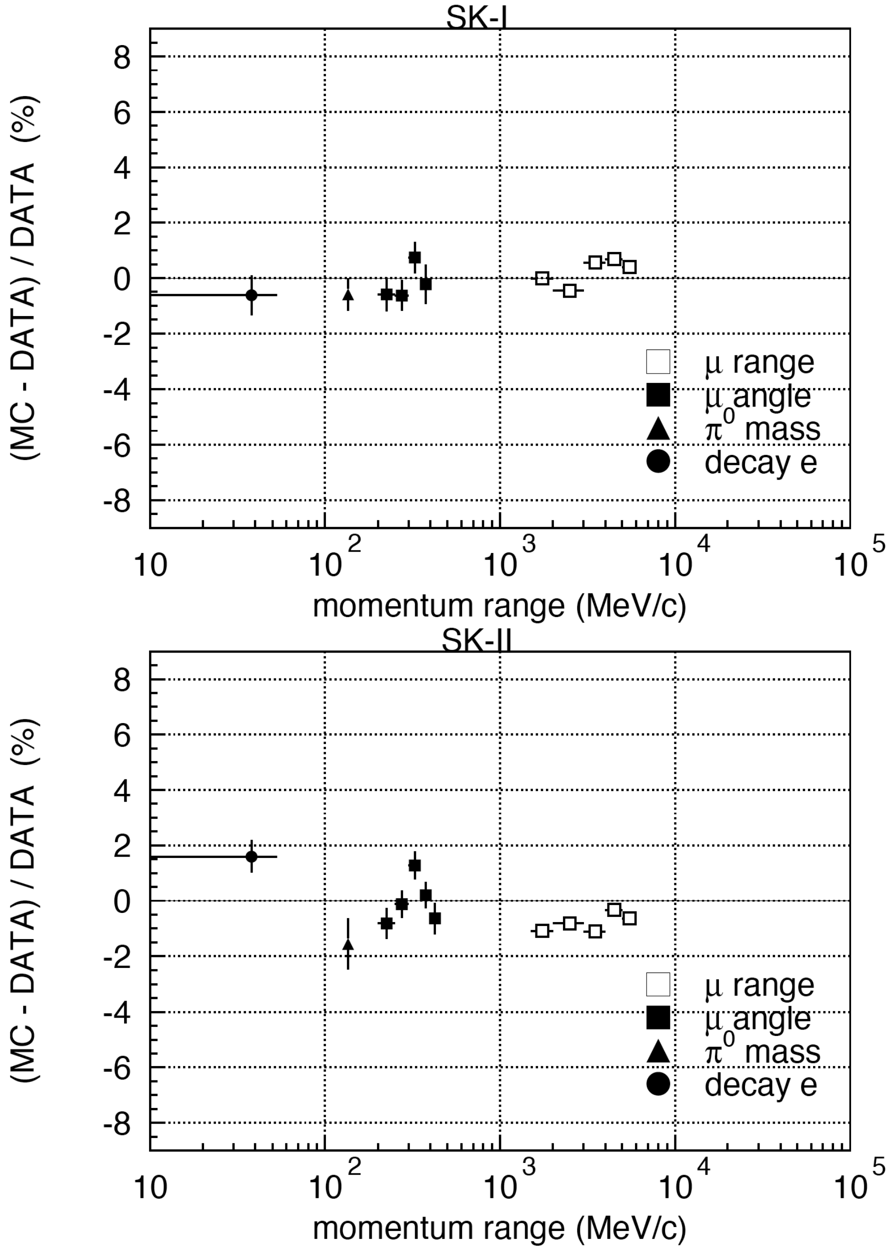

Figure 4.13: Summary of the absolute energy scale calibration for SK1 (top) and SK2 (bottom). The horizontal axis shows the momentum range of each source and the vertical axis shows the deviation of the data from the Monte Carlo predictions. [6].

Chapter 5

Simulation

In order to tell whether the atmospheric neutrino data collected by the detector agrees with a given model, and in order to measure the parameters of this model, we need to compare the data against a set of Monte Carlo (MC) data. To create this set of MC data, we first simulate the generation of atmospheric neutrinos by using the current knowledge about the cosmic ray flux. Then we simulate the different interaction modes that neutrinos can have with water at energies ranging from a few tens of MeV to several GeV. After the simulation of the neutrinos themselves is completed, we still need to simulate the detector response. Finally, the Monte Carlo sample is treated exactly like the data, we apply reduction tools (Chapter 6) and reconstruction tools (Chapter 7) to create the final Monte Carlo set.

5.1 Atmospheric neutrino flux

Atmospheric neutrinos are created when cosmic rays (mainly consisting of protons) hit the atmosphere and create charged pions and kaons. Pions mainly decay to a muon neutrino and a muon, while kaons have two main decay modes.

$$\begin{aligned}
\pi^+ &\rightarrow \nu_\mu \mu^+ \quad (100\%) \\
K^+ &\rightarrow \nu_\mu \mu^+ \quad (63\%) \\
&\rightarrow \pi^+ \pi^0 \quad (21\%) \\
&\rightarrow \pi^+ \pi^+ \pi^- \quad (6\%)
\end{aligned} \tag{5.1}$$

The muons then decay to neutrinos:

$$\mu^+ \rightarrow e^+ \overline{\nu}_\mu \nu_e. \tag{5.2}$$

The energy spectrum of atmospheric neutrinos is very wide and ranges from a few MeV to several GeV. This is due to the large range of cosmic ray proton energies. Depending on the energy of the cosmic ray proton, different ratios of pions to kaons are produced and therefore different ratio of muon neutrino to electron neutrino. At low energies where cosmic ray protons mainly produce pions, the ratio of ν_μ to ν_e is about two. It increases at higher energies, when kaons start to be produced.

The simulation of atmospheric neutrinos for the Super-Kamiokande experiment uses the neutrino flux calculation done by Honda *et al.* [44]. There are other atmospheric neutrino flux calculations done by G. Battistoni *et al.* [45] (Fluka flux) and G. Barr *et al.* [46] (Bartol flux). The difference between these models is used to estimate the systematic uncertainties on the neutrino flux. The calculated energy spectrum of atmospheric neutrinos at the Super-Kamiokande site for the Honda flux, Fluka flux and Bartol flux is shown in the left panel of Fig. 5.1. The right panel shows the flavor ratio of $\bar{\nu_e} + \nu_e$ to $\bar{\nu_\mu} + \nu_\mu$.

The primary cosmic ray flux depends on the solar activity. If the solar activity is

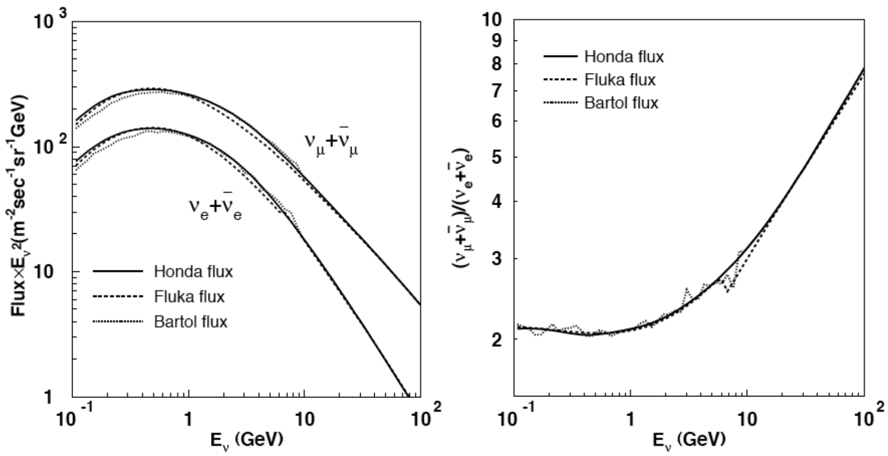

Figure 5.1: Predictions of the direction averaged atmospheric neutrino flux (left) and the flavor ratio (right) [6].

high (solar maximum), the solar winds are strong and the flux of cosmic rays that reach the atmosphere is decreased. Similarly if the solar activity is low (solar minimum), the cosmic ray flux is increased. For 1 GeV cosmic rays, the flux at solar minimum differs by a factor of two from the flux at solar maximum. For 10 GeV cosmic rays the difference is about 10% while 100 GeV cosmic rays are not affected. Another effect taken into consideration is the geomagnetic field, which acts as a shield for low momentum cosmic rays.

After the primary cosmic rays hit the atmosphere, secondary particles (mainly pions, kaons and muons) are created as described in Eq. 5.1. The decay of secondary mesons creates mainly muons and neutrinos. In the calculation of the neutrino flux, the interactions and the propagation of particles is done in a 3-dimensional manner. This is especially important for the L/E analysis because the two main effects of applying a 3-D treatment versus a 1-D treatment are:

1. An enhancement of the neutrino flux for near-horizontal directions.

2. Lower production heights of neutrinos in the atmosphere. This also affects mainly near-horizontal neutrinos.

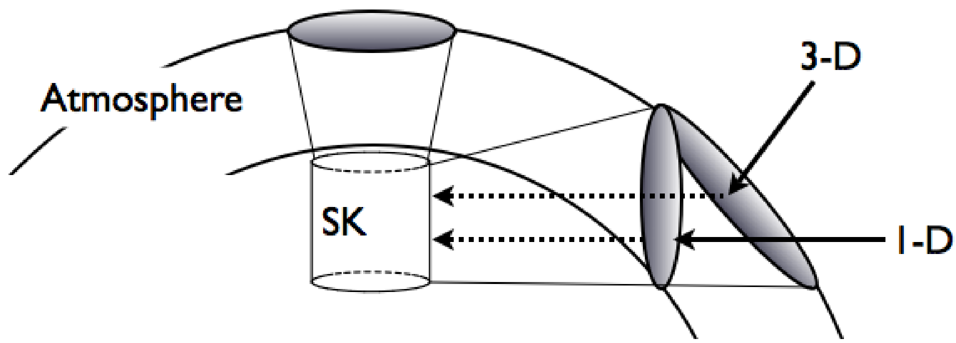

Figure 5.2: Example of 1D versus 3D flux calculation. The solid arrows denote the primary cosmic ray, while the dotted arrows denote the neutrinos.

The first effect is due to a difference in effective area for primary cosmic rays that generate horizontally incoming neutrinos as it can been seen in Fig. 5.2. This effect is especially important for low energy neutrinos ($1 <$ GeV). In that case, the incoming cosmic ray and the outgoing neutrinos are less likely to be colinear, either because of the kinematics of hadronic interactions, or because the outgoing muon can more easily be bent by the geomagnetic field if it has low momentum.

The second effect is explained by the fact that horizontal cosmic rays have to travel a larger distance to reach the same altitude as vertical cosmic rays. Therefore horizontal cosmic rays produce neutrinos higher in the atmosphere than vertical cosmic rays. In the 1D treatment only horizontal cosmic rays can produce horizontal neutrinos in the detector, but in the 3D treatment this is not the case. As a result, the production height of horizontal neutrinos is lowered. The 50% accumulation probability is the height above which 50% of the neutrinos of a given energy have been produced. We can see in Fig. 5.3 that applying a 3-D treatment does decrease the production height of horizontally incoming neutrinos, especially at at energies below 1 GeV.

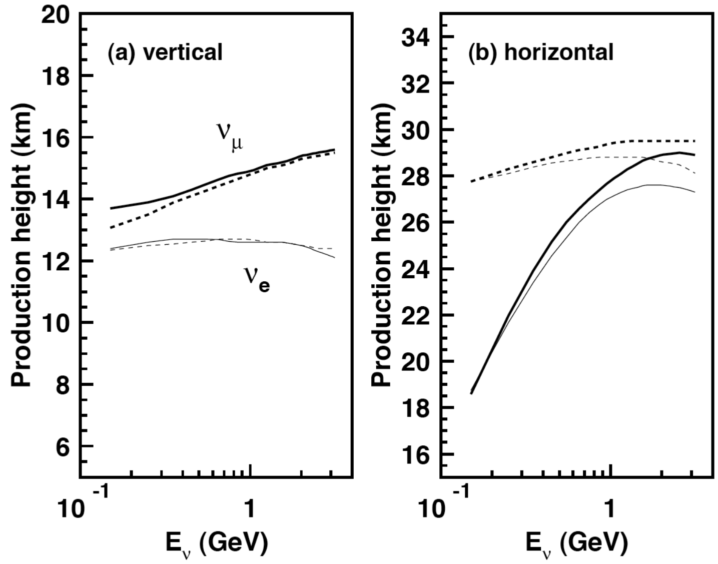

Figure 5.3: 50% accumulation probability lines of neutrino production height for (a) near-vertical ($\cos\theta > 0.95$) and (b) near-horizontal ($|\cos\theta| < 0.05$) directions. Thick and thin solid lines are for ν_μ and ν_e calculated with the 3D treatment, while thick and thin dashed lines are for ν_μ and ν_e calculated with the 1D treatment [47].

5.2 Neutrino interaction

The simulation model is based on the NEUT library [48–50]. The NEUT library was first developed to simulate the background caused by neutrino interactions in the Kamiokande nucleon decay measurement, and it was later expanded for the study of all atmospheric neutrinos. It is designed to simulate neutrino interactions with water (proton and oxygen) for energies ranging from a few MeV to 1 TeV. In the NEUT code, the following interactions are considered:

$$\begin{aligned}
\text{CC/NC (quasi)-elastic scattering :} &\quad \nu + N \rightarrow l + N' \\
\text{CC/NC single meson production :} &\quad \nu + N \rightarrow l + N' + meson \\
\text{CC/NC deep inelastic interaction :} &\quad \nu + N \rightarrow l + N' + hadrons \\
\text{CC/NC coherent pion production :} &\quad \nu +^{16} O \rightarrow l +^{16} O + \pi
\end{aligned} \tag{5.3}$$

where N and N' are protons or neutrons and l is a lepton. The cross-section of neutrino-electron interaction being a factor of a thousand smaller than the neutrino-nucleon interaction at ≈ 1 GeV it is not simulated here. Each mode is described briefly in the following subsections. These descriptions can be found in more details in G. Mitsuka's thesis [6].

5.2.1 Elastic and quasi-elastic scattering

The scattering of neutrinos off a free proton has been described by Llewellyn-Smith in Ref. [51]. For the scattering off bound nucleus of ^{16}O, nuclear effects like the Fermi motion, or the Pauli exclusion principle are dealt with following the work of Smith and Moniz [52].

In general, neutrino scattering off nucleon involves *form factors* [53]. Form factors are a way to describe the effect of the nucleon not being a pointlike particle. Form factors are usually labelled $F(q^2)$, where q^2 is the square of momentum transfer. The differential cross-section is therefore modified as follows:

$$\frac{d\sigma}{d\Omega} = \frac{d\sigma}{d\Omega_{pointlike}} \times F(q^2) \quad . \tag{5.4}$$

Empirically, it is found that the form factors can be fitted by the dipole formula:

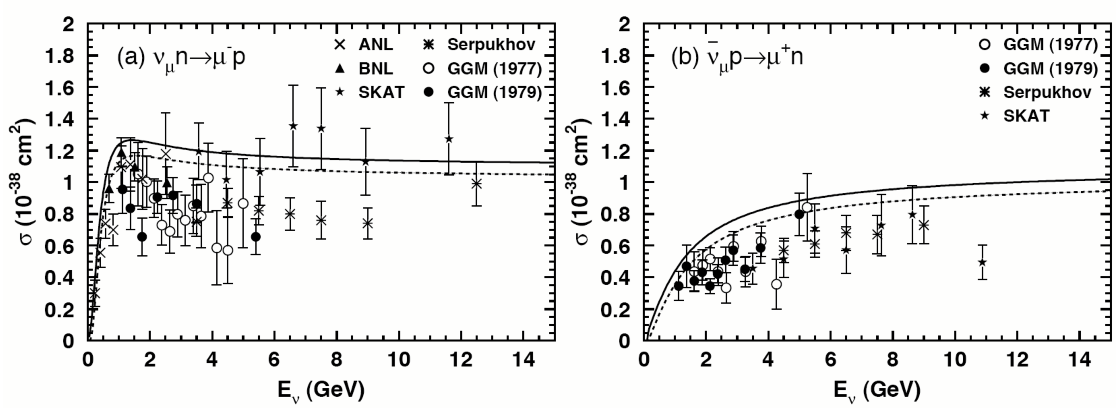

Figure 5.4: Quasi-elastic cross-sections for (a) ν_μ and (b) $\overline{\nu_\mu}$ computed with the NEUT library and with experimental data. The solid and dashed curves indicate the scattering of free and bound nucleon respectively [6].

$$F(q^2) \approx \frac{1}{(1 + q^2/M^2)^2} \quad , \tag{5.5}$$

where M is just a parameter determined by fitting to experimental data. In the case of neutrinos scattering, there are two form factors, one for vector couplings, specified by the vector mass M_V and one for axial vector couplings, specified by the axial vector mass M_A.

For reference, I give here the values of some parameters used in the simulation. The vector mass M_V is set to 0.84 GeV, and the axial vector mass M_A is set to 1.21 GeV according to experimental results [35, 54, 55]. The value of M_A is consistent with the value used by other experiments like K2K and MiniBooNE. The uncertainty on M_A is estimated to be 10%. The axial vector coupling constant g_A is measured in polarized nucleon beta-decay [56] and is set to 1.232. The Fermi surface momentum is set at 225 MeV/c. The cross-sections of quasi-elastic scattering for experimental data and calculation with the NEUT library are shown in Fig. 5.4. The solid and dashed curves indicate the scattering of free and bound nucleons respectively.

5.2.2 Single meson production

Meson production occurs through baryon resonances as shown in Eq. 5.6. We use the Rein and Sehgal model [57] to treat meson production. The model was first developed for single pion production but it was then modified to account for single η and kaon production. The value of M_A used for meson production is also set to 1.21 GeV. Single pions charged current cross-sections for muon neutrino a muon anti-neutrino are shown in Fig. 5.5 and Fig. 5.6.

$$\begin{aligned} \nu + N &\rightarrow l + N^* \\ N^* &\rightarrow N' + meson \end{aligned} \tag{5.6}$$

5.2.3 Deep inelastic scattering

When deep inelastic scattering occurs, several hadrons can be created, and we call these outgoing hadrons the hadronic system. We treat the case of single pion production separately as seen in the previous section. For reference, here are several parameters used to compute deep inelastic cross-sections. The GRV98 [58] parton distribution function is used, and the corrections from A. Bodek and U.K. Yang are applied [59]. The kinematics of the hadronic system is calculated with a different method depending on the invariant mass. For 1.3 GeV/c^2 $< W <$ 2.0 GeV/c^2, only outgoing pions are considered and for $W >$ 2.0 GeV/c^2 we use the PYTHIA/JETSET [60] package to simulate all sorts of outgoing mesons (not only π but also K, η, ρ, etc).

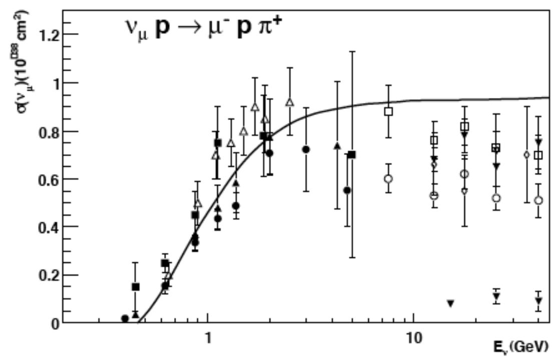

(a) $\nu_\mu p \to \mu^- p \pi^+$

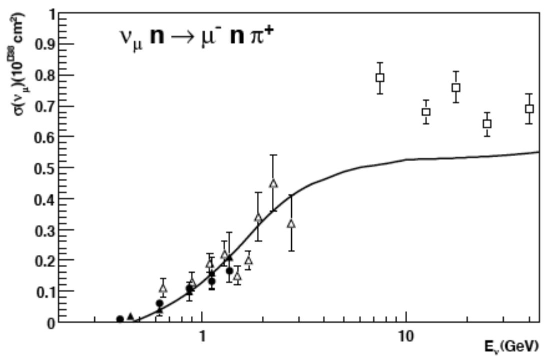

(b) $\nu_\mu n \to \mu^- n \pi^+$

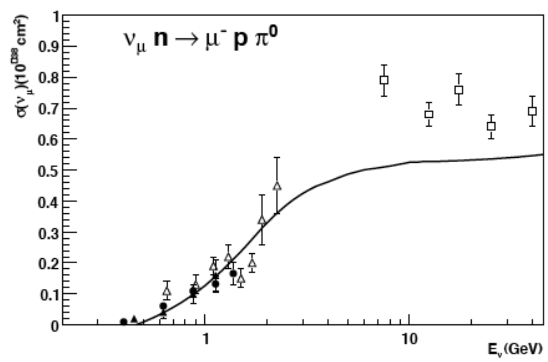

(c) $\nu_\mu n \to \mu^- p \pi^0$

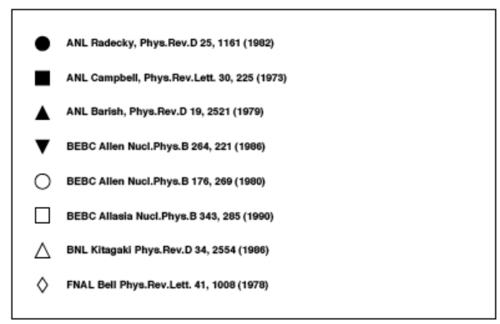

(d) The list of the experiments in this figure

Figure 5.5: Single π charged current cross-sections (ν_μ). Solid curves are the NEUT calculations, experimental data are overlaid and described in panel (d) [6].

5.2.4 Coherent pion production

Coherent pion production is a neutrino interaction with an oxygen nucleus, where the nucleus remains the same and a pion with the same charge as the incoming weak current is produced. Here again we use the formalism developed by Rein and Sehgal [61].

The measurements by the K2K-SciBar detector set an upper limit on the cross-section of charged current coherent pion production [62]. Since this upper limit is significantly lower than the predicted cross section, some modifications to the calculation were made by Rein and Seghal [63] and implemented in the simulation. The modifications account for the non-vanishing lepton mass in charged current interactions. This suppresses the cross section by about 25% at 1.3 GeV due to interference of the axial

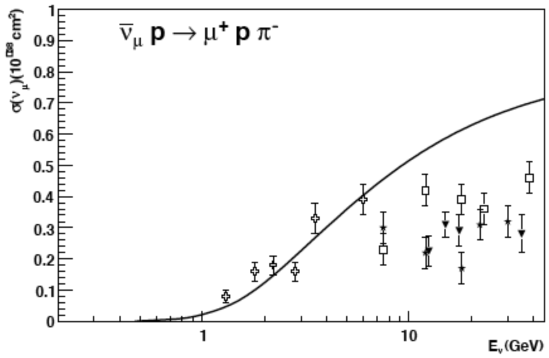

(a) $\overline{\nu}_\mu p \to \mu^+ p \pi^-$

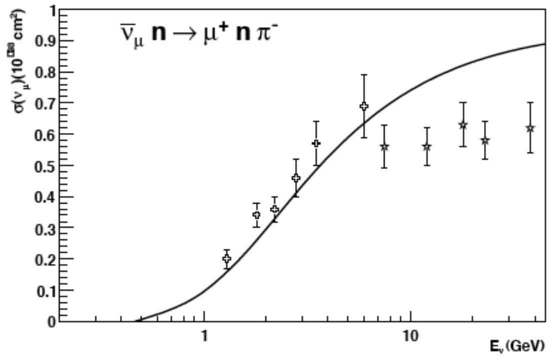

(b) $\overline{\nu}_\mu n \to \mu^+ n \pi^-$

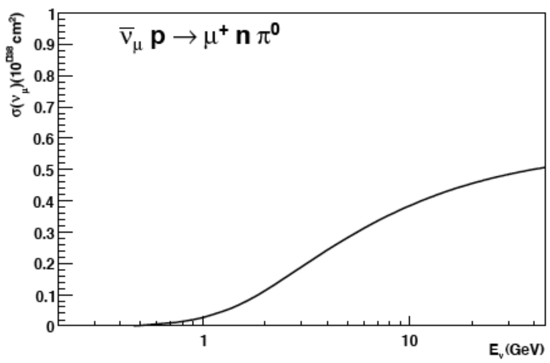

(c) $\overline{\nu}_\mu p \to \mu^+ n \pi^0$

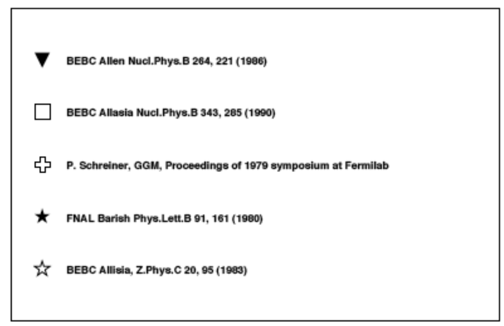

(d) The list of the experiments in this figure

Figure 5.6: Single π charged current cross-sections ($\overline{\nu_\mu}$). Solid curves are the NEUT calculations, experimental data are overlaid and described in panel (d) [6].

vector and the pseudo-scalar (pion-exchange) amplitudes. The cross sections for charged current and neutral current are shown in Fig. 5.8.

5.2.5 Nuclear effects

Secondary interactions of mesons which are produced in neutrino interactions with nucleons inside the ^{16}O nuclei also need to be simulated. In particular the interactions of pions are very important since the pion-nucleon cross-section is quite large for neutrino energies above 1 GeV. The pion interactions in the ^{16}O nuclei that have been considered are: inelastic scattering, charge exchange and absorption.

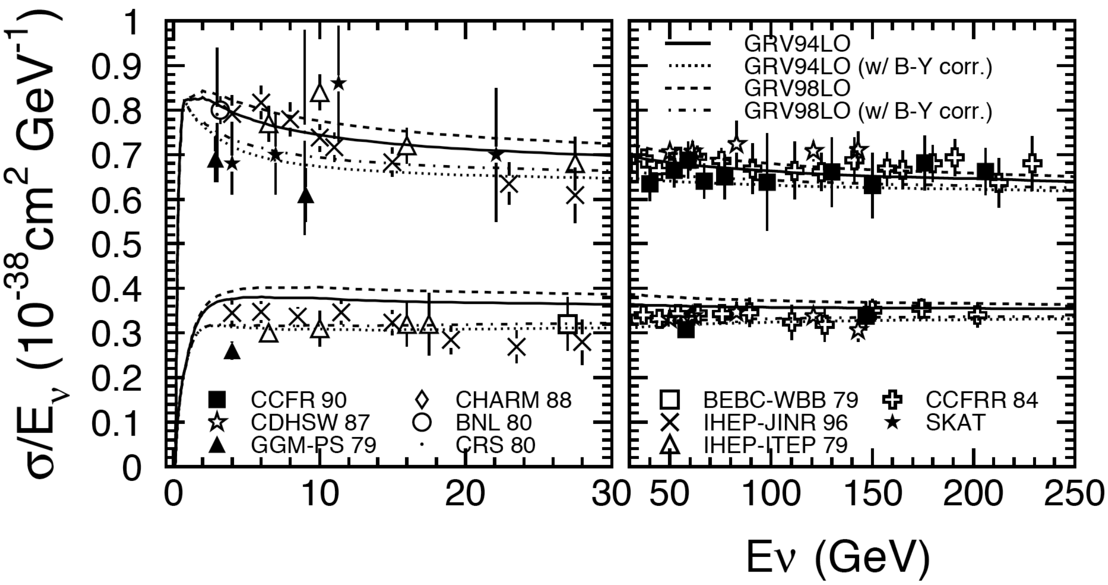

Figure 5.7: Deep inelastic cross-sections for charged current ν_μ and $\overline{\nu_\mu}$ interactions. Upper (lower) curves are for ν_μ ($\overline{\nu_\mu}$). NEUT calculations are shown for two different parton distribution calculation and with or without Bodek-Yang corrections. Experimental data are overlaid [6].

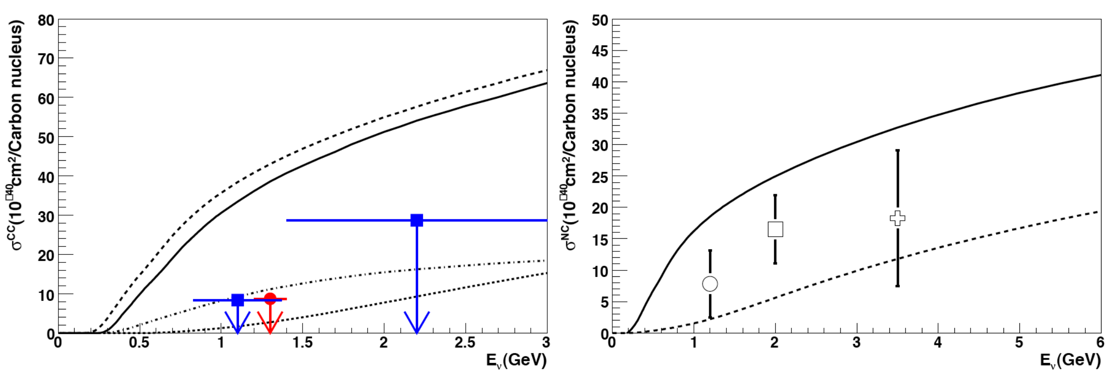

Figure 5.8: The cross sections for coherent pion production off the carbon nucleus for charged current interaction (left) and neutral current (right) by two models with experimental data. The solid, dashed and dotted curves stand for Rein and Sehgal with lepton mass effects, Rein and Sehgal without lepton mass effects, and Kartavtsev *et al.* respectively. On the left figure, the arrow indicates the experimental upper limit by K2K [62] and on the right experimental data are from CHARM, MiniBooNE, Aachen-Padova and Garmaelle [6].

5.3 Detector simulation

All the particles that are produced in the NEUT simulation are then processed with the detector simulation code. The detector simulation tracks the particle through water, generates Cherenkov light, propagates the light through the water, and finally simulates the PMT and the electronics response. The detector simulation is written with the GEANT3 package [64]. To simulate the hadronic interactions in water we use the CALOR package [65]. The complete list of processes which are simulated is given in Table 5.1. In order to estimate the systematic uncertainty on the hadron simulation, we compare the results of our detector simulation with the CALOR package, and the Fluka model. For the light propagation in water we consider Rayleigh scattering, Mie scattering, and absorption.

γ	(e^+,e^-) pair production Compton scattering Photoelectric effect
$e^\pm$	Multiple scattering Ionization and δ-rays production Brehmsstrahlung Annihilation of positron Generation of Cherenkov radiation
$\mu^\pm$	Decay in flight Multiple scattering Ionization and δ-rays production Direct (e^+,e^-) pair production Nuclear interaction Generation of Cherenkov radiation
Hadrons	Decay in flight Multiple scattering Ionization and δ-rays production Hadronic interactions Generation of Cherenkov radiation

Table 5.1: List of processes considered in the GEANT simulation.

Chapter 6

Data Reduction

The goal of *data reduction* is to select neutrino events out of the dataset selected by the trigger. The raw data is processed in real time by the first stage of reduction. The rest of the data reduction happens later. Before reduction, about 10^6 events are collected every day. Most of these are cosmic ray muons. Data reduction can be split into three categories. FC (fully-contained) reduction selects neutrino events for which none of the visible outgoing particles exit the inner detector and therefore have only a few hits in the outer detector for. PC (partially-contained) reduction selects neutrino events in which the outgoing lepton exits the inner detector and deposits a lot of energy in the outer detector. Finally UPMU (upward-going muon) reduction selects muon events going upwards. Upward-going muons are the result of neutrino interactions in the rock below the detector. A schematic view of each event sample can be found in Fig. 6.1. The FC and PC samples have the same livetime, while the UPMU sample, which is less sensitive to detector effects has a larger livetime. Since the UPMU sample is not used in the L/E analysis, it will not be described further.

The separation between FC and PC events is based on the number of hits recorded in the outer detector. The systematic error on this separation is 0.6% for SK1 and 0.5% for SK2.

I personally worked on improving PC reduction for the SK3 data-taking period, so in

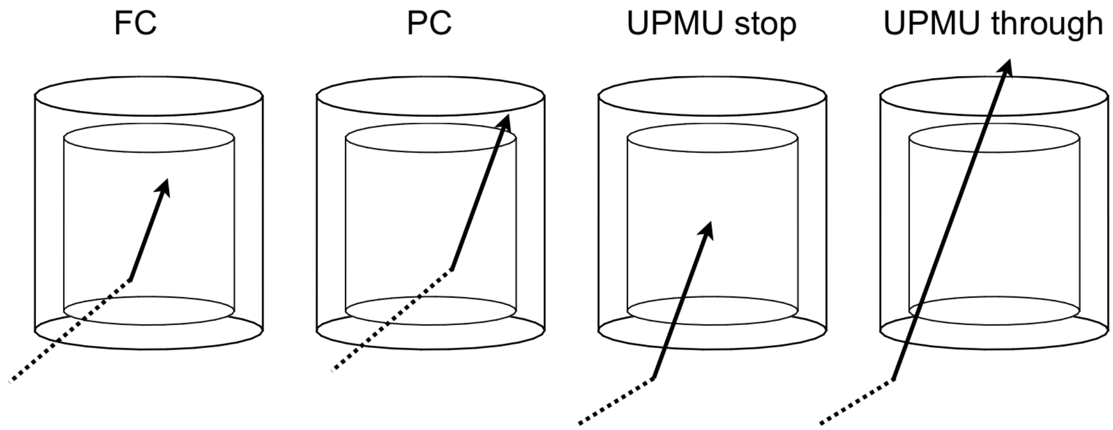

Figure 6.1: Schematic view of different event samples.

addition to presenting a brief overview of FC and PC reduction for SK1 and SK2 here, I will present the details of the PC reduction improvements for SK3 in Appendix A.

6.1 Fully-contained reduction

First I present an overview of the FC reduction results and then I describe the five levels of FC reduction in the following subsections.

6.1.1 First reduction

The goal of the first reduction is to remove low energy background due to radioactive decay and to remove cosmic ray muons. The cuts applied in the first reduction must be very stable and quite loose since the first reduction is run online. The goal is to not go back to the raw data but rather go back to the output of the first reduction if a reduction algorithm is improved.

- $\texttt{PE}_{300}$: The number of photoelectrons in the ID within a 300 ns sliding time window needs to be greater than 200 for SK1 and 100 for SK2. $\texttt{PE}_{300} \geq 200(100)$.

- $\texttt{NHITA}_{800}$: This is the number of hits in the outer detector in a fixed time window that runs from 400 ns before the ID trigger to 400 ns after. $\texttt{NHITA}_{800} \leq 50$ or the OD trigger must be off.

- TDIFF: This is the time interval between that last event and this one. We require that $\texttt{TDIFF} \geq 100\mu s$ so that we can reject electrons created by the decay of stopping muons.

After these cuts the event rate is about 3000 events per day for SK1 and 2200 events per day for SK2.

6.1.2 Second reduction

Second reduction has the same purpose as first reduction and is based on the same cuts but with tighter values, but it is run offline as are all reduction stages following FC2.

- $\texttt{PE}_{\texttt{max}}/\texttt{PE}_{300} < 0.5$: With PE_{max} being the maximum number of photoelectrons seen in one PMT and $\texttt{PE}_{300}$ being the same as in the first reduction. The goal of this cut is to remove flasher events (flasher events are described in Section 6.1.3.)

- $\texttt{NHITA}_{800}$: $\texttt{NHITA}_{800} \leq 25$ if $\texttt{PE}_{\texttt{tot}} < 100000$ (50000) p.e. for SK1 (SK2), or the OD trigger must be off.

After the second reduction step, the event rate is about 200 events per day for SK1 and 280 events per day for SK2.

6.1.3 Third reduction

Third reduction is still aimed at rejecting the remaining cosmic ray events and noise events, but now more elaborate (and time-consuming) tools are applied.

Through-going muon cut

Since through-going muon are cosmic ray muons deposit a lot of charge in the inner detector and leave an entrance and an exit charge cluster in the outer detector. We apply the following set of cuts, which uses a special muon fitter.

- $\texttt{PE}_{\texttt{max}} > 250$ p.e.: If one of the ID PMT receive more than 250 p.e.s then the following cuts are applied. In the SK2 case, we also ask that the total number of hit in the ID be greater then 1000.

- $\texttt{mugood} > 0.75$: The goodness of the muon fit must be better than 0.75

- $\texttt{NHITA}_{\texttt{in}} \geq 10$ or $\texttt{NHITA}_{\texttt{out}} \geq 10$: The number of hit PMTs in the OD within 8 meters of the entrance (in) or exit (out) point must be greater than 10 in a 800 ns time window.

Stopping muon cut

To remove stopping muons, we also use the muon fitter used for the though-going muon cut.

- $\texttt{mugood} > 0.5$ and $\texttt{NHITA}_{\texttt{in}} \geq 5$ OR $\texttt{NHITA}_{\texttt{in}} \geq 10$: where the definitions of `mugood` and $\texttt{NHITA}_{\texttt{in}}$ are the same as for the through-going muon cut.

Cable hole muon cut

We need to remove cosmic ray muons that enter through the cable holes described in the detector section 4.2. We remove events that have the following characteristics:

- One hit in the veto counter.

- $\texttt{l}_{\texttt{veto}} < 4$m : The vertex must be within 4 meters of the cable hole.

Flasher events

Flasher events are due to mis-behaving PMTs. The timing distribution of such events is usually wider than the timing distribution of neutrino events. Events satisfying the following criteria are considered flasher events and removed from the neutrino sample.

- For SK1: $\texttt{NMIN}_{\texttt{100}} \geq 14$ or $\texttt{NMIN}_{\texttt{100}} \geq 10$ if the number of hit ID PMT is less than 800. $\texttt{NMIN}_{\texttt{100}}$ is the minimum number of ID hits in a 100 ns time window.

- For SK2: $\texttt{NMIN}_{\texttt{100}} \geq 20$

Accidental muon cut

Sometimes, a cosmic ray event happens just after a low energy event. If the two events are in the same trigger gate, the event is hard to reject because there will be no OD activity during the trigger gate, but enough photoelectrons (coming from the muon) in the ID to keep the event. To reject such events, we apply the following two cuts:

- $\texttt{NHITA}_{\texttt{OFF}} > 20$: The number of hit OD PMTs in the fixed 500 ns time window from 400 ns to 900 ns after the trigger is greater than 20.

- $\texttt{PE}_{\texttt{off}} > 5000$ (2500) p.e.: The number of photoelectrons in the ID in the 500 ns time window is greater than 5000 (2500) for SK1 (SK2).

Low energy muon cut

Low energy events from electronic noise and radioactive decay are removed at this stage by applying the following cut:

- $\texttt{NHIT}_{\texttt{50}} < 50$ (25): The number of ID hits within a 50 ns sliding time window is less than 50 for SK1, 25 for SK2. To decide whether a hit PMT is in the 50 ns time window, we take into account the time of flight of the photons assuming they all come from the same vertex. In this case the vertex is defined as the position at which the residual time distribution peaks. $\mathtt{NHIT}_{50} = 50$ corresponds to a 9 MeV event.

After the third reduction step, the event rate is about 45 events per day for SK1 and 21 events per day for SK2.

6.1.4 Fourth reduction

The goal of the fourth reduction step is to remove the remaining flasher events. Flasher events occurs when light is emitted from the discharge of the PMT dynodes. It usually takes time before such bad PMTs are identified and turned off, so we have to remove flasher events in the reduction process. The characteristic of flashers is that the light pattern emitted by these events repeats over a long period of time. By looking for such repetition we are able to remove these events. More details about how this search is performed was described previously [66].

The event rate after the fourth reduction is about 18 events per day for both SK1 and SK2.

6.1.5 Fifth reduction

The fifth (and last) reduction is a set of very specific cuts designed to remove the remaining non neutrino events.

Stopping muon cut

This cut is similar to the cut applied in the third reduction, but the entrance point is now computed by extrapolating backward the fitted track of the event instead of using the earliest hit PMT. The cut is now:

- $\mathtt{NHITA}_{\mathtt{IN}} \geq 5$ where $\mathtt{NHITA}_{\mathtt{IN}}$ is defined as before.

Invisible muon cut

When a cosmic ray muon is below the Cherenkov threshold it is not seen in the detector but its decay electron can be seen. Such events are called invisible muons and are removed with the following set of cuts:

- $\mathtt{PE}_{\mathtt{tot}} < 1000$ (500): The total number of photoelectrons in the ID is less than 1000 for SK1 and 500 for SK2.

- $\mathtt{NHITA}^{\mathtt{max}}_{\mathtt{early}} > 4$: The maximum number of hit OD PMTs in a 200 ns time window going from 8900 ns to 100 ns before the trigger is greater than 4.

- $\mathtt{NHITA}^{\mathtt{max}}_{\mathtt{early}}+\mathtt{NHITA}_{\mathtt{500}} > 9$ if $\mathtt{l}_{\mathtt{cluster}} < 500cm$ or $\mathtt{NHITA}_{\mathtt{early}} > \mathtt{9}$ otherwise. $\mathtt{NHITA}_{\mathtt{500}}$ is the number of hit OD PMTs in a 500 ns time window from -100 ns to 400 ns. $\mathtt{l}_{\mathtt{cluster}}$ is the distance between two OD clusters used during the calculation of $\mathtt{NHITA}_{\mathtt{early}}$ and $\mathtt{NHITA}_{\mathtt{500}}$.

Coincidence muon cut

The remaining accidental events are removed using the following two cuts:

- $\mathtt{PE}_{\mathtt{500}} < 300$ (150)p.e.s: The total number of photoelectrons within a 500 ns time window going from -100 ns to 400 ns is less than 300 for SK1 and 150 for SK2.

- $\mathtt{NHITA}^{\mathtt{max}}_{\mathtt{late}} > 20$: The number of hit OD PMTs in a 200 ns sliding window going from 400 ns to 1600 ns after the trigger is greater than 20.

Long tail flasher cut

This a tighter version of the cut applied in the third reduction. Events are removed if they satisfy the following condition:

- For SK1: $\texttt{NMIN}_{100} > 5$ if the goodness of point fit is < 0.4: The minimum number of hit ID PMTs in a 100 ns sliding time window from 300 ns to 800 ns after the trigger is greater than 5.

- For SK2, the SK1 cut is applied and in addition we ask that the goodness of point fit be < 0.3 and that $\texttt{NHITMIN}_{100} < 6$.

The event rates at the end of the fifth reduction step are about 16 events per day for both SK1 and SK2.

6.1.6 Final FC cuts

The last cuts to be applied to select the fully-contained sample are the following:

- `FV cut`: the fiducial volume cut where we require an event to have a reconstructed vertex located at more than 2 meters from the wall of the inner detector. For the L/E analysis, we relax the fiducial volume cut a little bit. In that case, the vertex must be 1.5 meters away from the endcaps (top and bottom) and 1 meter away from the wall.

- `NHITAC`: We require that the number of hits in the outer detector be less than 10 for SK1 and 16 for SK2. This is the separation between FC and PC events.

- `Evis`: The visible energy must be greater than 30 MeV. The visible energy is defined as the energy of an electro-magnetic shower that produced a given amount of Cherenkov light.

These final cuts are not applied for every analysis, in the case of the L/E analysis for example, the fiducial volume is extended as seen in the next Chapter. At the end of the reduction process the event rate of the FC sample is 8.18 ± 0.07 and 8.26 ± 0.10 events per day for SK1 and SK2 respectively.

6.1.7 Status for SK1 and SK2 datasets

The efficiency of FC reduction used in SK1 and SK2 is summarized in Table 6.1. The numbers for SK1 are taken from the Super-K paper [1], while the numbers for SK2 are taken from collaboration meeting slides and can be found in other Super-Kamiokande PhD. theses [6, 66].

	SK1 (1489 days)		SK2 (804 days)	
	Efficiency	Data	Efficiency	Data
Trigger	100%	1889599293	100%	
FC1	99.95%	4591659	99.92%	
FC2	99.94%	301791	99.89%	
FC3	99.85%	66810	99.71%	
FC4	99.17%	26937	99.39%	
FC5	99.15%	23984	99.32%	
FC5 (FV + visible energy cuts)	97.59%	12180	99.17%	6605

Table 6.1: SK1 and SK2 FC reduction summary.

The background contamination for FC events was evaluated in two different energy regimes, below 1.33 GeV (sub-GeV events) and above 1.33 GeV (multi-GeV events). The summary of the upper limits on each kind of background is presented in Table 6.2. The systematic error on FC reduction is 0.2% for SK1 and SK2.

	Sub-GeV $E_{vis} < 1.33$ GeV/c		Multi-GeV $E_{vis} > 1.33$ GeV/c	
SK1	e-like (%)	μ-like (%)	e-like (%)	μ-like (%)
Cosmic ray μ	-	0.07	-	0.09
Flashing PMT	0.42	-	0.16	-
Neutron events	0.1	-	0.1	-
SK2				
Cosmic ray μ	-	0.01	-	0.07
Flashing PMT	0.27	-	0.65	-
Neutron events	0.1	-	0.1	-

Table 6.2: SK1 and SK2 FC background contamination upper limits.

6.2 Partially-contained reduction

The goal of most of the PC reduction process is to remove cosmic ray muons. There are two kinds of cosmic ray muons: through-going muon events which enter and exit the inner detector and deposit two charge clusters in the OD, and stopping muon events which deposit an entrance charge cluster in the OD and stop in the ID. There are five levels of PC reduction and the first reduction is run online.

6.2.1 First reduction

The cuts used in PC1 must be very simple and very stable since the first reduction is run online.

- $\texttt{PE}_{\texttt{tot}}$: The total number of photoelectrons observed in the ID must be greater than 1000 (500 for SK2).
- `TWIDA`: The width of the timing distributions of OD PMTs must be smaller than 260 ns for SK1 (170 ns for SK2).
- `NCLSTA`: The number of hit clusters in the OD must be equal or greater than 1. (Cut applied only for SK1)

6.2.2 Second reduction

PC2 uses very simple cuts, looking at variables like the number of hits in the OD or the charge to remove cosmic ray muons. This reduces the number of events for which we have to run time-consuming fitters.

- `Numendcap vs numwall`: (SK2) We look at the number of hits in the endcaps of the detector and compare it to the number of hits in the wall. If the number of hits in the endcap is smaller than the `maxendcap(numwall)` then the event is

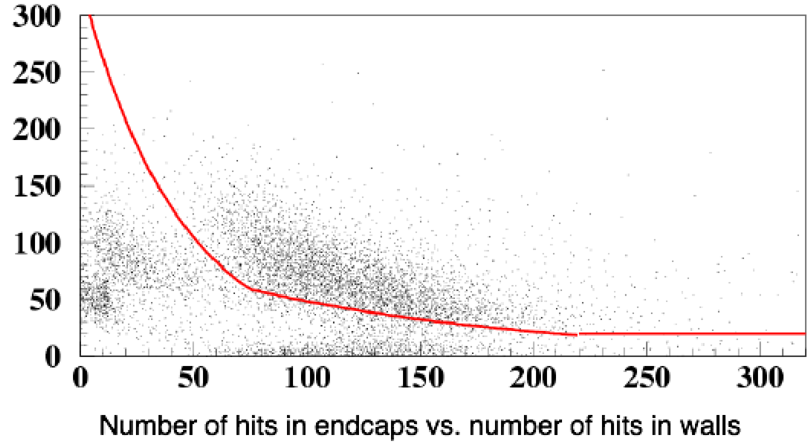

Figure 6.2: Number of hits in the OD endcaps versus number of hits in the OD wall. Events that are above the red line (`maxendcap`) are corner clippers events and are rejected during PC reduction.

kept. This cut is designed to remove cosmic ray muons that clip the corner of the detector (corner clipper events).

- `Nouter2`: Number of hits in the second highest charge OD cluster. An event passes this cut if `nouter2` ≤ 10. This cut is used to remove through-going cosmic ray muons.

- `Nouter`: Number of hits in the highest charge OD cluster. An event passes this cut if `nouter` ≤ 6. This is to remove both kind of cosmic ray muons. If events have more than 6 hits then they are part of a conditional cut with `PE200` (next cut).

- `PE200`: Number of photoelectrons within 200 cm of the highest charged PMT in the ID hit cluster closest to the OD hit cluster. This cut is combined with the `nouter` cut such that an event passes the cut if (`nouter` $<$ (12+ `pe200` $/2.0 * (80. - 12.)/800.$)). This cut is used to remove stopping events.

In order to pass PC2 an event has to satisfy the following criteria:

`((numendcap vs numwall).and.(nouter2).and.(nouter.or.pe200)`

6.2.3 Third reduction

- `Flashtest:` Results of the function flasher test. This cut is used to removed flasher events due to electronic noise.

- `Ehit8m:` This is the number of hit OD PMTs located within 8m of the entrance point in a fixed 500 ns time window. The entrance point is extrapolated using the `pfit` direction. We require `ehit8m` ≤ 10 to pass the cut. This cut removes both stopping and through-going muon events.

  We ask an event to pass both cuts in order to be kept.

6.2.4 Fourth reduction

PC4 mainly uses the muon fitter `mfmufit` and the point fitter `pfit`.

- `Qismsk:` Total charge in the inner detector. This is to remove events with too little energy in the ID. The cut is set at 1000 in PC4 and then at 3000 in PC5.

- `Mu distance:` This is the track length given by `mfmufit`. Long track lengths are associated with cosmic ray muons. An event passes the cut if `Mu distance` < 3000.

- `Mu good:` This is the goodness of the `mfmufit`. The goodness of fit is good only for true muons, therefore we keep events with a bad goodness of fit. An event passes the cut if `Mu good` < 0.85.

- `Dcorn:` This is the distance between the vertex found by `pfit` and the corner of the tank. An event passes the cut if `dcorn` > 150. This removes events that are outside the fiducial volume anyway, but it is convenient to remove these events at this stage, as they would slow down PC5.

- `Dot product:` This is the dot product between the `pfit` direction ($\vec{d}_{pfit}$) and the vector linking the `pfit` vertex and the earliest saturated ID PMT ($\vec{d}_{pmt}$). An event passes the cut if `dot product` $= \vec{d}_{pfit} \cdot \vec{d}_{pmt} > -0.85$. This cut eliminates cosmic ray muons that are likely to have $\vec{d}_{pfit}$ and $\vec{d}_{pmt}$ in the opposite direction.

An event is kept if:

`(qismsk).and.(dcorn).and.(dot product).and.((mu good) .or.(mu distance))`

6.2.5 Fifth reduction

PC5 is split into two distinct parts. Fast cuts that do not use any precise fitter, and slow cuts that use several fitters like `apfit`, MS-fit (`msfit`) and others. These fitters are described in more detail in the next chapter.

Fast cuts

First there are two very basic cuts to select partially-contained events.

- `Nhitac:` This is the number of hits in the OD. We use this cut to decide whether an event is fully-contained (`nhitac`< 16) or partially-contained (`nhitac`≥ 16).

- `Qismsk:` This is the total charge in the ID. We keep events which have `qismsk`$>$ 3000.

Then there are a set of very simple cuts, using only OD information, and designed to remove through-going muon events.

- `Nodcluster3:` This is the number of hits in the third highest charged OD cluster. If `nodcluster3`<2 then an event passes this cut.

- `Distod12:` This is the distance between the first and second highest charge OD clusters. If `distod12`≤ 2000 then an event passes this cut. A very large distance would be an indication of a through-going muon.

- `Odclustq2:` This is the amount of charge in the second highest charge OD cluster. If `odclustq2`<10 then an event passes this cut.

If an event passes at least one of these three cuts, it is kept.

Finally we use two cuts to remove events coming from calibration runs (`calsel cut`), or from runs where there was a problem with some of the electronics huts (`deadsel cut`). Only events that pass the fast cuts are passed on to the slow cuts.

Slow cuts

There are several kinds of slow cuts. Cuts designed to remove junk events, stopping muons, through-going muons, corner clippers and low energy events.

Junk cut:

- ``` ``Bye Bye'' cut: ``` This cut is designed to remove events that were spread across two triggers.

- `NO ID:` This cut removes events where the ID data is missing.

- `Ano OD:` This cut removes events where the OD malfunctioned.

Muon cuts: There is one cable hole muon cut, four stopping muon cuts and three through-going muon cuts.

Cable hole muon:

There are veto scintillation counters placed over the four cable holes on top of the detector (see Chapter 4). The cut criteria to remove a cable hole muon are the following:

- `Veto:` One veto counter hit.
- $\vec{d}_{ring} \cdot \vec{d}_{veto-vertex} > -0.8$, where $\vec{d}_{ring}$ is the reconstructed ring direction, and $\vec{d}_{veto-vertex}$ is the direction from the hit veto counter to the reconstructed vertex.

<u>Stopping muons:</u>

The stopping muons cuts rely on finding a cluster of OD hits close to an entry cluster in the ID.

- `Stop mu:` Number of entry hits based on the `msfit` fitter results. If more than 10 entry hits are found, then the event fails this cut.
- `Cone:` This cut uses the charge information in the opposite direction of the `stmfit` direction. First, we check that the `stmfit` goodness is greater than zero. Then we define a cone of 8 m radius, in the backward direction found by the `pfdofit` fitter. We also check that 60% of the ID charge is in the cone. If there are more than 6 hits in this cone, then the event is rejected.
- `Hits:` This cut is the same as the `ehit8m` cut in PC3, but instead of using `pfit`, we now use the precise fitter `apfit`. If more than 10 hits are found close to the entry point, the event fails the cut.
- `Angle:` This cut uses the angle between a fitted direction and a vector linking a fitted vertex and the center of the highest charge OD cluster. Two fitters are used, the standard precise fitter `apfit` and `msfit`. If any of the angles are above 90° then the event is rejected.

<u>Through-going muons:</u>

The through-going muon cuts rely on finding two clusters in the OD, an entry cluster and an exit cluster.

- `Geji:` This cut is used to remove "Geji" events. Those are cosmic ray muons that are traveling vertically downwards in the volume between the ID and the OD. They leave a "millipede-type" track in the ID which explains their name. (i.e. millipede = geji in Japanese)

- `Cluster:` Using an algorithm called `grad cluster`, we look at the number of hits in the first and in the second OD cluster. We ask the number of hits in the first cluster to be less than 10 and the number of hits in the second OD cluster to be less than 10.

- `Through mu:` This cut uses the number of entry and exit hits based on `msfit` results. If there are more than 4 entry hits and more than 4 exit hits and if the variable `thtoflen` is between 0.75 and 1.5 then the event is rejected. The variable `thtoflen` is the time difference between average hit time in the top and bottom OD clusters divided by the distance between the entry and exit points.

<u>Corner Clipper:</u>

- `New evis:` This cut is used to reject mis-reconstructed corner clipper muons using the relation between the visible energy given by `apfit` and the track length from the `apfit` vertex to the OD exit position.

<u>Low Evis:</u>

- `Evis:` This cut is used to remove events that have a visible energy less than 350 MeV and are inside the fiducial volume.

An event has to pass all the PC5 cuts to be accepted in the final PC sample.

6.2.6 Status for SK1 and SK2 datasets

The efficiency of PC reduction used in SK1 and SK2 is summarized in Table 6.3. The numbers for SK1 are taken from the Super-K combined paper [1]. The SK2 numbers are from collaboration meeting slides.

	SK1 (1489 days)		SK2 (804 days)	
	Efficiency	Data	Efficiency	Data
PC1	99.0%	1889599293	98.7%	
PC2	94.2%	34536269	94.3%	
PC3	93.1%	5257443	93.1%	
PC4	87.9%	380053	85.8%	
PC5	84.4%	1483	84.3%	678
PC5(FV)	79.7%	911	79.4%	427

Table 6.3: SK1 and SK2 PC reduction summary.

The background contamination in the PC sample comes mainly from cosmic ray muons. The background estimation is simply done by scanning the final data sample and counting how many non-neutrino events are found inside the fiducial volume. For SK1 the background contamination was 0.2% and for SK2 it was 0.7%.

The PC systematic uncertainties for PC1 to PC4 were estimated using two methods. For ID cuts, the uncertainty of each cut was estimated by comparing data and MC. For OD cuts, the uncertainty was estimated by creating several sets of Monte Carlo with slightly different OD tuning parameters and studying how these changes affected the PC efficiency. The uncertainty of the last step of PC reduction was again estimated by comparing distributions of cut variables between data and Monte Carlo. All the uncertainties were then added in quadrature. A more detailed description of the uncertainty calculation is done in Ref. [67]. The final PC uncertainty for SK1 is 2.4% and for SK2 is 4.8%. The final event rate at the end of PC reduction is 0.61 ± 0.02 (0.53 ± 0.03) events per day for SK1 (SK2).

Chapter 7

Data Reconstruction

Events that pass all the reduction steps are then reconstructed in order to be used in analyses. The energy, the number of rings, the type of rings (electron or muon), and the vertex of the interaction are some of the variables that are computed during the reconstruction. In this Section, I will describe how the main variables that characterize an event are computed. For comparison of data versus Monte Carlo of standard variables, see Appendix B. The name of the algorithms are written for reference, and the master routine that runs the entire reconstruction is called `apfit`.

7.1 Vertex fitting (`tfafit`)

The vertex is the first variable to be reconstructed. To do so, we apply a "3 steps" fit. This is the first attempt at fitting the vertex and it will be improved later in the reconstruction process.

7.1.1 Point fit (`pfit`)

First we look for a rough vertex position, assuming that all the light comes from a single point source using the timing information of all PMT's. We defined the goodness of the point-fit vertex G_P as in the following equation:

$$G_P = \frac{1}{N} \sum_i \exp\left(-\frac{(t_i - t_0)^2}{2(1.5 \cdot \sigma)^2}\right), \tag{7.1}$$

where N is the number of hit PMT's, t_i is the residual time of the i^{th} (ie. the difference between the hit time of the PMT t_i^0 and the time of light of the photon between the PMT and the vertex candidate), t_0 is a free parameter representing the time of the interaction, σ is the timing resolution (2.5 ns) and the 1.5 factor is there to improve the performance of the fit.

Depending on the position of the vertex, the time of flight of each photon is different, and the algorithm looks for the position which maximizes G_P.

Once the point-fit fitter finds a vertex, a rough direction is also calculated using:

$$\vec{d_0} = \sum_i q_i \times \frac{\vec{P_i} - \vec{O_0}}{|\vec{P_i} - \vec{O_0}|}, \tag{7.2}$$

where $\vec{O_0}$ is the vertex position found by point-fit, $\vec{P_i}$ is the position of the i^{th} PMT and q_i is the detected charge in the i^{th} PMT.

7.1.2 Ring edge search

Then we look for the edge of the main ring, and we compute a more precise direction. The ring edge is found by looking at the distribution of observed photo-electrons as a function of the angle of each PMT and the direction given by point-fit. The direction is then varied around the point-fit direction in order to maximize the estimator defined as:

$$Q(\theta_{edge}) = \frac{\int_0^{\theta_{edge}} PE(\theta) d\theta}{\sin \theta_{edge}} \times \left(\left. \frac{dPE(\theta)}{d\theta} \right|_{\theta=\theta_{edge}} \right)^2 \times \exp\left(-\frac{(\theta_{edge} - \theta_{exp})^2}{2\sigma_\theta^2}\right), \tag{7.3}$$

where θ_{exp} is the expected Cherenkov opening angle from the charge within the cone,

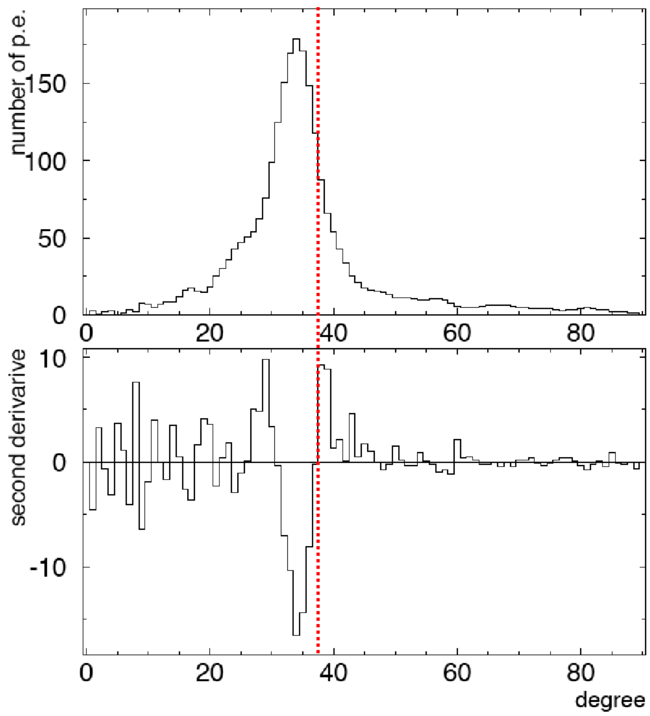

Figure 7.1: Example of $(PE(\theta))$ and its second derivative. The value of θ_{edge} in this example is shown by the red dotted line.

σ_θ is the resolution of θ_{exp}, $(PE(\theta))$ is the angular distribution of the observed charge as a function of the particle direction. The observed charge is corrected to take into account the water transparency. We choose θ_{edge} such that it is the first angle after the peak in $(PE(\theta))$ $(\theta_{edge} > \theta_{peak})$ for which the second derivative of $(PE(\theta))$ is equal to zero. This means that we look for the first inflection point after the peak in the $(PE(\theta))$ distribution. We also vary the particle direction around the direction found by point-fit such that it maximizes the $Q(\theta_{edge})$ estimator.

7.1.3 TDC-fit (`tftdcfit`)

Finally, we consider the fact that photons are emitted all long the path of the particle and not from a point source and the fact that photons can scatter in order to improve the vertex position found by point-fit.

The residual time is now computed differently whether a given PMT is located inside or outside of the Cherenkov cone, and the estimator is split into three parts. G_I for PMTs located inside the cone, G_{O1} for PMTs located outside the cone and with $t_i < t_0$ and G_{O2} for PMTs located outside the cone and with $t_i > t_0$.

7.2 Ring counting (`rirngcnt`)

In some cases, more than one Cherenkov ring is produced in the detector. Therefore, after finding the vertex and the first Cherenkov ring, the next step is to look for other rings. The purpose of the ring counting algorithm is not only to find the other rings, but also to determine their direction. The algorithm is made of two parts. First we look for any additional ring, and then we check if the candidates are true or not using a likelihood method.

7.2.1 Ring candidate search

In order to find ring candidates, we use the Hough transform method [68]. Consider a circle of a given radius, and draw circles of the same radius centered on each point of the first circle. All of these new circles will intersect at the center of the first circle. This is shown in Fig. 7.2. The shaded ring is the Chrenkov ring seen in the Super-Kamiokande detector. We draw a virtual ring (dashed lines) with a 42° angle around each hit PMT. The center of the Cherenkov ring is the point where all the virtual rings interesect. In practice, we also have to take into account the detector geometry and the charge information. To do so we use the expected charge distribution function ($f(\theta)$) weighted by the observed charge instead of virtual rings. We then map $f(\theta)$ on a (Θ, Φ) plane for each hit PMT. As a result, in the (Θ, Φ) plane the center of ring candidates are visible as peaks (see Fig. 7.3). This method was described extensively in S.T. Clark's PhD thesis [69].

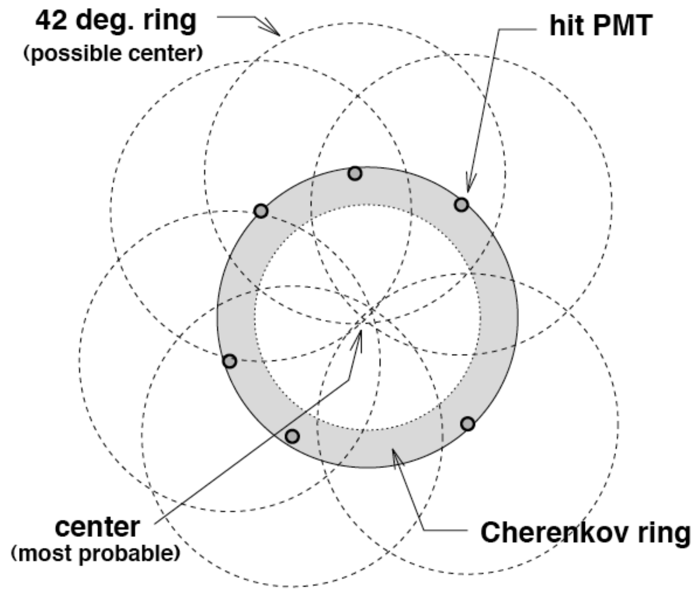

Figure 7.2: Schematic view of a Hough transform for a radius of 42° [6].

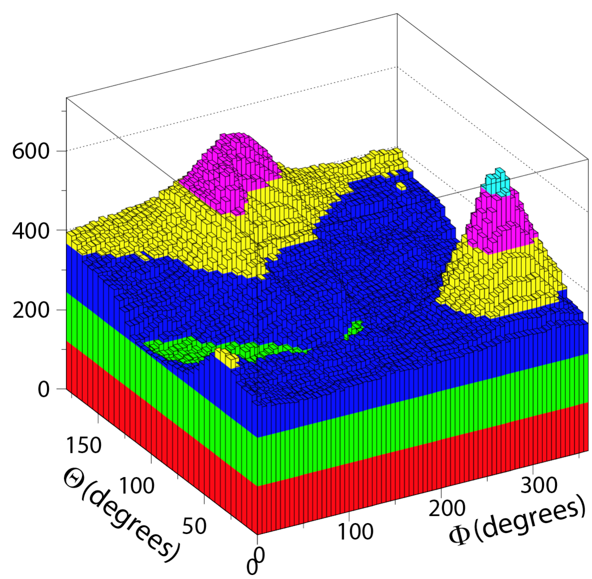

Figure 7.3: A charge map from Hough transformation alogrithm for a typical two ring events. The peak are the centers of the Cherenkov rings [6].

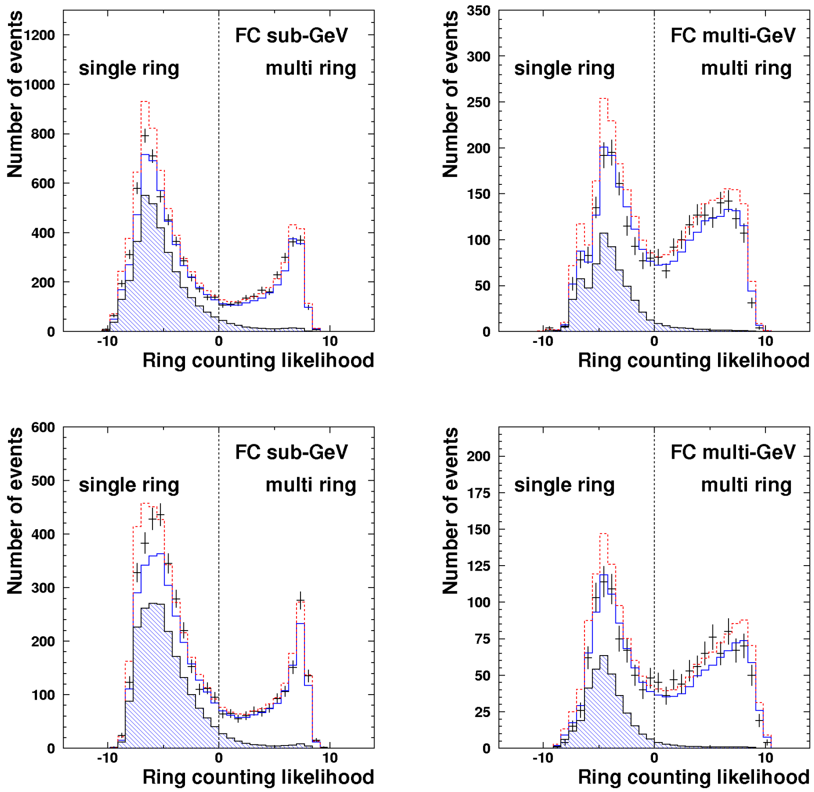

Figure 7.4: Ring counting likelihood for FC Sub-GeV events (left) and Multi-GeV events (right) of data (black dot) and Monte Carlo events (blue solid line) assuming 2 flavor $\nu_\mu \rightarrow \nu_\tau$ oscillation with $(\sin^2 2\theta, \Delta m^2) = (1.00, 2.5 \times 10^{-3} eV^2)$, CCQE events are in blue hatched histograms, and red solid line is the unoscillated Monte Carlo. SK1 is on top, SK on the bottom.

7.2.2 Ring candidate test

After the ring candidates are found, we need to evaluate whether they are good rings or not. This process is based on likelihood functions and the evaluation of a set of 4 (6) functions for SK1 (SK2). If N rings have been found, then the $N+1$ ring is analyzed following this technique. If the $N+1$ ring is a good ring, the process starts over from the Hough transform. The ring candidate test has been described extensively by S.T. Clark [69] and Y. Takenaga [66]. The ring counting likelihood is shown in Fig. 7.4 for SK1 and SK2.

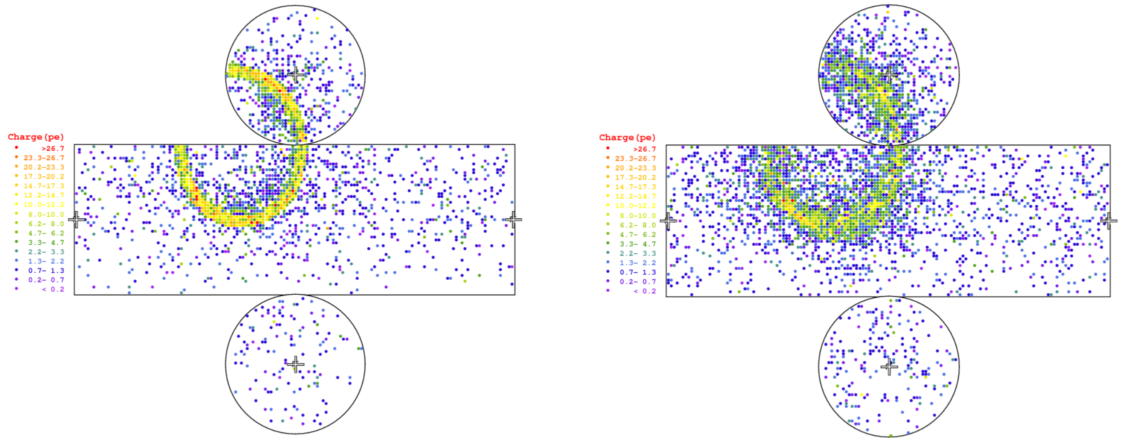

Figure 7.5: Example 1 GeV muon (left) and 1 GeV electron (right), in the SK1 detector.

7.3 Particle Identification (`sppatid`)

The goal of the particle identification is to determine the type of a particle. Knowing the flavor of the lepton emitted during the neutrino interaction is useful to determine the flavor eigenstate of the neutrino at the time of the interaction. Electron events create electro-magnetic showers and therefore the Cherenkov rings produced by electrons tend to by "fuzzy". Muon events, on the other hand, do not create showers, and their rings tend to have a very clear edge. The particle identification algorithm is based on these ring properties and classifies events into 2 categories: e-like and μ-like. Electrons and photons produce e-like events while muons and other heavy particles such as pions or kaons produce μ-like events. In addition, while electrons and photons produce Cherenkov rings with an opening angle of 42°, muons and other heavy particles can produce rings with a slightly smaller opening angle if they are not highly relativistic. This feature will also be used for the identification of protons presented in Appendix D, which also describes the selection of a CCQE sample. An example of e-like and μ-like events are presented in Fig. 7.5. The rate of mis-identification is computed using cosmic ray muons that decay in the detector, therefore provided a good sample of both muon and electron events.

7.3.1 Expected charge distributions

First, we compute the expected charge distributions for an electron and for a muon. For an electron, the expected charge deposited in the i-th PMT is calculated as follow:

$$q_i^{exp}(e) = \alpha_e \times Q^{exp}(p_e, \theta_i) \times \left(\frac{R}{r_i}\right)^{1.5} \times \frac{1}{\exp(r_i/L)} \times f(\Theta_i) + q_i^{scatt}, \tag{7.4}$$

where

α_e	:	normalization factor
r_i	:	distance from vertex to i-th PMT
θ_i	:	opening angle between the i-th PMT direction and the ring direction
L	:	light attenuation length in water
$f(\Theta_i)$	:	correction for the PMT acceptance as a function of the photon incidence angle Θ_i
R	:	radius of the virtual sphere (16.9 m)
$Q^{exp}(p_e, \theta_i)$	:	expected p.e. distribution from an electron as a function of the opening angle and the electron momentum (from MC)
q_i^{scatt}	:	expected p.e.s for the i-th PMT from scattered photons

The value of $Q^{exp}(p_e, \theta_i)$ is calculated using Monte Carlo. The light intensity depends on the distance as $(R/l_i)^{1.5}$ where the 1.5 factor was determined using Monte Carlo simulation.

For muons, the expected charge deposited in the i-th PMT is calculated as follows:

$$q_i^{exp}(\mu) = \left(\alpha_\mu \times \frac{\sin^2 \theta_{x_i}}{r_i(\sin \theta_{x_i} + r_i \cdot \frac{d\theta}{dx}\big|_{x=x_i})} + q_i^{knock}\right) \times \frac{1}{\exp(r_i/L)} \times f(\Theta_i) + q_i^{scatt}, \tag{7.5}$$

where

α_μ	:	normalization factor
x	:	track length of the muon
x_i	:	track length of the muon at which Chrenkov photons are emitted toward the i-th PMT
θ	:	Cherenkov opening angle of the muon traveling at x
θ_i	:	Cherenkov opening angle of the muon traveling at x_i
q_i^{knock}	:	expected p.e.s for the i-th PMT from knock-on electrons

The $\sin^2\theta$ factor comes from the fact that the Cherenkov light intensity depends on the Cherenkov angle. The contribution of knock-on electrons is estimated using Monte Carlo simulation.

7.3.2 Estimation of particle type

There are two types of particle type estimators. One estimator relies on the expected charge pattern described in the previous sub-section, while the other relies on the Cherenkov angle. For the pattern estimator, we first construct a likelihood for each ring, as described in the following equation:

$$L_n(e \text{ or } \mu) = \prod_{\theta_i < (1.5\times\theta_c)} \text{prob}\left(q_i^{obs}, q_i^{exp}(e \text{ or } \mu) + \sum_{n' \neq n} q_{i,n'}^{exp}\right), \tag{7.6}$$

where the product is made over the PMTs inside the n-th ring. q_i^{obs} is the observed number of photo-electrons in the i-th PMT, $q_{i,n}^{exp}(e \text{ or } \mu)$ is the expected number of photo-electrons in the i-th PMT from the n-th ring assuming an electron or a muon as in Eq. 7.4 or Eq. 7.5, and $q_{i,n}^{exp}$ is the expected number of photo-electrons from the n'-th ring without any assumption of particle types. The function *prob* is the probability to detect q_i^{obs} in the i-th PMT when q_i^{exp} is expected.

To combine this pattern estimator with the angle estimator, we convert it into a χ^2 parameter:

$$\chi_n^2(e \text{ or } \mu) = -2\log L_n(e \text{ or } \mu) + \text{constant}. \tag{7.7}$$

Once we have the χ^2 parameter, we compute a probability as done in the following equation:

$$P_n^{pattern}(e \text{ or } \mu) = \exp\left(-\frac{(\chi^2(e \text{ or } \mu) - \min\,[\chi_n^2(e), \chi_n^2(\mu)])^2}{2\sigma^2_{\chi_n^2}}\right), \tag{7.8}$$

where $\sigma^2_{\chi_n^2}$ is the resolution of the χ^2 distribution and is equal to $\sigma^2_{\chi_n^2} = \sqrt{2N}$ and N is the number of PMTs used in the calculation.

To use the Cherenkov angle estimator we compute the following probability:

$$P_n^{angle}(e \text{ or } \mu) = \exp\left(-\frac{\left(\theta_n^{obs} - \theta_n^{exp}(e \text{ or } \mu)\right)^2}{2(\delta\theta_n)^2}\right), \tag{7.9}$$

where θ_n^{obs} is the reconstructed opening angle of the n-th ring, $\delta\theta_n$ its error and θ_n^{exp} is the expected opening angle of the n-th ring assuming the particle is either a electron or a muon.

Once both probabilities are computed we can build the final PID probability. For single ring events we use both the pattern and the angle probability while for multi-ring events we use only the pattern probability. Therefore for single-ring events we have $P_1((e \text{ or } \mu) = P_1^{pattern}(e \text{ or } \mu) \times P_1^{angle}(e \text{ or } \mu)$ and for multi-ring events we have $P_n((e \text{ or } \mu) = P_n^{pattern}(e \text{ or } \mu)$.

Finally we construct the PID estimator using the following equation:

$$P = \sqrt{-\log P_n(\mu)} - \sqrt{-\log P_n(e)}. \tag{7.10}$$

The PID estimator is shown in Fig. B.7 for SK1 and Fig. B.8 for SK2. The systematic uncertainties on the PID estimator are 1% for the single-ring events and 10% for the multi-ring events, for both SK1 and SK2.

7.4 Precise vertex fitting

For single-ring events, the vertex calculated by TDC-fit in Section 7.1 is not as good in the direction in which the particle is traveling as it is in the perpendicular plan to that direction. This is because if the vertex is slightly moved along the longitudinal direction the time of flight calculated for each hit PMT will be moved by the same amount, and therefore the goodness of fit does not change by much. In order to solve this problem, we apply a different fitter called MS-fit (`msfit`) (muon shower fit). MS-fit is based on a likelihood comparing the observed charge distribution and a expected charge distribution, similar to what is done in the PID algorithm. Using the same likelihood function as in Eq. 7.6 we modify slightly the vertex and the ring direction, maximize the goodness of TDC-fit, and iterate until the vertex moves by less than 5cm and the ring direction by less than 0.5°.

The vertex resolution and angular resolution for different sub-samples and for SK1 and SK2 are shown in Table 7.1 and in Fig. 7.6, Fig. 7.7, Fig. 7.8, and Fig. 7.9. The resolution is defined as the width at which 68% of events are included.

	SK1		SK2	
	e-like	μ-like	e-like	μ-like
Vertex resolution				
Sub-GeV single ring	27 cm	26 cm	32 cm	31 cm
Multi-GeV single ring	49 cm	24 cm	47 cm	27 cm
Multi rings	-	57 cm	-	77 cm
PC events	56 cm		63 cm	
Angular resolution				
Sub-GeV	3.1°	2.0°	3.3°	2.2°
Multi-GeV	1.5°	0.9°	1.5°	1.0°

Table 7.1: Vertex resolution and angular resolution for SK1 and SK2.

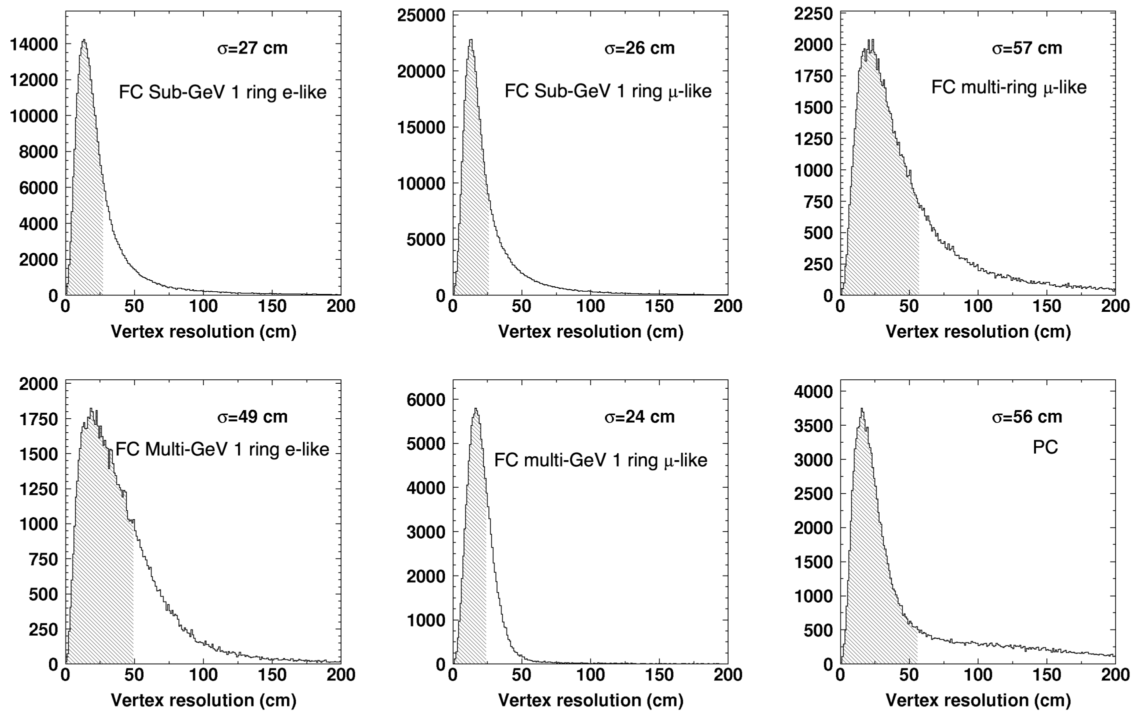

Figure 7.6: Distance between the true and reconstructed vertex for SK1. Top row: FC Sub-GeV 1ring e-like, FC Sub-GeV 1ring μ-like, FC multi-ring μ-like. Bottom row: FC Multi-GeV 1-ring e-like, FC Multi-GeV 1ring μ-like, PC

7.5 Momentum determination (`spfinalsep`)

The momentum calculation of each ring is based on the observed number of photoelectrons inside a cone of 70° opening angle around the ring (variable R_{TOT}). When two rings intersect, we have to properly assign the number of p.e's that belong to each ring. To do so, we use the expected charge contribution from each ring (sum on index n') in the i-th PMT and we compute the fractional charge observed from the n-th ring in the i-th PMT:

$$q_{i,n}^{obs} = q_i^{obs} \times \frac{q_{i,n}^{exp}}{\sum_{n'} q_{i,n'}^{exp}}. \tag{7.11}$$

We compute the variable R_{TOT} for each ring based on the number of observed p.e's in the cone of 70° opening angle and in a time window that goes from -50 ns to 250 ns

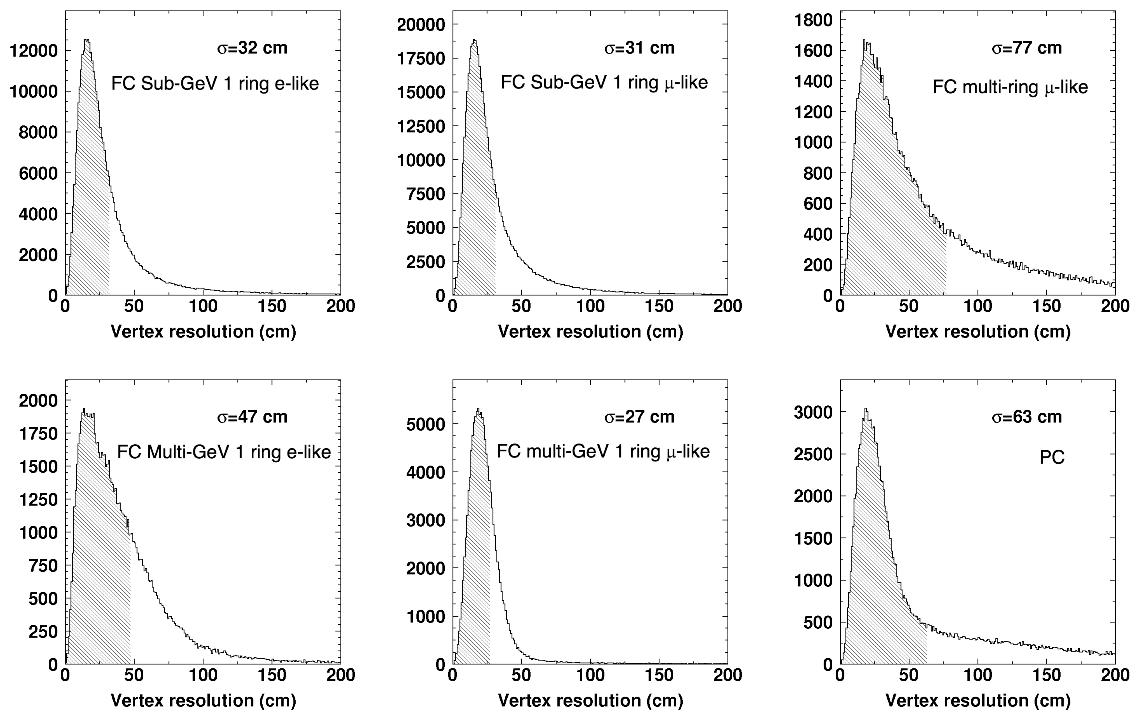

Figure 7.7: Distance between the true and reconstructed vertex for SK2. Top row: FC Sub-GeV 1ring e-like, FC Sub-GeV 1ring μ-like, FC multi-ring μ-like. Bottom row: FC Multi-GeV 1-ring e-like, FC Multi-GeV 1ring μ-like, PC

around the peak of the "TOF-subtracted" hit timing distribution. We also correct for the water attenuation length and the acceptance of the PMT. In order to convert R_{TOT} into the momentum of each ring, we need to know the absolute energy scale. To do so, we use several calibration methods as described in Section 4.5. The resolution of the momentum is presented in Fig. 7.10.

7.6 Ring number correction (`aprngcorr`)

After the momentum reconstruction is done, we apply a correction to the number of rings found by the ring counting algorithm. This is applied at this stage because mis-fitted rings often have a low momentum and overlap with other more energetic rings. Two sets of cuts are applied at this stage. If one of the two sets of cuts is satisfied, then

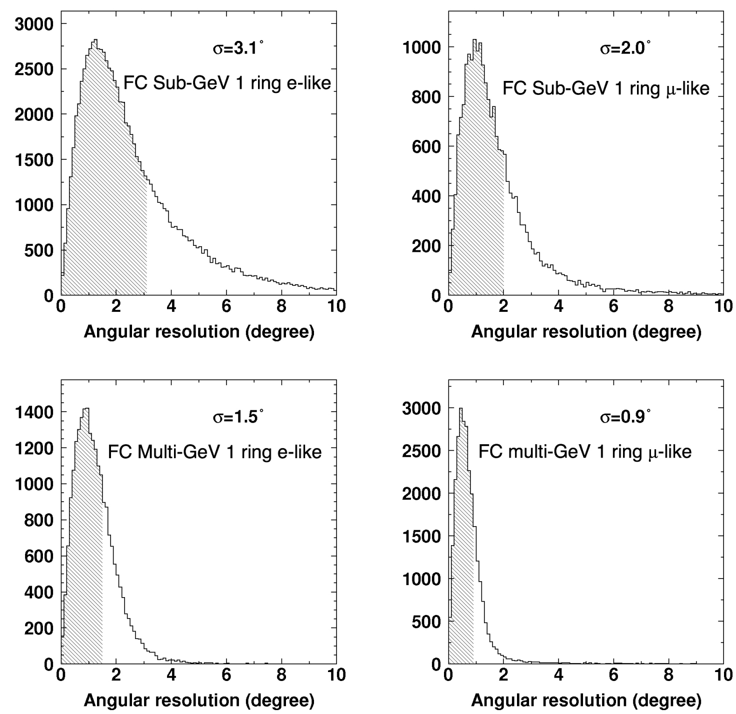

Figure 7.8: Angle between true and reconstructed direction of the outgoing lepton for CC quasi-elastic events for SK1. Top: FC Sub-GeV 1ring e-like, FC Sub-GeV 1ring μ-like. Bottom: Multi-GeV 1-ring e-like, FC Multi-GeV 1ring μ-like.

the ring i is removed. We require either the following set of three cuts,

1. $E_i < E_j$ The visible energy of ring i is smaller than the visible energy of ring j

2. $\theta_{ij} < 30°$ The angle between the direction of ring i and ring j is less than 30 degrees.

3. $E_i \times \cos\theta_{ij} < 60\ MeV$

or we require the following two cuts.

1. $\frac{E_i}{\sum_n E_n} < 0.05$

2. $E_i < 40\ MeV$

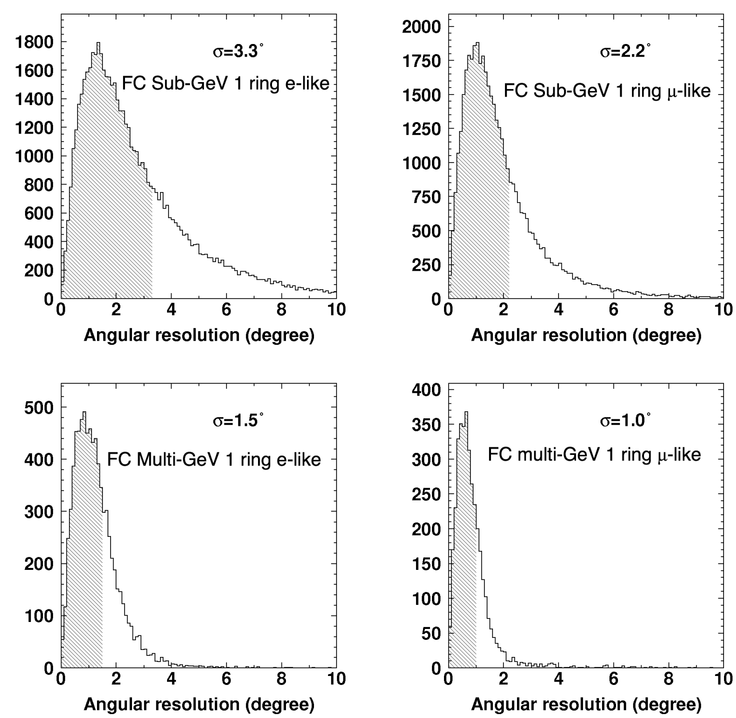

Figure 7.9: Angle between true and reconstructed direction of the outgoing lepton for CC quasi-elastic events for SK2. Top: FC Sub-GeV 1ring e-like, FC Sub-GeV 1ring μ-like. Bottom: Multi-GeV 1-ring e-like, FC Multi-GeV 1ring μ-like.

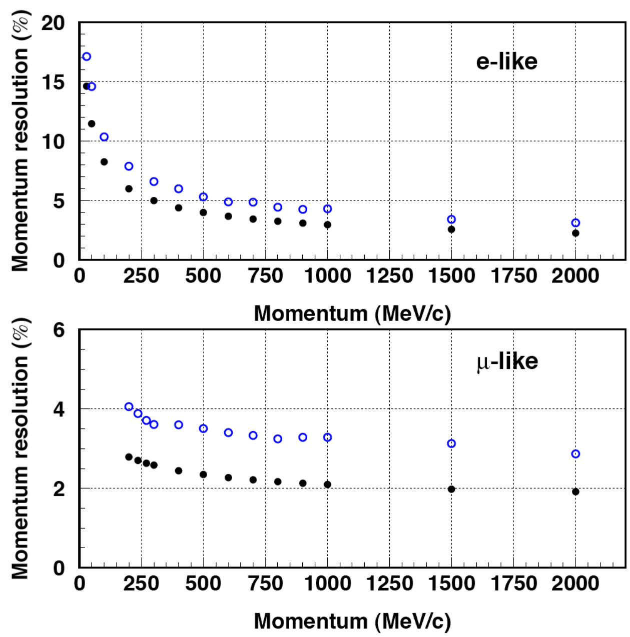

Figure 7.10: Momentum resolution for electron (top) and muon (bottom) for SK1 (filled circles) and SK2 (open circles).

Chapter 8

Dataset

In this chapter I will describe in details the dataset used for the L/E analysis presented in Chapter 9. The samples of neutrino events used in the L/E analysis are the following: the fully-contained events sample and the partially-contained events sample for both SK1 (1489 days of data) and SK2 (804 days). We classify events further into FC events with single-ring or multi-ring and PC events which are stopping or through-going. In all samples, we select only μ-like events.

The main challenge of the L/E analysis is to select a sample of neutrino events with a good enough resolution in flight length L and energy E so that the oscillation pattern of $\nu_\mu \rightarrow \nu_\tau$ as a function of L/E is not washed out. In order to do so, we reconstruct L and E in a different way than in the "zenith angle" analysis, and we apply a cut on the L/E resolution.

For quasi-elastic charged current interaction $\nu + n \rightarrow p + e^-$, our accuracy on the reconstruction of the energy and the flight length of the neutrino is limited by the fact that in most cases we do not see the recoiling proton coming from a neutrino interaction. If we were able to see the recoiling proton, our reconstruction of the energy and flight length would be more accurate. In some cases, the recoil proton is above Cherenkov threshold and if it is properly identified, we can collect a sample of events for which all the kinematics variables are known. In that case, the energy and the flight length of the incoming neutrino can be fully reconstructed. This idea was explored and is fully described in Appendix D. Adding this sample did not improve the sensitivity of the L/E analysis, and it was therefore not added.

8.1 Events samples

After data reduction, a few more cuts are applied to select FC and PC events which are suitable for the L/E analysis.

8.1.1 FC single-ring and multi-ring

For both fully-contained sample we apply the following three cuts:

- Inside the fiducial volume. Distance between the reconstructed vertex and the endcap of the detector is greater than 1.5 m and the distance between the vertex and the barrel is greater than 1.0 m.
- No more than 10 (16) hits in the outer detector for SK1 (SK2).
- Visible energy greater than 30 MeV.

The fiducial volume used for the fully-contained samples in the L/E analysis is larger than for other analyses and larger than for the PC samples. This is done to increase the statistics. The vertex distributions for data and Monte Carlo are shown in Fig. B.1 and Fig. B.3.

To select FC single-ring events we apply two additional cuts.

- Number of rings equals 1.
- The ring should identified as μ-like and its momentum should be greater then 200 MeV/c ($p_\mu > 200$ MeV/c).

To select FC multi-ring events, we apply the same three common FC cuts, and then apply two more cuts:

- Number of rings must be greater than 1.
- The most energetic ring must be μ-like and its momentum must be greater than 600 MeV/c. The visible energy E_{vis} should also be greater than 600 MeV.

8.1.2 PC stopping and through-going

PC stopping events contain muons that stop in the outer detector. The energy of such muons can be accurately reconstructed since we know the length of the muon, and therefore we know its energy from calculation of the energy loss via dE/dx. PC through-going events on the other hand contain muons which exited the outer detector before stopping, and therefore the energy reconstructed for such events is only a lower limit on the energy of the incoming muon.

To separate PC stopping from PC through-going events we look at the maximum number of OD photoelectrons in a 500 ns time window between -400 ns and +500 ns (PE_{anti}) and for stopping events we require that PE_{anti} be less than 1.5 times the expected number of photoelectrons from the track length information (PE_{exp}). Figure 8.1 shows the separation criteria between PC OD stopping and PC OD through-going for SK1 and SK2. We estimate the systematic uncertainty on the separation between PC OD stopping and PC OD through-going by comparing the data and the Monte Carlo; we do this separately for the top, barrel and bottom of the detector. The agreement between data and MC for SK2 is not as good as for SK1 and this is taken into account in the systematic uncertainties. The systematic uncertainties are therefore different for SK1 and SK2, the SK1 value is 15%, 11.3%, 7.5% for top, bottom and barrel respectively, while the SK2 value is 19%, 18%, 14%, for top bottom and barrel. We decided to use different systematic uncertainties for top, barrel and bottom because the response of the outer detector is different for these three regions, because of the different geometry between the barrel and the endcaps and because of the different PMT types between the top and the bottom.

In summary, we apply three common cuts to select the PC samples:

- Inside the fiducial volume. The distance from the vertex to the wall must be greater than 2 m.
- More than 10 (16) hits in the outer detector for SK1 (SK2).
- Visible energy greater than 350 MeV.

Then to select the stopping sample, we apply two additional cuts:

- Have a total number of photoelectrons in the ID greater than 3000 (1500) for SK1 (SK2).
- The most energetic or the second most energetic ring must be μ-like.
- $PE_{anti} < PE_{exp}/1.5$.

To select the PC through-going sample, we apply the same three general cuts and also two additional cuts. We do not need to apply a μ-like cut to the PC through-going sample since already 99% of CC interactions which produce PC through-going events are $\nu_\mu + \overline{\nu_\mu}$ CC interactions. The two additional cuts are:

- Total number of photoelectrons in the ID greater than 3000 (1500) for SK1 (SK2).
- $PE_{anti} \geq PE_{exp}/1.5$.

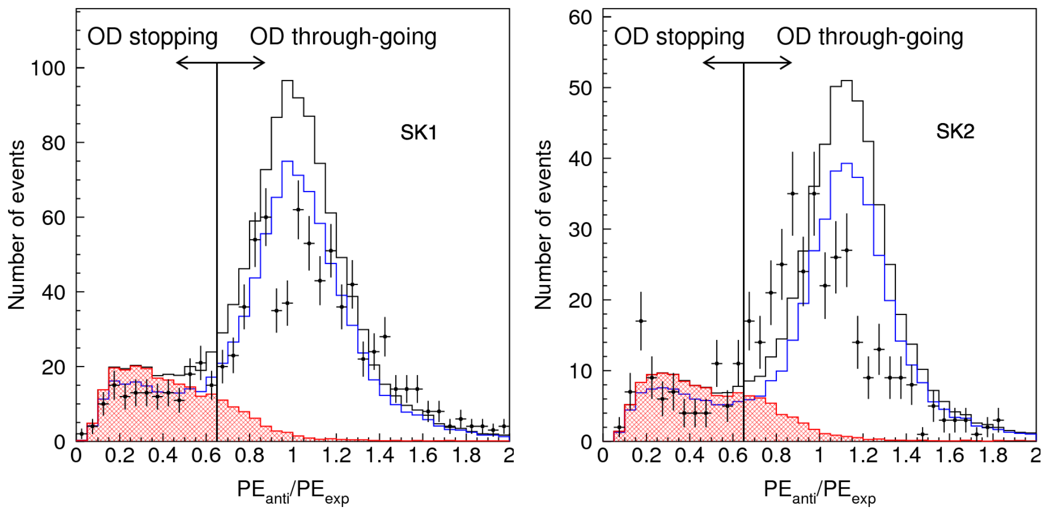

Figure 8.1: Separation criteria between PC OD stopping and PC OD through-going events for SK1 (left) and SK2 (right). The black dots are the data, the black solid line is the unoscillated Monte Carlo, the blue solid line is the oscillated Monte Carlo, and the red hatched histograms are the true stopping events.

8.2 Reconstructing L and E

Reconstructing the energy E and the flight length L as accurately as possible is crucial for the L/E analysis in order to be able to see the oscillatory pattern. If the resolution is not good enough, the oscillation averages out.

8.2.1 Energy

To reconstruct the neutrino energy we compute the *effective* energy (`EVIS2`) of all the outgoing charged particle by looking at the energy of their Cherenkov rings in the inner detector. For PC events, we have to apply a special treatement to estimate the energy of the muon that was deposited after it exited the inner detector.

Fully-contained single-ring

For single-ring fully contained events, the energy of the charged particles is simply the reconstructed energy of the outgoing muon `EVIS2`$= E_\mu$.

Fully-contained multi-ring

For fully-contained multi-ring events, we assume that the most energetic ring comes from a muon emitted through a CC interaction while the other rings are either assumed to be electro-magnetic showers if they are e-like or pions if they are μ-like. Therefore, the reconstructed energy of the charged particles is `EVIS2`$= E_\mu + \sum_{i=2}^{n}(E_e^i \text{ or } E_\pi^i)$.

The reconstruction of μ-like rings assumes that the particle is a muon and therefore the mass of the muon is involved in the energy reconstruction through the Cherenkov energy threshold. If we believe that the particle which emitted the μ-like ring was not a muon but some other massive particle we have to correct for this fact. We can rewrite the energy of a muon as $E_\mu = (E_\mu - E_\mu^{th}) + E_\mu^{th}$ and the energy of a pion as $E_\pi = (E_\pi - E_\pi^{th}) + E_\pi^{th}$, where $E_\mu^{th} = 160$ MeV and $E_\pi^{th} = 212$ MeV are the Cherenkov energy threshold for a muon and a pion. If we assume that dE/dx in water is independent from the energy and the particle type, then the number of emitted Cherenkov photons is just proportional to the track length. So the energy deposited from a muon and a pion which have been estimated from the same ring satisfy the following relation: $E_\mu - E_\mu^{th} = E_\pi - E_\pi^{th}$. And therefore: $E_\pi = E_\mu - E_\mu^{th} + E_\pi^{th} = E_\mu + (E_\pi^{th} - E_\mu^{th})$. So in the case of pions we have to correct the observed energy as follows: $E_\pi = E_\mu + 52$ MeV.

Partially-contained

For the PC sample, we have to take into account the energy deposited in the dead layer that separates the inner and outer detectors, and the energy deposited in the outer detector itself. The energy of the outgoing charged particles is therefore `EVIS2`$=$ $E_{inner} + E_{dead} + E_{outer}$.

E_{inner} is reconstructed in the same way as for fully-contained single or multi-ring events, but we have to apply a correction on the number of rings. Because PC events are quite energetic (≈ 10 GeV), most of the produced rings will be collinear and are likely

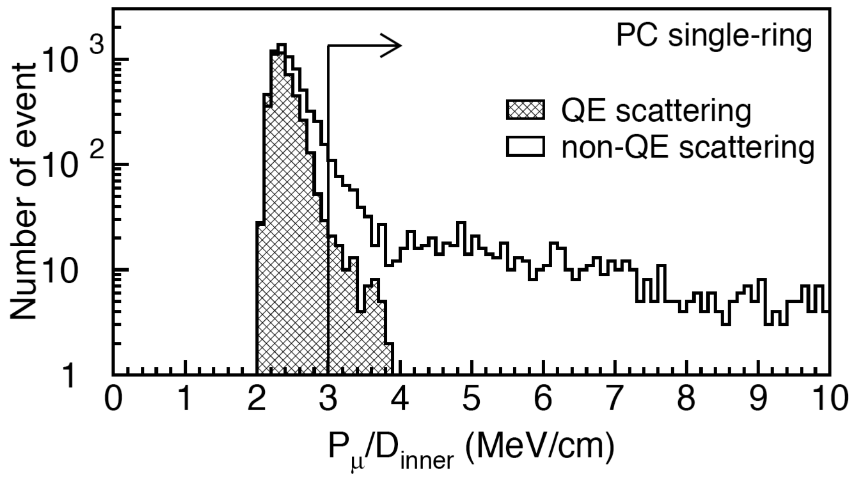

Figure 8.2: P_μ/D_{inner} for quasi-elastic (QE) interactions (hatched) and non-QE interactions in the atmospheric neutrino MC PC single-ring sample. Events at the right of the arrow are divided into two rings: a muon ring and an electron ring.

to overlap. We can recognize mis-reconstructed rings by comparing the momentum of the ring (P_μ) and its track length in the inner detector (D_{inner}) for the PC single-ring sample as in Fig. 8.2. Quasi-elastic events are by definition single-ring events if the proton is below Cherenkov threshold, while non quasi-elastic are likely to be multi-ring. The large tail of non quasi-elastic events in Fig. 8.2, is due to overlapping pions and/or other particles. We therefore apply a correction to the number of rings by using the following method. If the most energetic muon ring satisfies $P_\mu/D_{inner} > 3.0$ MeV/cm, the ring is separated into a muon ring with momentum estimated from the track length in the ID as $D_{inner} \times dE/dx$, where $dE/dx = 2.4$ MeV/cm and an electron ring. The expected charge from the muon is subtracted from the ring and the remaining charge is used the reconstruct the momentum of the electron.

E_{dead} is the energy deposited in the dead region that separate the inner detector from the outer detector. We estimate the energy deposited in this region by measuring the distance the muon traveled in the dead region and assuming a dE/dX of 2.4 MeV/cm.

E_{outer} is the energy deposited in the outer detector. The estimation of E_{outer} is done in the same way as E_{dead} and the flight length in the OD is computed using the energy of the muon and our Monte Carlo.

Reconstruction of the neutrino energy

Finally, once we have reconstructed `EVIS2`, we can infer the neutrino energy by doing a polynomial extrapolation. The parameters a, b, c, d of the polynomial fit are computed using our Monte Carlo.

$$E_{\nu}^{rec} = E_{vis2} \times (a + bx + cx^2 + dx^3) \tag{8.1}$$

with $x = log_{10}(E_{vis2})$

The distributions of $(E_{\nu}^{true} - E_{\nu}^{rec})/E_{\nu}^{true}$ for each sample is presented in Fig. 8.3 for SK1 and Fig. 8.4 for SK2. It is also summarized as a function of energy in Fig. 8.5.

8.2.2 Flight Length

The reconstruction of the flight length uses the reconstructed neutrino energy described in the previous section, the reconstructed zenith angle and it takes into account the fact that we do not know precisely where in the atmosphere the neutrino is created.

Fully-contained single-ring

For single-ring events, the direction of the neutrino is assumed to be the same as the direction of the outgoing muon.

Fully-contained multi-ring

For multi-ring events, we assume that the most energetic ring is a muon and that the other rings are either pions or electro-magnetic showers (from photons or electrons) as described in the energy reconstruction section. The zenith angle of the incoming neutrino

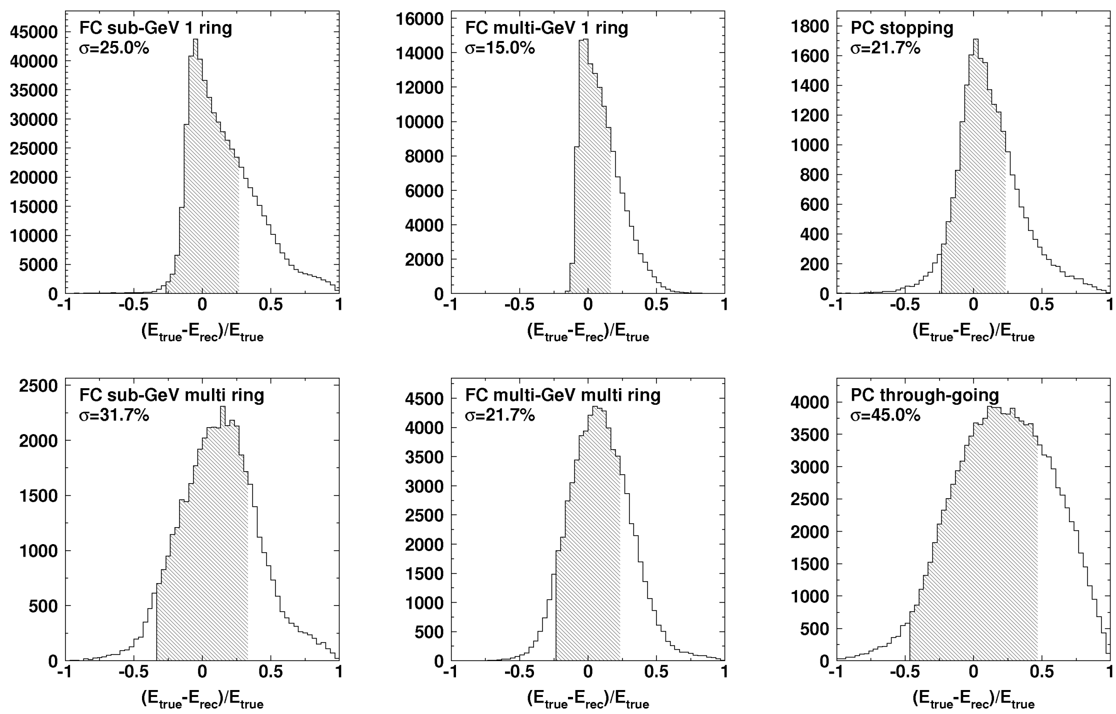

Figure 8.3: $(E_\nu^{true} - E_\nu^{rec})/E_\nu^{true}$ distributions for μ-like SK1 events. Top left: FC Sub-GeV 1 ring. Bottom left: FC Sub-GeV multi-ring. Top middle: FC Multi-GeV 1 ring. Bottom middle FC Multi-GeV multi-ring. Top right: PC stopping. Bottom right PC trough-going. The region histograms represents 68% of the events. Note: the resolution cut has not yet been applied.

is simply equal to the weighted sum of all the reconstructed rings: $\cos\theta_\nu = \cos\theta_{sum}$, with $\vec{d}_{sum} = p_\mu \cdot \vec{d}_1 + \sum_{i=2}^{n}(p_e^i \text{ or } p_\pi^i) \cdot \vec{d}_i$.

Partially-contained sample

The zenith angle of PC events is computed in a very similar way as for FC events. For single-ring events, we have $\cos\theta_\nu = \cos\theta_\mu$. And for multi-ring events we use $\cos\theta_\nu = \cos\theta_{sum}$, with $\vec{d}_{sum} = \alpha \cdot p_\mu \cdot \vec{d}_1 + \sum_{i=2}^{n}(p_e^i \text{ or } p_\pi^i) \cdot \vec{d}_i$. The numerical factor α is set to 2.0 for stopping events and 4.0 for through-going events. This factor has been introduced for better performance.

The angular resolution for each sample is presented in Fig. 8.6 for SK1 and Fig. 8.7

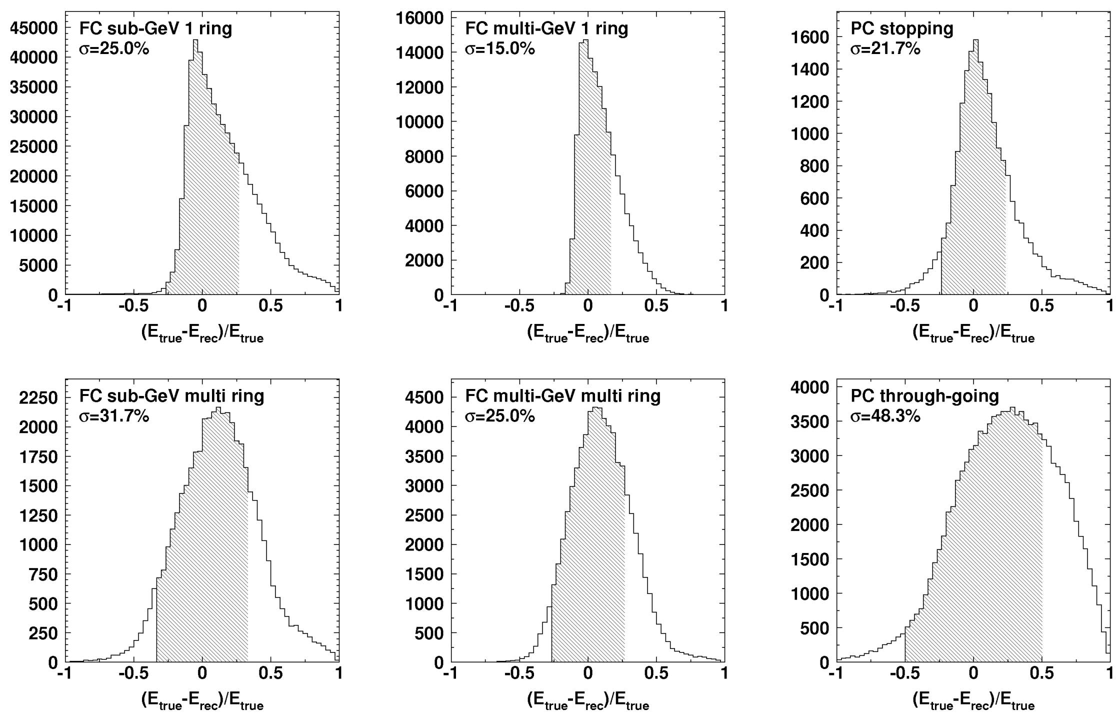

Figure 8.4: $(E_\nu^{true} - E_\nu^{rec})/E_\nu^{true}$ distributions for μ-like SK2 events. Top left: FC Sub-GeV 1 ring. Bottom left: FC Sub-GeV multi-ring. Top middle: FC Multi-GeV 1 ring. Bottom middle FC Multi-GeV multi-ring. Top right: PC stopping. Bottom right PC trough-going. The region histograms represents 68% of the events. Note: the resolution cut has not yet been applied.

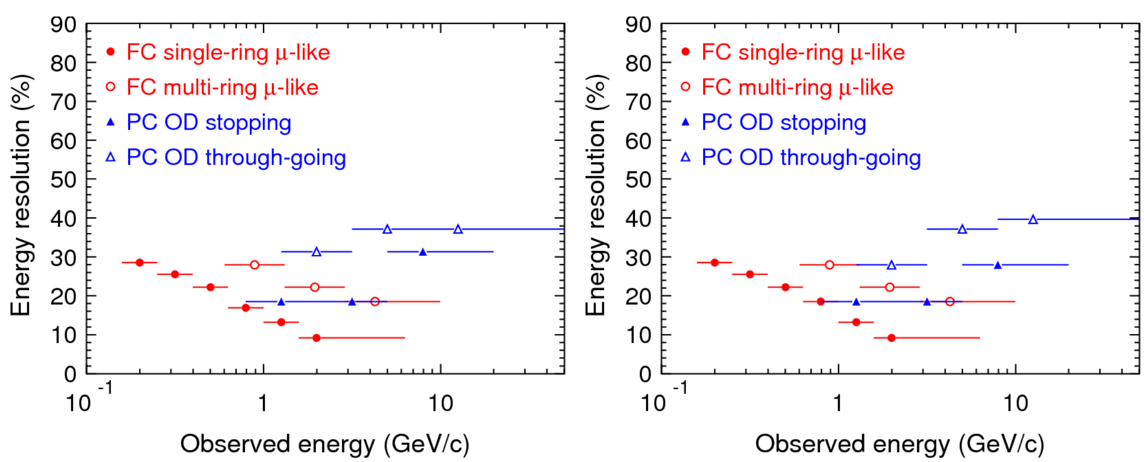

Figure 8.5: Energy resolution for SK1 (left) and SK2 (right).

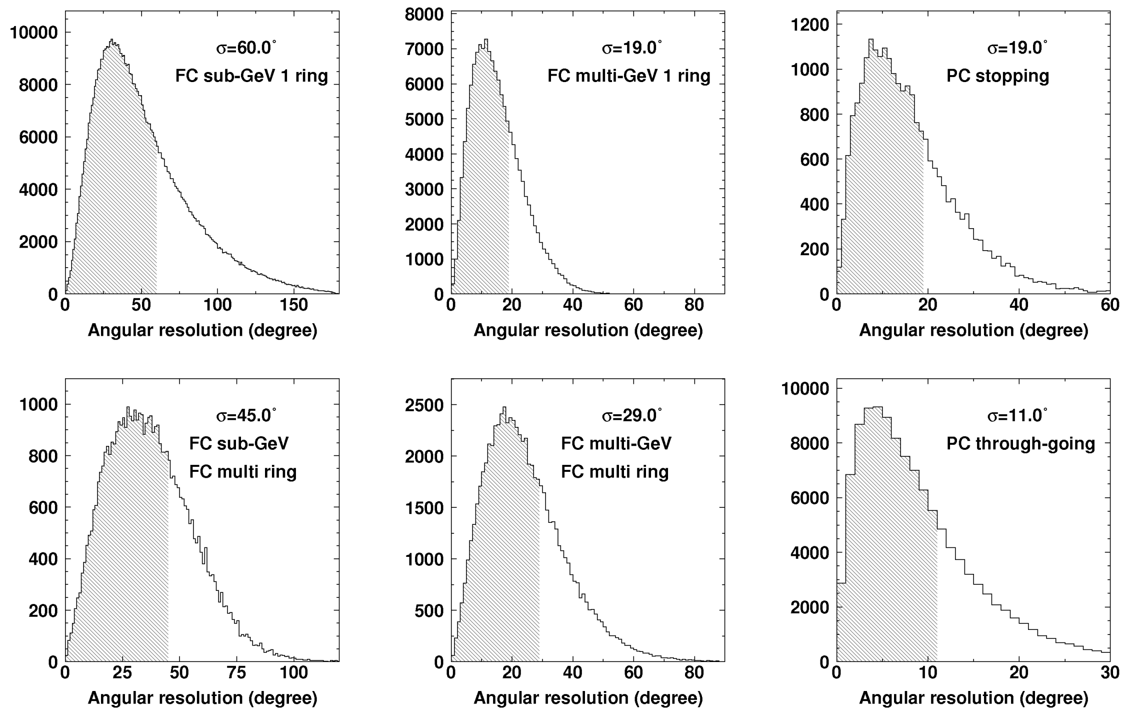

Figure 8.6: Angle between true and reconstructed neutrino direction for μ-like SK1 events. Top left: FC Sub-GeV 1 ring. Bottom left: FC Sub-GeV multi-ring. Top middle: FC Multi-GeV 1 ring. Bottom middle FC Multi-GeV multi-ring. Top right: PC stopping. Bottom right PC trough-going. The hatched region represents 68% of the events. Note: The resolution cut has not yet been applied.

for SK2. It is presented as a function of energy in Fig. 8.8.

Reconstruction of the neutrino flight length

Finally after the reconstruction of the neutrino zenith angle has been completed, we estimate its flight length. The relation between zenith angle and flight length can be seen in Fig. 8.9. For horizontal events ($\cos\theta = 0$) a small variation in the zenith angle represents a large variation in the flight length, therefore it is very hard to obtain a good resolution on the flight length for horizontal events. For upward going events, the uncertainty in the production height is of the order of a percent at most since the overall flight length is large (≈ 10000 km) while the atmosphere is only about 15 km thick, but

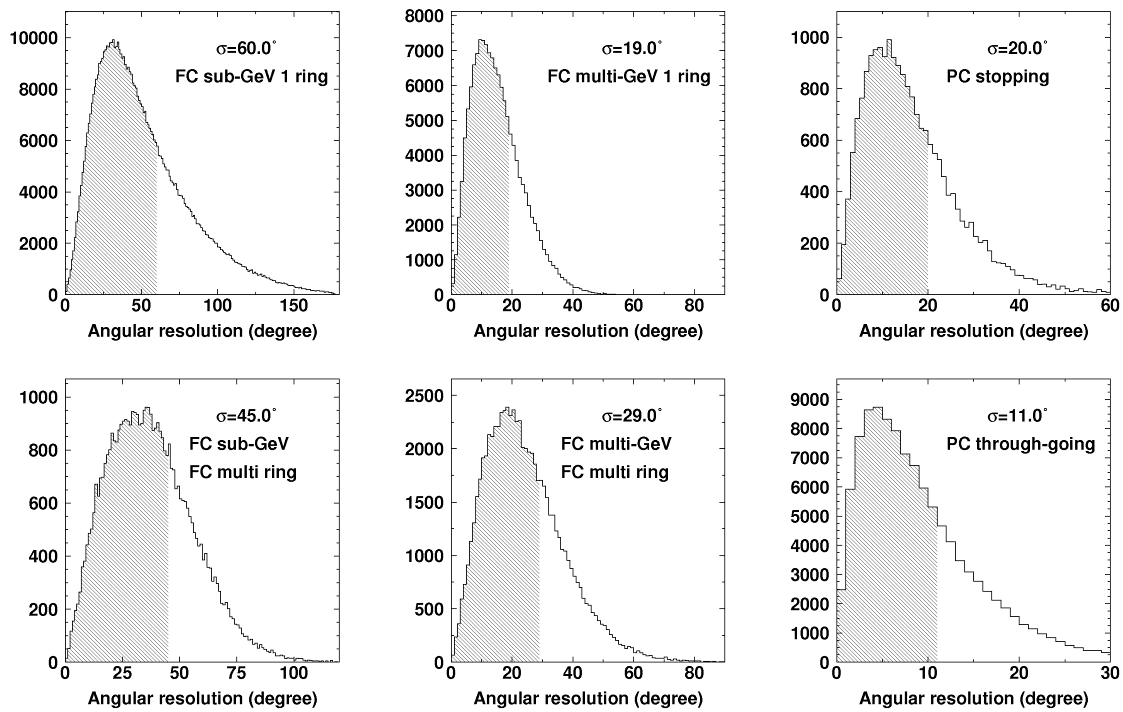

Figure 8.7: Angle between true and reconstructed neutrino direction for μ-like SK2 events. Top left: FC Sub-GeV 1 ring. Bottom left: FC Sub-GeV multi-ring. Top middle: FC Multi-GeV 1 ring. Bottom middle FC Multi-GeV multi-ring. Top right: PC stopping. Bottom right PC trough-going. The region histograms represents 68% of the events. Note: the resolution cut has not yet been applied.

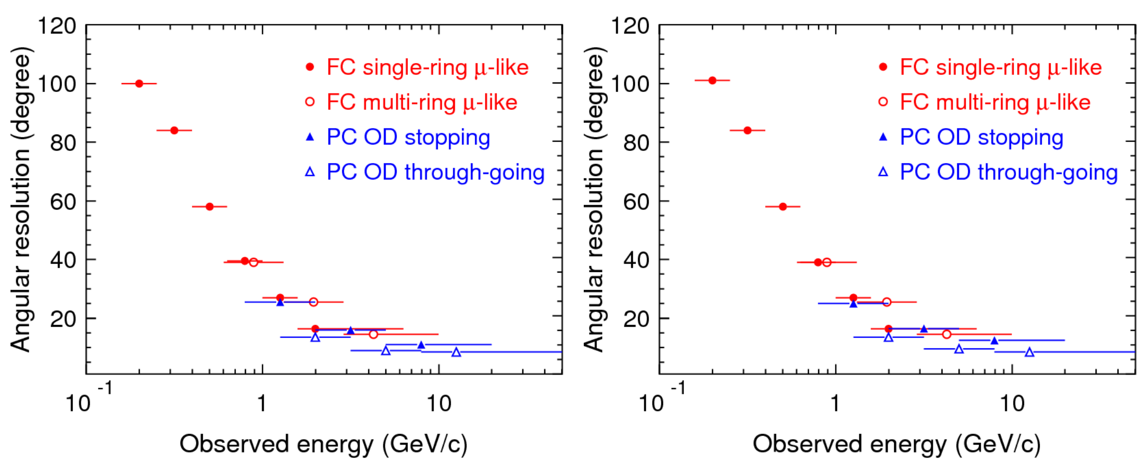

Figure 8.8: Angular resolution for SK1 (left) and SK2 (right).

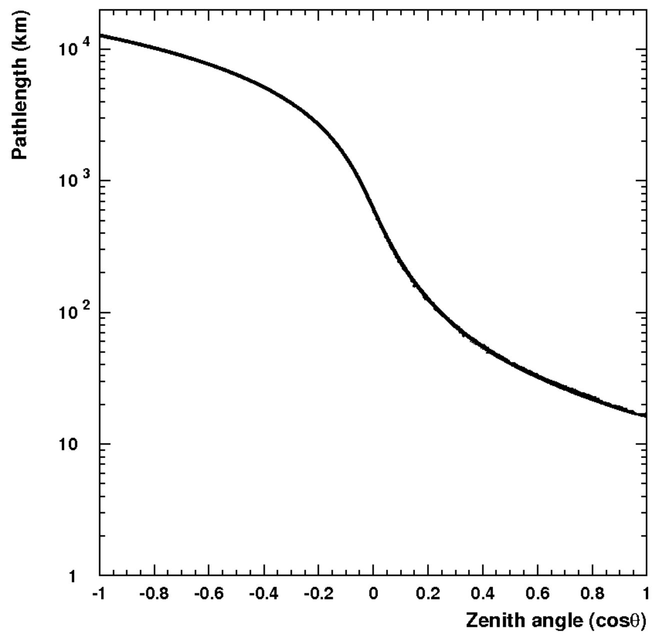

Figure 8.9: True flight length versus true zenith angle for fully-contained single-ring events with an E_{vis} between 0.9 and 1.1 GeV (SK1 Monte Carlo).

for downward and horizontal going events the uncertainty is much larger, and this is taken into account in the systematic erros.. We estimate the neutrino flight length by using the reconstructed zenith angle, the neutrino energy, and assuming ν_μ interactions.

8.3 Resolution cut

In order to perform the L/E analysis, we have to select a set of events that have a good resolution in L/E. To do so, we use Monte Carlo to predict the L/E resolution of each sample (FC-1R, FC-MR, PC-stop and PC-through) at each point of a $(\cos\theta_\nu^{rec}, E_\nu^{rec})$ grid. Later, we keep only events that are expected to have a good resolution.

In order to to estimate the resolution as accurately as possible, we take into account the fact that the L_ν/L_ν^{rec} and E_ν/E_ν^{rec} have asymmetric distributions and that the peak of the $(L_\nu/E_\nu)/(L_\nu^{rec}/E_\nu^{rec})$ distribution is not equal to one. Since this smears the resolution, by correcting for this known fact, we can improve the resolution of each sample. To do so we shift the L/E value as follow: $(L_\nu^{rec}/E_\nu^{rec})' = \delta(L/E) \times (L_\nu^{rec}/E_\nu^{rec})$ where $\delta(L/E)$ is computed for each sample using Monte Carlo and for each point on the $(\cos\theta_\nu^{rec}, E_\nu^{rec})$ grid. Once this is done, we can draw a resolution map and this is shown in Fig. 8.10. We decided to use the 70% cut as this was found to maximize the log likelihood [47].

The effect of the resolution is to remove events coming from the horizontal direction as for these events a small variation in θ corresponds to a large variation in flight length. Very high energy events ($E_{vis2} > 10$ GeV for FC single-ring and $E_{vis2} > 50$ GeV for FC multi-ring and PC events) are also removed as we do not have enough statistics to estimate their resolution. The $log_{10}((L_\nu/E_\nu)/((L_\nu^{rec}/E_\nu^{rec}))$ distributions are shown in Fig. 8.11. The effect of the resolution cut can be seen in Fig. 8.12.

8.4 Event summary

The dataset obtained after the resolution cut is applied, is presented in Table 8.1. The energy of the events range from 30 MeV to about 20 GeV, the flight length ranges from a few kilometers to about 10000 km. Close to the horizontal, the flight length changes fast as a function of the zenith angle, therefore L/E bins which consists mainly of events coming from an horizontal direction have much less statistics that others. Furthermore, the flight length resolution is usually worse for horizontal events, and this decreases even further the statistics of these bins. As a consequence, the distribution of the number of events as a function of L/E has the “two-bumps” structure that can be seen in Fig. 8.13. Using $\Delta m_{23}^2 = 2.2 \times 10^{-3}\ eV^2$, the first oscillation minimum is located where $L/E = \frac{\pi}{2}/(1.27 \times \Delta m^2) = 562\ km/GeV$. At this value of L/E, most of the events come from the PC through-going sample. Therefore, the work done on improving PC reduction and consequently increasing the PC sample statistics, will be

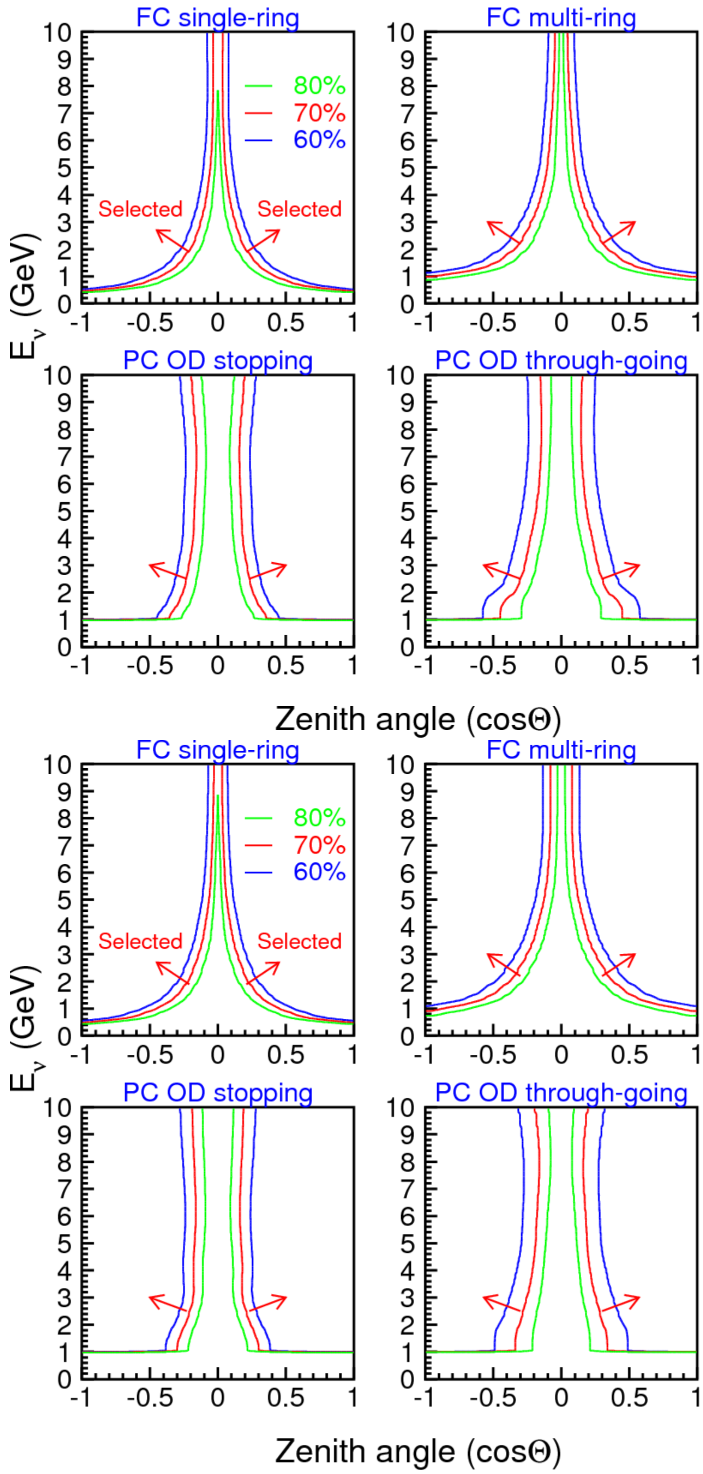

Figure 8.10: Contour plots of 60%, 70% and 80% L/E resolutions for each sample, for SK1 (left) and SK2 (right)

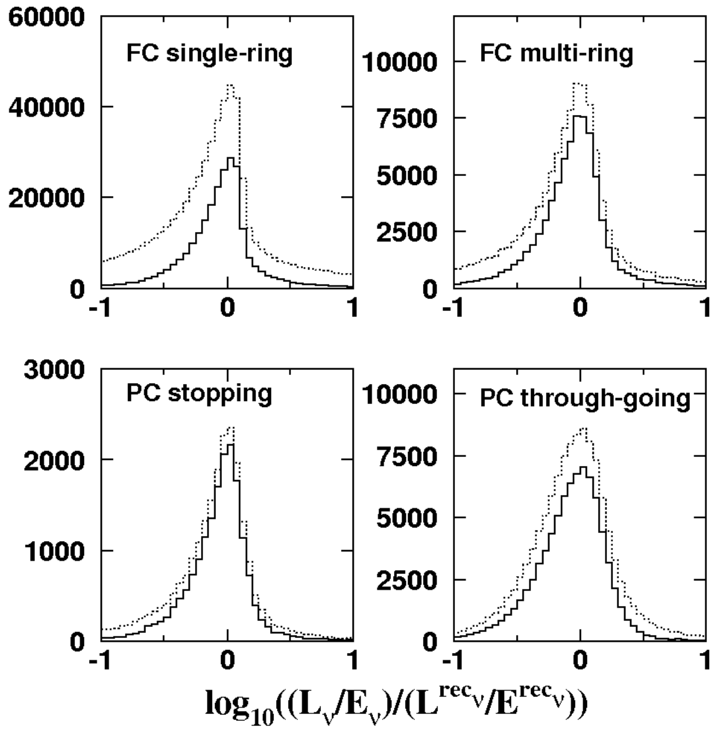

Figure 8.11: $log_{10}((L_\nu/E_\nu)/((L_\nu^{rec}/E_\nu^{rec}))$ distributions for FC single-ring, FC multi-ring, PC OD stopping and PC OD through-going without the resolution cut (dashed lines) and with the resolution cut (solid lines).

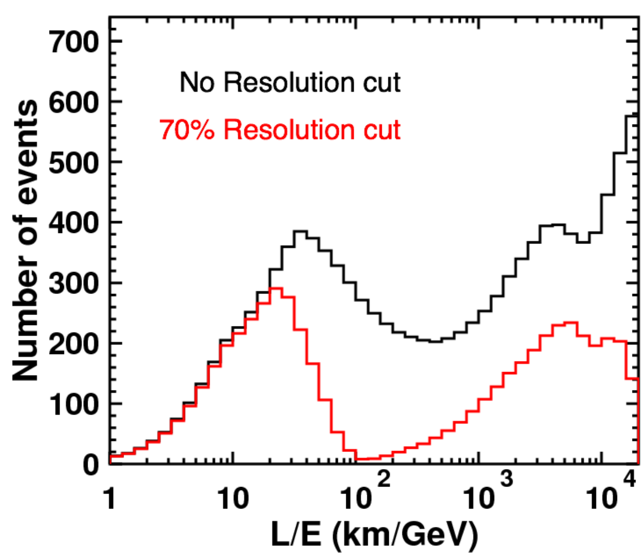

Figure 8.12: Effect of the resolution cut: L/E distribution for normalized oscillated SK1+SK2 Monte Carlo with (red) and without (black) the resolution cut.

especially relevant to the L/E analysis when the SK3 sample will be introduced.

SK1 (1489 days)	Data		MC		$\nu_\mu CC$
Apply resolution cut	yes	no	yes	no	
FC					
Single-ring	1562	[4491]	2093.6	[6018.1]	(98.2%)
Multi-ring	445	[667]	625.6	[972.9]	(93.5%)
PC					
Stopping	100	[134]	148.5	[193.1]	(94.9%)
Through-going	445	[710]	670.6	[952.7]	(99.2%)
SK2 [804 days]	Data		MC		$\nu_\mu CC$
Apply resolution cut	yes	no	yes	no	
FC					
Single-ring	855	[2390]	1170.4	[3306.5]	(98.2%)
Multi-ring	246	[412]	333.4	[516.6]	(93.3%)
PC					
Stopping	73	[98]	68.5	[91.1]	(94.2%)
Through-going	191	[308]	321.7	[484.5]	(99.3%)

Table 8.1: Summary of the event samples for SK1 and SK2 data.

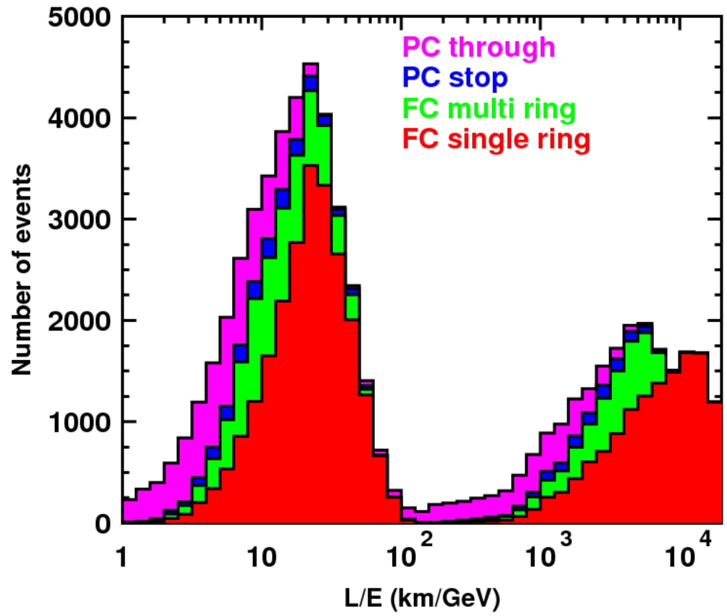

Figure 8.13: Stacked L/E distribution for each sub-sample after the resolution cut is applied and for an unnormalized oscillated set of Monte Carlo.

Chapter 9

L/E analysis

The goal of the L/E analysis is to be able to see the oscillation pattern expected from the standard 2-flavor oscillation equation (Eq. 2.9). A similar analysis was conducted by the Soudan-2 experiment [70]. In an ideal case, this oscillation pattern looks like Fig. 9.1. Because of finite energy and flight length resolution, the oscillatory signature of the survival probability of muon neutrinos is a challenge to see.

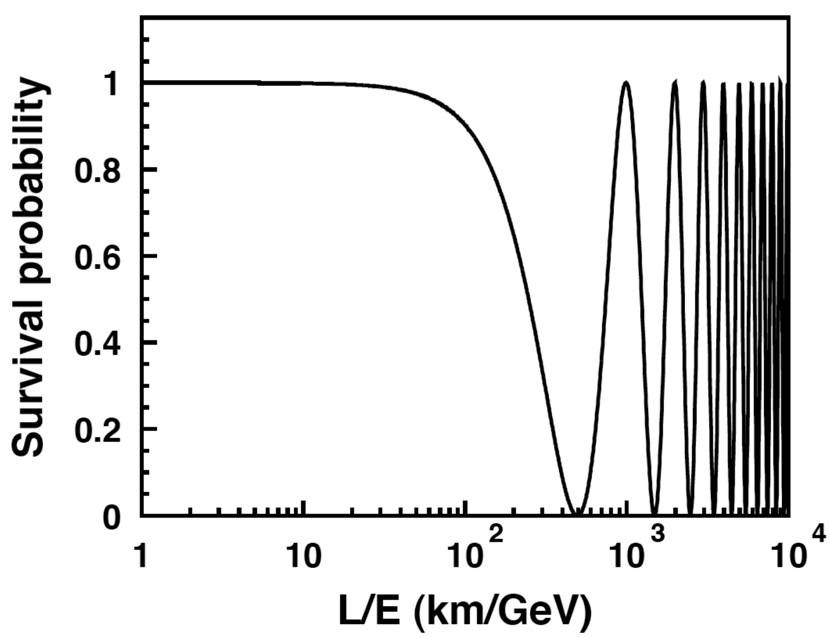

Figure 9.1: Survival probability of $\nu_\mu \rightarrow \nu_\tau$, without any detector effect as a function of L/E.

After selecting events as explained in the previous chapter, we apply a maximum likelihood analysis to determine the best fit oscillation parameters $\sin^2 2\theta_{23}$ and Δm^2_{23}. Other theories, like neutrino decay [71, 72] or neutrino decoherence [73] predict a deficit of upward-going neutrinos, but the sinusoidal pattern of neutrino oscillation is unique. Therefore comparing the L/E spectrum of the data and the L/E spectrum of these different theories is a good way to determine which model describes the neutrino data the best.

9.1 Maximum likelihood analysis and χ^2 fit

The L/E analysis is performed with a binned maximum likelihood analysis. We use 43 L/E bins ranging from $\log_{10}(L/E) = 0.0$ to 4.3. The systematics used for the L/E analysis are described fully later in this chapter and are taken into account in the likelihood using the "pull method" [74]. Because of the small number of events per L/E bins, Poisson statistics is used. With pull term added for systematic errors, the likelihood is defined as follows:

$$L(N_{exp}, N_{obs}) = \prod_i \frac{\exp(-N_i^{exp})(N_i^{exp})^{N_i^{obs}}}{N_i^{obs}!} \times \prod_j \exp\left(\frac{\epsilon^j}{\sigma_j^{sys}}\right). \tag{9.1}$$

We can rewrite the likelihood function as a χ^2:

$$\begin{aligned}
\chi^2 &\equiv -2\ln\left(\frac{L(N^{obs}, N^{exp})}{L(N^{obs}, N^{obs})}\right) \\
&= \sum_{i=1}^{nbin}\left[2(N_i^{exp}(1+\sum_{j=1}^{nsys} f_j^i \cdot \epsilon^j) - N_i^{obs}) - 2N_i^{obs}\ln\left(\frac{N_i^{obs}}{N_i^{exp}(1+\sum_{j=1}^{nsys} f_j^i \cdot \epsilon^j)}\right)\right] \\
&+ \sum_j^{nsys}(\frac{\epsilon^j}{\sigma_j^{sys}})^2,
\end{aligned} \tag{9.2}$$

where N_i^{obs} is the number of observed events in the i-th L/E bin, N_i^{exp} is the expected number of events in the i-th L/E bin from the Monte Carlo simulation and for a given set of oscillation parameters. N_i^{exp} can be corrected to account for systematic uncertainties: σ_j^{sys} is the j-th systematic error and ϵ_j is the pull value on the j-th systematic uncertainty. The f_j^i parameter is the fractional change expected in the i-th bin from the j-th systematic due to a variation of the parameter ϵ_j.

Searching numerically for the best fit parameters in ϵ_k, Δm^2 and $\sin^2 2\theta$ would be very slow. Instead, we minimize Eq. (9.2) as a function of ϵ_k and then, since ϵ_k is small, we can do a linear expansion and obtain a set of linear equations which are much faster to solve:

$$\sum_{i=1}^{nbin} \left[(1 + (f_j^i \cdot \epsilon^j)^2 + ...)N_i^{obs} - N_i^{exp}\right] \cdot f_k^i = \sum_{j=1}^{nsys} \Big(\frac{\delta_{jk}}{(\sigma_j^{sys})^2} + \sum_{i=1}^{nbin} N_i^{obs} f_j^i f_k^i \Big) \epsilon_k. \tag{9.3}$$

where the number of L/E bins is $nbin \equiv 43$ and the number of systematic errors is $nsys \equiv 29$. We then scan the Δm^2 and $\sin^2 2\theta$ parameter space in order to find the set of parameters that finally minimize the reduced χ^2. It is worth noticing that this approach is completely equivalent to doing a unbinned maximum likelihood analysis if we use the Monte Carlo to generate the p.d.f. P needed in the following equation. The proof can be found in Appendix C.

$$\ln L \quad = \quad \left(\sum_{i}^{N^{obs}} \ln(N^{exp} \cdot P(x_i|\alpha)) \right) - N^{exp} \tag{9.4}$$

9.1.1 Combining SK1 and SK2 dataset

When combining datasets corresponding to different versions of the detector (like the SK1 and the SK2 datasets), we have to make sure that the systematic errors are taken into account correctly. Some systematic errors are common to both datasets, like the uncertainties on the neutrino flux, while others are different for each datasets, like the uncertainties directly related to the detector, or the algorithms used in the data analysis. So in order to treat these systematic errors properly, we modify the reduced χ^2 defined earlier as follows:

$$\sum_{i=1}^{nbin*nset} \left(N_i^{obs} - N_i^{exp}\right) f_k^i = \sum_{j=1}^{nsys_{tot}} \left(\frac{\delta_{jk}}{\sigma_j^2} + \sum_{i=1}^{nbin*nset} N_i^{obs} f_j^i f_k^i\right) \epsilon_k, \tag{9.5}$$

with $nset \equiv 2$ since we have two datasets (SK1 and SK2), and the total number of systematic uncertainty being $nsys_{tot} = nsys_{sk1} + nsys_{sk2} + nsys_{common}$, where $nsys_{common} = 13$ and $nsys_{sk1} = nsys_{sk2} = 16$ so $nsys_{tot} = 45$. By doing this, we allow pull terms related to uncertainties that are different between SK1 and SK2 to vary separately while pull terms related to uncertainties that are common between SK1 and SK2 can take only a single value.

To apply this method, we modify the f_{ij} matrix such that the terms corresponding to an SK1-only systematic and an SK2 bin (and vice versa) are set to zero, while terms that are common to SK1 and SK2 are forced to be identical. A schematic view of the changes made to the f_{ij} matrix is presented in Table 9.1. This method can be extended to more datasets such as SK1+SK2+SK3.

f_{ij}	Sys for SK1 only			Sys for SK2 only			Sys common to SK1 and SK2			
SK1 bins	x	x	x	0	0	0	a	b	c	d
	x	x	x	0	0	0	e	f	g	h
	x	x	x	0	0	0	i	j	k	l
	x	x	x	0	0	0	m	n	o	p
SK2 bins	0	0	0	x	x	x	a	b	c	d
	0	0	0	x	x	x	e	f	g	h
	0	0	0	x	x	x	i	j	k	l
	0	0	0	x	x	x	m	n	o	p

Table 9.1: Schematic view of the f_{ij} matrix modified to account for two datasets

9.2 Systematic uncertainties

There are several categories of systematic errors taken into account. Uncertainty in the neutrino simulation model, uncertainty in the neutrino interaction simulation, uncertainty in the event reduction, and uncertainty in the event reconstruction. The systematic uncertainties used in the L/E analysis are a subset of the ones used in the zenith angle analysis. The description of each systematic, its value for SK1 and SK2, its best fit values and its pull values are summarized in Tables 9.2, 9.3 and 9.4.

9.2.1 Simulation uncertainties - Neutrino flux

Normalization (1)

The overall normalization is left free because the overall normalization is irrelevant to the L/E analysis. What is important in the analysis is the shape of the L/E spectrum. The uncertainty on the overall normalization is linked to the atmospheric neutrinos flux and it comes from the uncertainty on the cosmic ray flux and the hadronic interaction used in the model. The normalization is common for SK1 and SK2.

	Systematic Description	common to SK1 and SK2		
		σ %	best fit%	pull
1	Normalization	free	0.14	0.000
	Neutrino flux			
3	Flux $\overline{\nu_\mu}/\nu_\mu$ ratio	6.0	0.49	0.0066
4	Flux up/down		0.06	0.0032
	Single-ring < 400 MeV	0.3		
	Single-ring > 400 MeV	0.5		
	Single-ring multi-GeV	0.2		
	Multi-ring Sub-GeV	0.2		
	Multi-ring Multi-GeV	0.2		
	PC	0.2		
5	Flux horizontal/vertical		0.27	0.0726
	Single-ring < 400 MeV	0.1		
	Single-ring > 400 MeV	1.9		
	Single-ring multi-GeV	2.3		
	Multi-ring Sub-GeV	1.3		
	Multi-ring Multi-GeV	1.5		
	PC	1.7		
6	Neutrino flight length	10.0	-0.23	0.0005
7	Energy spectrum	5.0	-1.47	0.859
8	Sample-by-sample multi-GeV (SK1)	5.0	-1.68	0.1132
8	Sample-by-sample multi-GeV (SK2)	5.0	0.48	0.0092
2	FC multi-GeV μ / PC (SK1)	6.0	0.01	0.0002
2	FC multi-GeV μ / PC (SK2)	5.0	-0.01	0.0003
26	Solar activity (SK1)	20.0	-1.89	0.089
26	Solar activity (SK2)	50.0	-7.25	0.0210

Table 9.2: Definition of systematic uncertainties related to the neutrino flux. Their values, best fit values, pull values.

Flux of $\overline{\nu_\mu}/\nu_\mu$ ratio (3)

The systematic on the anti-neutrino to neutrino ratio comes from the π^+/π^- ratio in hadronic interaction in the flux calculation. This systematic is common to both SK1 and SK2, and is set to 6%.

	Systematic Description	common to SK1 and SK2		
		σ %	best fit%	pull
	Neutrino interaction			
9	QE cross section	10.0	8.02	0.6425
10	Single-π	10.0	-1.38	0.0190
11	DIS cross section	5.0	-1.67	0.1116
12	Coherent π	100.0	-4.49	0.020
13	NC/(CC)	20.0	1.94	0.0094
21	Nuclear effect	30.0	14.1	0.0022
24	MA in QE and single-π	20.0	-4.48	0.501
25	DIS (Bodek correction)	20.0	24.45	1.4946
27	Single-meson $\pi^0/\pi^+ + \pi^-$	40.0	-2.30	0.033

Table 9.3: Definition of systematic uncertainties related to the neutrinos interaction their values, best fit values, pull values.

Flux of upward going neutrinos versus downward going neutrinos (4)

The uncertainty in the up/down ratio is due to the fact that the ratio is asymmetric below a few GeV due the geomagnetic field of the earth, while above a few GeV the ratio is symmetric. This systematic is common to both SK1 and SK2, and it is energy dependent. It is set to 0.3% and 0.5% for single-ring sub-GeV events with $E_{vis} < 400$ MeV and $E_{vis} > 400$ MeV respectively; to 0.2% for all other types or events.

Flux of horizontal versus vertical neutrinos (5)

The uncertainty in the horizontal/vertical ratio is estimated from the difference in the 3-D calculation methods described in the simulation chapter. This systematic is common to both SK1 and SK2, and it depends on the event type. It is set to 0.1% and 1.9% for single-ring sub-GeV events with $E_{vis} < 400$ MeV and $E_{vis} > 400$ MeV respectively; to 2.3% for FC single-ring multi-GeV events; to 1.3% and 1.5% for FC multi-ring sub-GeV and multi-GeV respectively, and to 1.7% for PC events.

	Systematic Description	SK1			SK2		
		σ	best fit	pull	σ	best fit	pull
	Reconstruction						
16	Ring counting		0.14	0.0002		-0.86	0.0073
	Single-ring $<$ 400 MeV	0.7			2.3		
	Single-ring $>$ 400 MeV	0.7			0.7		
	Single-ring multi-GeV	1.7			1.7		
	Multi-ring Sub-GeV	4.5			8.2		
	Multi-ring Multi-GeV	4.1			0.8		
17	Particle ID 1ring		-0.01	0.0001		-0.02	0.0002
	Single-ring sub-GeV	-0.1			-0.4		
	Single-ring multi-GeV	-0.2			-0.1		
18	Particle ID multi ring		0.26	0.0007		1.27	0.0160
	Multi-ring Sub-GeV	-3.9			-2.2		
	Multi-ring Multi-GeV	-2.2			-3.4		
19	Energy calibration	1.1	-0.14	0.0167	1.70	0.11	0.0043
20	Up-down asym of E calib	0.6	0.21	0.1177	0.60	0.07	0.147
23	PC stop/through top	15.0	0.71	0.0023	19.00	-0.20	0.0001
28	PC stop/through bottom	11.3	-0.94	0.0069	18.00	-2.08	0.0133
29	PC stop/through barrel	7.5	0.56	0.0057	14.00	0.33	0.0006
	Reduction						
14	FC reduction	0.2	0.00	0.0000	0.20	0.00	0.0002
15	PC reduction	2.4	-0.06	0.0007	4.80	-1.42	0.0869
22	Non-ν BG (μ-like)		0.00	0.0000		0.02	0.0005
	Cosmic ray FC sub-GeV	0.1			0.1		
	Cosmic ray FC multi-GeV	0.1			0.1		
	Cosmic ray PC	0.2			0.7		

Table 9.4: Definition of systematic uncertainties related to the reconstruction and reduction. Their values, best fit values, pull values.

Neutrino flight length (6)

The production height of a neutrino in the atmosphere is impossible to reconstruct on an event-by-event basis using the zenith angle, but it can be simulated statistically using the Monte Carlo. The uncertainty on the production height depends on the zenith angle. For upward going neutrinos, the systematic error on the neutrino flight length is only of the order of 1% because the uncertainty in the production height is small compared to the overall flight length. But for a downward-going or horizontal neutrino the production height of the neutrino matters significantly. The uncertainty is related to the structure of the atmosphere. To estimate the uncertainty the simulation calculation is done by changing the density structure of the atmosphere by 10% and observing how the production height changes as a function of the zenith angle. It is common to both SK1 and SK2, and is evaluated to be 10%.

Energy spectrum (7)

The spectrum of primary cosmic rays can be well fit with an E^{γ} form up to where the spectral index γ is set to -2.74. The systematic in the spectral index is common to both SK1 and SK2, and is set to 5%.

Sample-by-sample FC multi-GeV normalization (8)

Different flux calculations predict different energy dependence that cannot be explained by a simple spectral index uncertainty. We therefore compare the number of events predicted by the Honda [44] flux model to the number of events predicted by other models (Fluka [45], Bartol [46]) and we assign a 5% systematic error for samples which include multi-GeV events since all three flux predictions agrees very well below 1 GeV as shown by G.Mituska [6]. This systematic is calculated separately for SK1 and SK2.

FC multi-GeV μ-like events versus PC normalization (2)

The PC sample also contains multi-GeV events and therefore an uncertainty on its normalization should be applied as for the FC multi-GeV sample. But the uncertainty on the PC sample normalization is highly correlated to the uncertainty on the FC multi-GeV sample normalization. To account for this correlation we use a systematic error on the ratio of FC multi-GeV μ-like events to PC events. This systematic error is different for SK1 and SK2 because the software used treat SK1 and SK2 was different. The SK1 value is 6% while the SK2 value is 5%

Solar activity (26)

The primary flux of cosmic rays and therefore the atmospheric neutrino flux is affected by the solar activity as described in Section 5.1. We assign the change in neutrino flux for ± 1 year as the uncertainty related to solar activity. This systematic error is different for SK1 and SK2 since the ± 1 change leads to different uncertainties depending on the stage of the solar cycle. The SK1 value is 20% while the SK2 value is 50%.

9.2.2 Simulation uncertainties - Neutrino Interactions

The cross-sections involved in neutrino interactions are measured by several experiments and theoretically predicted. We use these measurements/predictions to estimate this set of systematic errors. All systematic errors related to neutrino interactions are common for the SK1 and SK2 dataset. A detailed description of the systematic errors linked to neutrino interactions can be found in G.Mitsuka's thesis [6].

9.2.3 Reconstruction uncertainties

Number of rings (16)

The number of rings in one event is reconstructed using a ring counting likelihood as explained in Section 7.2. The single-ring/multi-ring separation uncertainty is estimated by comparing the ring counting likelihood between data and Monte Carlo. This systematic is considered separately for SK1 and SK2 and is sample and energy dependent, as it can be seen in Table 9.4.

Particle identification for the FC 1-ring sample (17) and multi-ring sample (18)

The type of an event (e-like or μ-like) is determined using a PID likelihood as explained in Section 7.3. The systematic errors related to the particle identification algorithm are estimated by comparing the PID likelihood between data and Monte Carlo. Both errors are separate for SK1 and SK2, and are different for each sample. The values can be found in Table 9.4. The minus signs are important when the e-like sample is used to account for correlation properly. In the L/E analysis, we use only the μ-like sample, but I decided to keep the minus signs for coherence with the zenith angle analysis.

Energy calibration (19)

The energy calibration is computed by different means depending on the energy region, as described in Section 4.5. The summary of the energy calibration results is presented in Fig. 9.2 This systematic is separate for SK1 and SK2, the SK1 value is 1.1% while the SK2 value is 1.7%.

Up-down asymmetry of energy calibration (20)

The difference in energy scale for upward-going events compared to downward-going events is calculated using decay electrons from stopping cosmic ray muons. These events are good for calibration because their vertices are distributed all over the fiducial volume of the inner detector and the momentum distribution is almost uniform in all directions. The up/down asymmetry is separate for SK1 and SK2, but both values are set to 0.6%.

PC stopping to through-going (23, 28 29)

The separation between stopping PC events and through-going PC events is estimated by comparing data and Monte Carlo. We look at the distribution of the observed numbers of photoelectrons in the OD (PE_{anti}) divided by the expected number of photoelectrons (PE_{exp}). We fit the distributions of PE_{anti}/PE_{exp} for both data and Monte Carlo to find the means of each distribution. We then shift the MC sample by $mean_{data}/mean_{mc}$, and count how many events classified as stopping before the shift would become through-going. The number of changing events divided by the total number of stopping events is

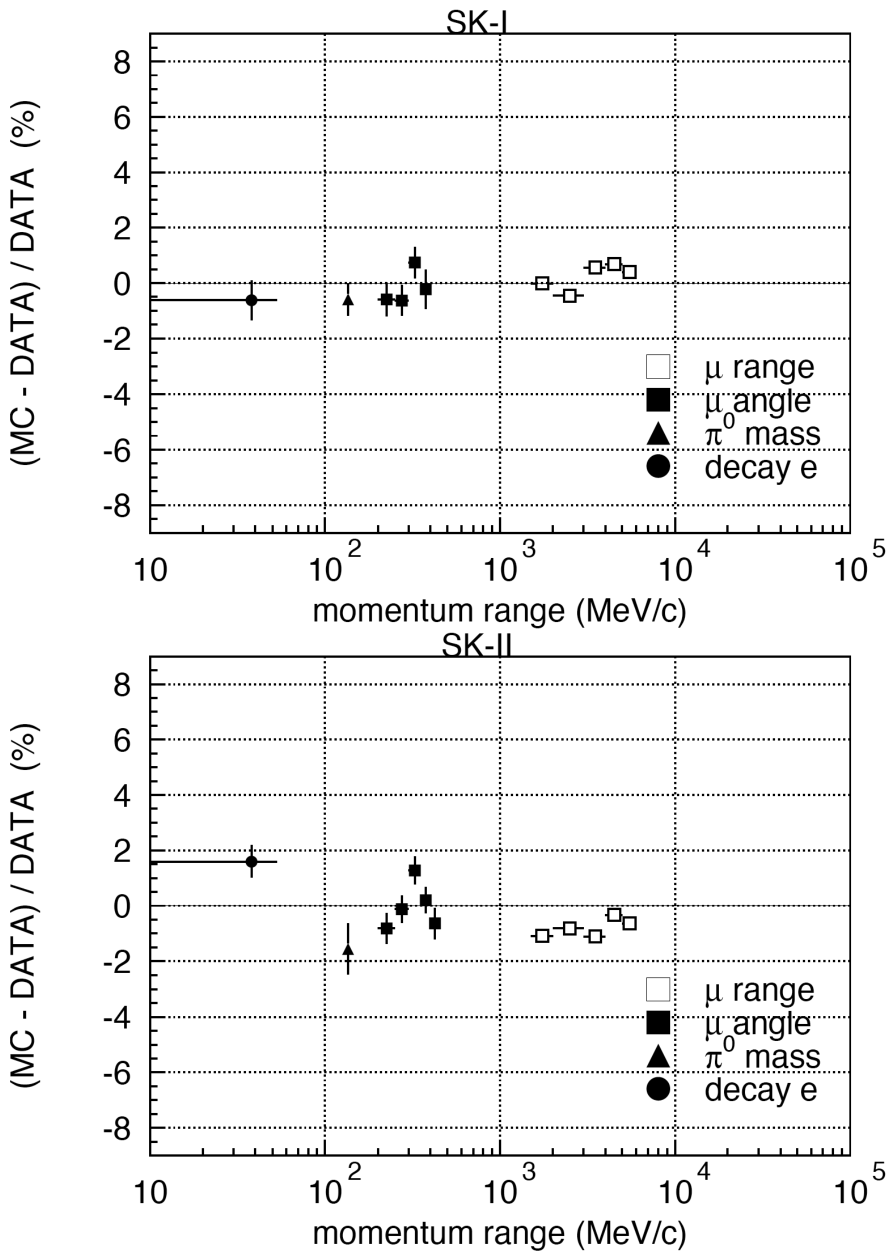

Figure 9.2: Summary of the absolute energy scale calibration for SK1 (top) and SK2 (bottom). The horizontal axis shows the momentum range of each source and the vertical axis shows the deviation of the data from the Monte Carlo predictions. [6].

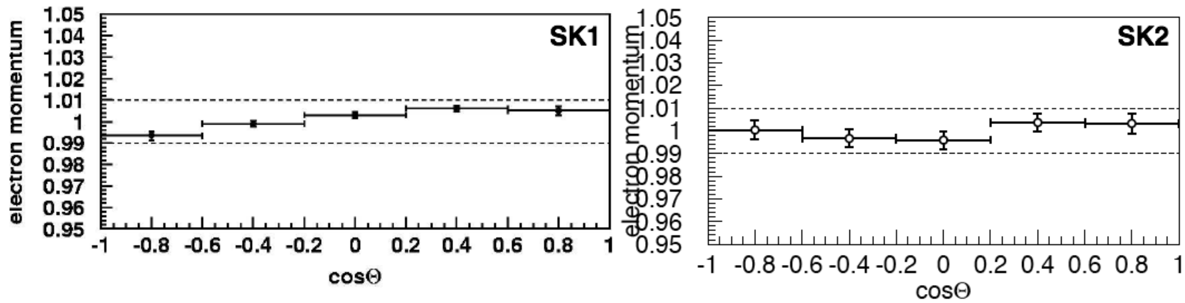

Figure 9.3: The uniformity of the detector gain as a function of zenith angle for SK1 (left) and SK2 (right). The vertical axis in the two figures are the averaged momentum of decay electron events [6].

the systematic uncertainty. Because there are two types of OD PMTs and because most of the old IMB tubes are on the top of the detector while most of the new ones are in the bottom, we estimate this systematic error separately for the top, barrel and bottom of the detector. An example of the PE_{anti}/PE_{exp} distribution for the SK1 barrel is shown in Fig. 9.4, in that case 260 events were moved from PC stopping to PC through-going when the shift was applied, so the systematic uncertainty for the SK1 barrel is 260/3463=0.075. This systematic is separate for SK1 and SK2, the SK1 value is 15% , 11.3 % , 7.5 % for top, bottom and barrel respectively, while the SK2 value is 19%, 18%, 14%, for top, bottom and barrel.

9.2.4 Reduction uncertainties

FC reduction (14)

The systematic uncertainty on the fully-contained reduction is estimated by studying the effect of changing the cuts values. This systematic is separate for SK1 and SK2, the SK1 value is 0.2% while the SK2 value is 0.2%.

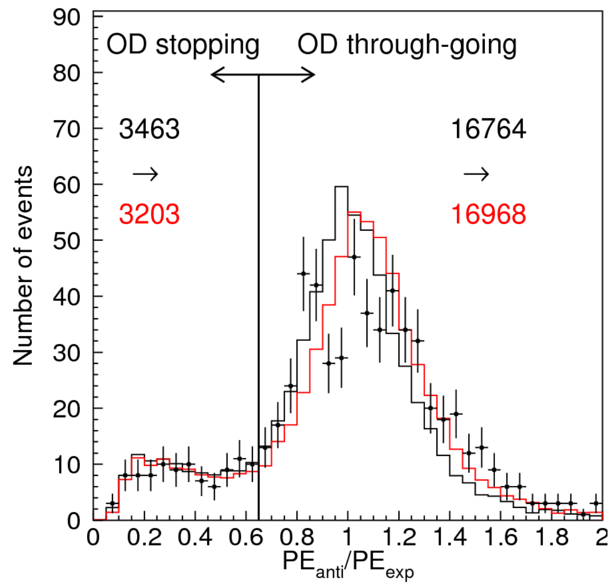

Figure 9.4: PE_{anti}/PE_{exp} for SK1 barrel. The black dots are the data, the black solid histogram is the MC before the shift and the red solid histogram is the MC after the shift.

PC reduction (15)

The estimation of PC systematic uncertainty has been described in detail in W.Wang's thesis [67], it is largely dominated by the systematic uncertainty on the number of hits in the outer detector (`NHITAC`), because `NHITAC` is the variable used to separate FC events from PC events. The PC reduction systematic is separate for SK1 and SK2, the SK1 value is 2.4% while the SK2 value is 4.8%.

Non-neutrino background (22)

The non-neutrino background is estimated during the reduction processes as was presented in Table 6.2 for the background in the fully-contained sample and in Section 6.2.6 for the background in the partially-contained sample. In the L/E analysis, only background events in the μ-like sample are relevant, and they mainly come from cosmic ray muons. The systematic error on the background contamination is separate for SK1 and SK2 and is energy dependent. For SK1 and for SK2, the FC sub-GeV sample and the FC multi-GeV samples both have a systematic error on the background contamination of 0.1%. The PC sample the systematic is set to 0.2% in SK1 and 0.7% in SK2.

9.3 Results

9.3.1 Dealing with non physical region

The best fit result in $\sin^2 2\theta_{23}$ that we obtained is larger than one, which is not a physical result, therefore when drawing the confidence interval we have to correct for that fact. To do so, we followed the 1996 PDG method [75] to treat results close to a physical boundary. In this section, I will describe this method for a 1-parameter fit, it can then be extended for the 2-parameter fit used in the L/E analysis. Assume that the result of a fit falls in an unphysical region (negative mass, $\sin\theta$ greater than one, etc...) and the minimum χ^2 value of the fit is $\chi^2_{min} = 0.853$. If the fit is forced to give a result in the physical region, then $\chi^2_{phys} = 1.353$. The difference between the two χ^2 is $\Delta\chi^2 = 0.5$ which corresponds to $\sigma = 0.25$, and which means that 60% of the gaussian falls in the unphysical region as shown in Fig. 9.5. In order to compute a confidence level, I have to consider only the events that falls in the physical region instead of the entire range. So if I want to compute the 90% confidence level boundary of my hypothetical case, I have to draw the boundary at 90% of the 40% of events that are in the physical region, that is to say at 96% of the entire range. Using confidence level tables, I find that 96% of events corresponds to $\sigma = 1.76$ and therefore $\chi^2_{90,corr} = 3.10$. So the 90% confidence level boundary is drawn at $\chi^2_{90,phys} = \chi^2_{min} + \chi^2_{90,corr} = 0.853 + 3.10 = 3.953$.

9.3.2 Oscillation results

The results of the L/E analysis for the SK1 (1489 days) and SK2 (803 days) data for the ν_μ to ν_τ hypothesis are presented in this section. For this analysis 500 years of fully-contained and 500 years of partially-contained Monte Carlo events were used. The SK1

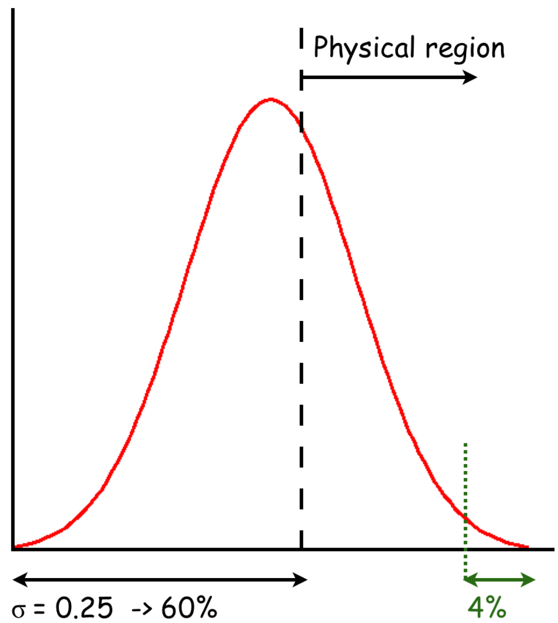

Figure 9.5: 1996 PDG method to treat results close to physical boundary.

+ SK2 data are presented in Fig. 9.6 with unoscillated Monte Carlo and the oscillated (best fit) Monte Carlo overlaid in red on top of the data.

To see the oscillation pattern, we divide the data and the best fit Monte Carlo by the unoscillated Monte Carlo. The result of this division is shown in Fig. 9.7, with the theoretical survival probability for comparison.

Finally, the result of the reduced χ^2 is shown in Fig. 9.8 and the slices in Δm^2_{23} and $\sin^2 2\theta_{23}$ are shown in Fig. 9.9. If we allow the fit to go in the unphysical region, the χ^2 is equal to 77.1 for 83 degrees of freedom, and the best fit parameters are $\sin^2 2\theta_{23} = 1.04$ and $\Delta m^2_{23} = 2.2 \times 10^{-3}$ eV^2. If we constrain the fit to lie in the physical region, the χ^2 is equal to 78.2.0 for 83 degrees of freedom, and the best fit parameters are $\sin^2 2\theta_{23} = 1.00$ and $\Delta m^2_{23} = 2.2 \times 10^{-3}$ eV^2. At 90% confidence level, we have $\sin^2 2\theta_{23} > 0.94$ and 1.85×10^{-3} eV$^2 < \Delta m^2_{23} < 2.65 \times 10^{-3}$ eV^2

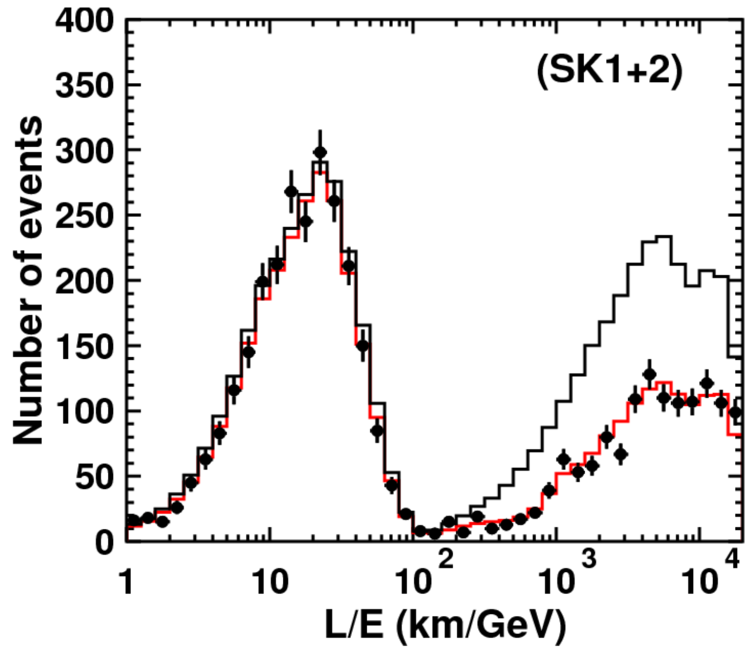

Figure 9.6: L/E spectrum. Black circles are the SK1+SK2 data, black histogram is the unoscillated Monte Carlo, red is the best fit oscillated Monte Carlo.

9.3.3 Neutrino decoherence and decay

There are other theories that predict the behavior of atmospheric neutrinos, these non-standard effects have been studied in detail with the Super-Kamiokande data by W.Wang [67] and G.Mituska [6] in their Ph.D. theses. Neutrino decay and neutrino decoherence are two such theories. As it can be seen in Fig. 9.10, one form of neutrino decay and one form of neutrino decoherence predict a deficit of upward-going muon neutrino but they do not predict an oscillatory pattern. Therefore studying the L/E spectrum of the atmospheric neutrino data, and comparing it to predictions from these theories is the best way to constrain these models. Comparing to these theories also yields a benchmark for determining a significance of our observation of the oscillation pattern. Comparing against no oscillation gives a very large χ^2 difference, but does not tell us if we resolve the first oscillation minimum. In this section, I present the SK1 + SK2 results for neutrino decay and neutrino decoherence and compare them to the neutrino oscillation results.

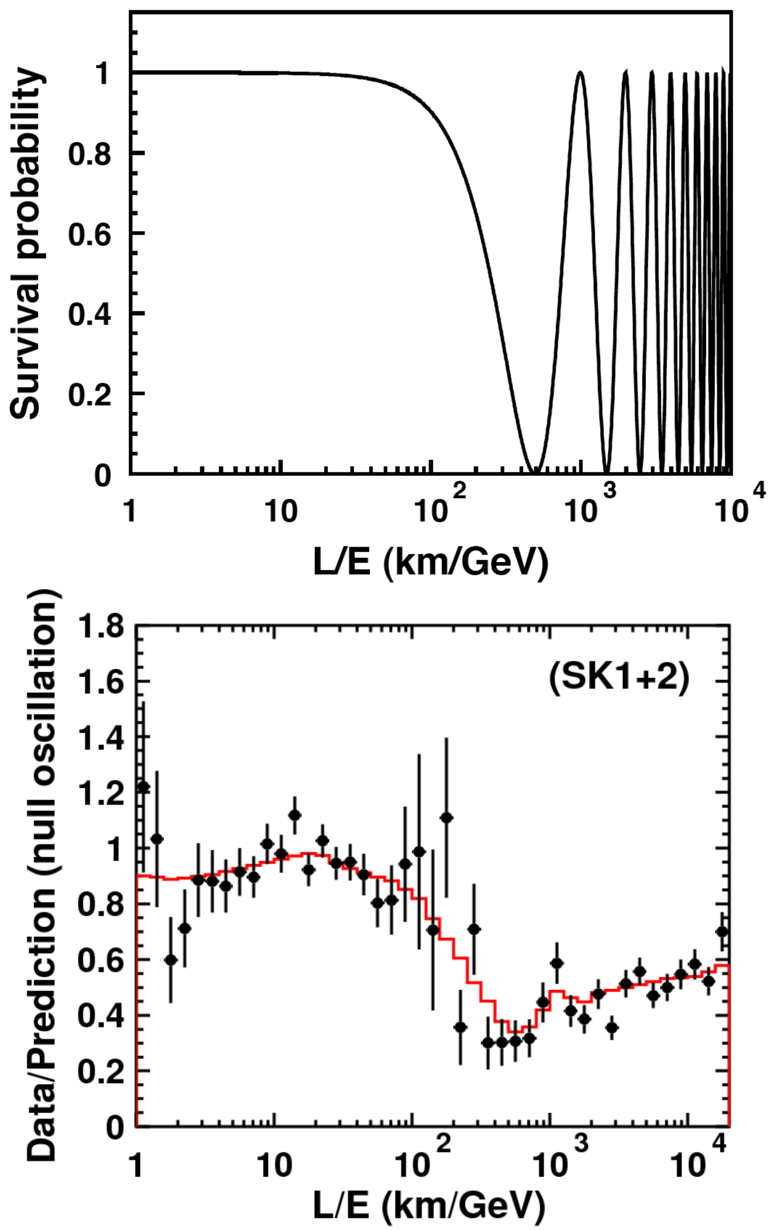

Figure 9.7: Top: Theoretical survival probability. Bottom: Experimental survival probability. (black circles are the SK1+SK2 data, red is the best fit oscillated Monte Carlo).

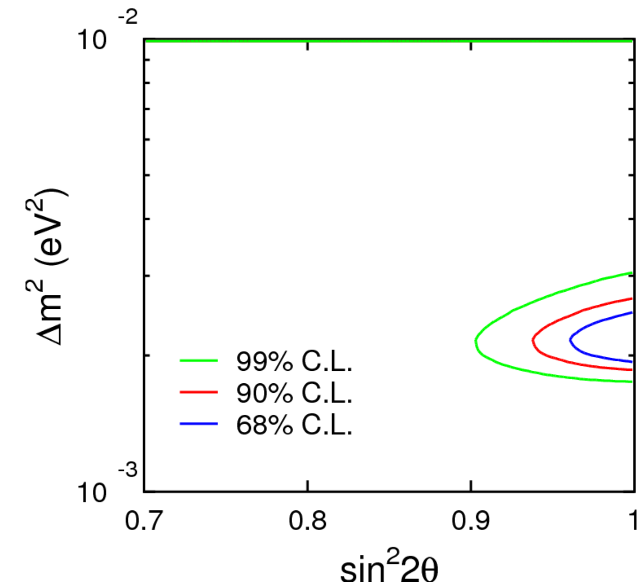

Figure 9.8: Contour map of the oscillation analysis for the SK1 + SK2 dataset.

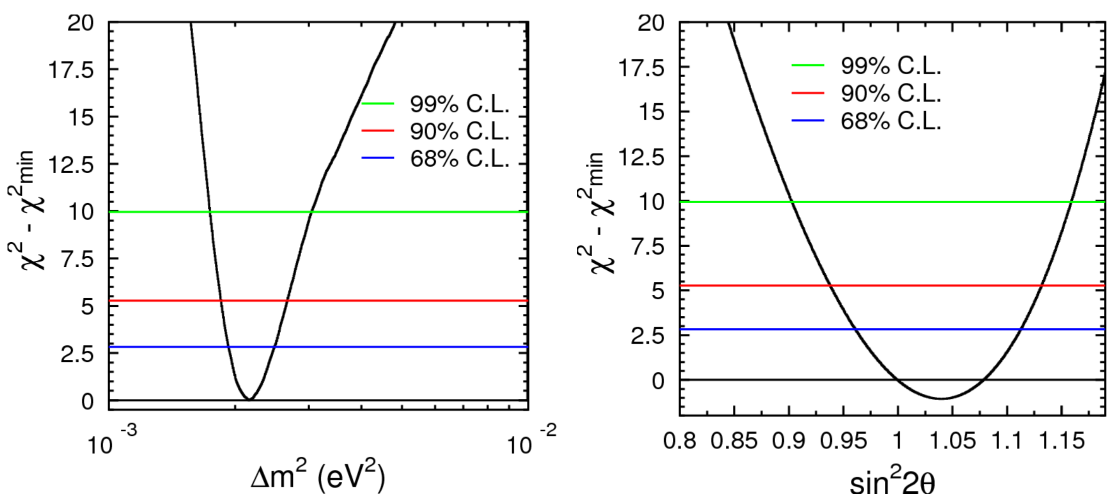

Figure 9.9: Left: Slice in Δm^2_{23}. Right: in $\sin^2 2\theta_{23}$.

9.3.4 Neutrino Decay

Neutrino decay could also explain the deficit of upward going muon neutrinos [71]. In the Standard Model, neutrinos cannot decay because they are massless, but several models predict the decay of massive neutrinos. Lower limits on the lifetime of the neutrinos come from radiative decay channels as $\tau/m > 15.4$ sec/eV, where τ is the lifetime and m the mass of the neutrino [72]. The effect of neutrino decay on the survival probability

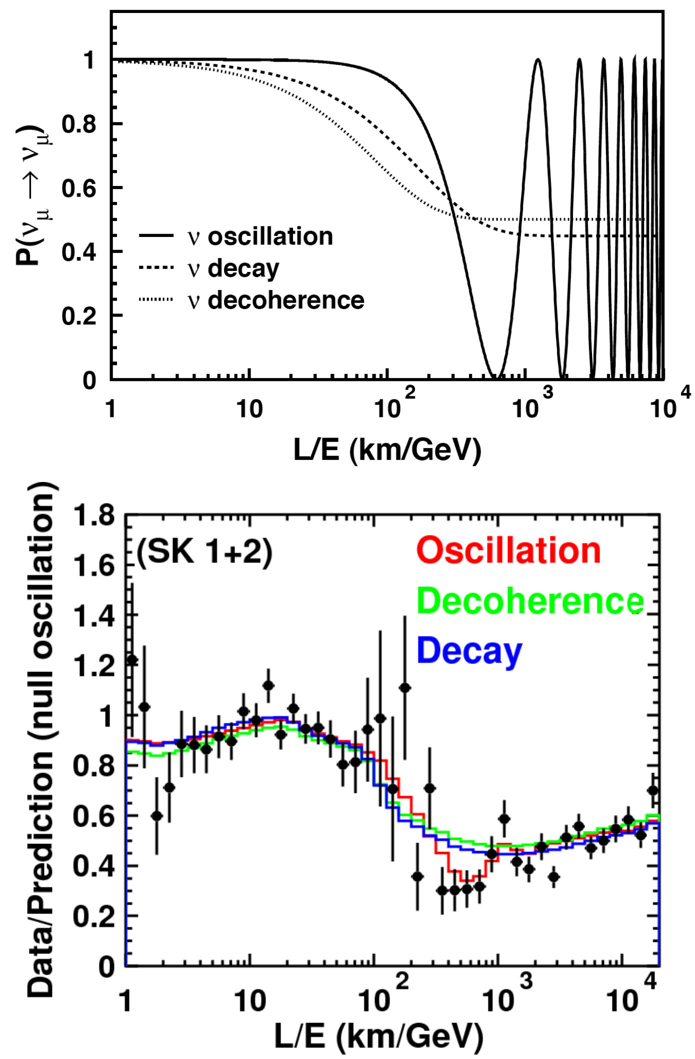

Figure 9.10: Top: Theoritical survival probability of muon neutrinos for neutrino oscillation, neutrino decay and neutrino decoherence. Bottom: Survival probability for SK1 + SK2 data (black circles) and compared with the best fit results for neutrino oscillation (red), decoherence model (green) and decay model (blue).

of ν_μ is the following:

$$P(\nu_\mu \to \nu_\mu) = \left[\sin^2\theta + \cos^2\theta \exp\left(-\frac{m_2}{2\tau_2}\frac{L_\nu}{E_\nu}\right)\right]^2 \tag{9.6}$$

If we fit the atmospheric neutrino data with a neutrino decay assumption instead of a neutrino oscillation assumption, the final χ^2 for the SK1 + SK2 dataset is 92.1 for 83 degrees of freedom so the $\Delta\chi^2$ comparing neutrino decay and neutrino oscillation is

13.9, which is 3.7 σ away from the oscillation result.

9.3.5 Neutrino Decoherence

The deficit of upward-going neutrino can also be explained by neutrino decoherence induced by new physics like quantum gravity [73]. The decoherence of neutrino can be parametrized by $\gamma = \gamma_0(E_\nu/GeV)^n$ and in the case where $n = -1$, the effect on the survival probability is a deficit of upward-going neutrino but without an oscillation pattern.

$$P(\nu_\mu \to \nu_\mu) = 1 - \frac{1}{2}\sin^2 2\theta \left[1 - \exp(-\gamma_0 \frac{L_\nu}{E_\nu})\right] \tag{9.7}$$

If we fit the atmospheric neutrino data with a neutrino decoherence assumption instead of a neutrino oscillation assumption, the final χ^2 for the SK1 + SK2 dataset is 100.4 for 83 degrees of freedom so the $\Delta\chi^2$ comparing neutrino decoherence and neutrino oscillation is 22.2, which is 4.7 σ away from the oscillation result.

Chapter 10

Conclusion

In this thesis, I presented the result of the L/E analysis of the atmospheric neutrino data collected between 1996 and 2005 by the Super-Kamiokande water Cherenkov detector. There were two data-taking periods during that time, SK1 lasted from 1996 to 2001 and SK2 from 2002 to 2005. We used the fully-contained and partially-contained event samples with specific resolution cuts to ensure that the oscillatory pattern of the survival probability of muon neutrinos is not washed out. This analysis demonstrates that the survival probability of muon neutrinos follows a sinusoidal function as presented in Fig. 10.1.

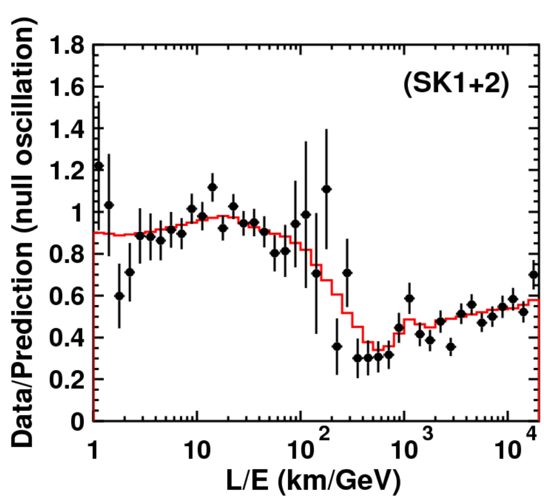

Figure 10.1: Experimental survival probability of muon neutrinos. (black circles are the SK1+SK2 data, red is the best fit oscillated Monte Carlo).

We created a set of Monte Carlo data and by fitting this Monte Carlo to the Super-Kamiokande detector data assuming 2 flavor oscillation of $\nu_\mu \to \nu_\tau$, we found that the allowed regions for the two parameters, $\sin^2 2\theta_{23}$ and Δm^2_{23}, at 90% confidence level are:

$$0.94 < \sin^2 2\theta_{23} \tag{10.1}$$

$$1.85 \times 10^{-3}\ \mathrm{eV}^2 < \Delta m^2_{23} < 2.65 \times 10^{-3}\ \mathrm{eV}^2 \tag{10.2}$$

The minimum χ^2 value for the 2 flavor fit is 78.2/83 d.o.f. if we constrain the fit in the physical region of $\sin^2 2\theta_{23}$.

The L/E analysis gives a better measurement of Δm^2_{23} than the traditional zenith angle analysis, as it can be seen in Fig. 10.2. Our central value for Δm^2_{23} is consistent with the recent MINOS [27] result but MINOS constrains Δm^2_{23} better (see Fig. 10.2). Atmospheric neutrinos are still currently the best tool to measure the angle $\sin^2 2\theta_{23}$, but accelerator neutrinos and experiments like MINOS (and soon T2K), are now more powerful at measuring the mass splitting Δm^2_{23}.

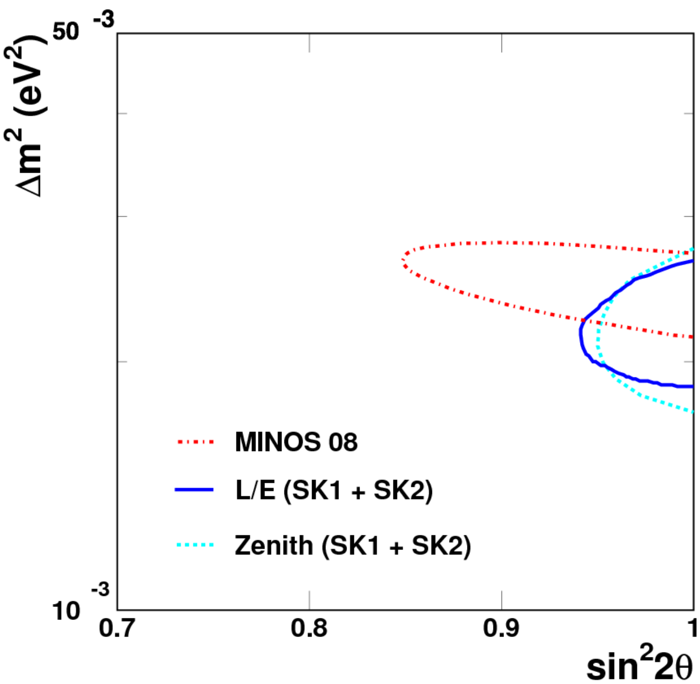

Figure 10.2: 90% CL contours for SK1 + SK2 analyses: L/E (dark blue, solid) and zenith (light blue dashed), and for MINOS 08 (red, dashed).

Appendix A

Partially contained data reduction

In this Appendix, I describe the changes made to PC reduction for SK3. During the reconstruction of the winter 2005-2006, when the full photo-coverage of SK was rebuilt, we also added a segmentation of the outer detector. This segmentation gives us a new tool to select partially contained neutrino events. Six months later, we also updated the computer facilities of SK, and with more processing power, significant improvements to PC reduction were made possible. The goal of my work was to improve the efficiency of the PC reduction from 85% to above 97% while keeping the background contamination as low as possible. The description of PC reduction for the SK1 and SK2 dataset is done in Chapter 6.

A.1 Purpose of the OD segmentation added for SK3

One of the main modifications of the detector in the SK3 period is the addition of the OD segmentation. A schematic view of the segmentation is presented in Fig. A.1.

The purpose of the segmentation is to be able to better identify cosmic ray muons which are clipping the corner of the detector. Figure A.2 shows the distribution of hits in the wall versus the number of hits in the end-caps (top and bottom of the detector).

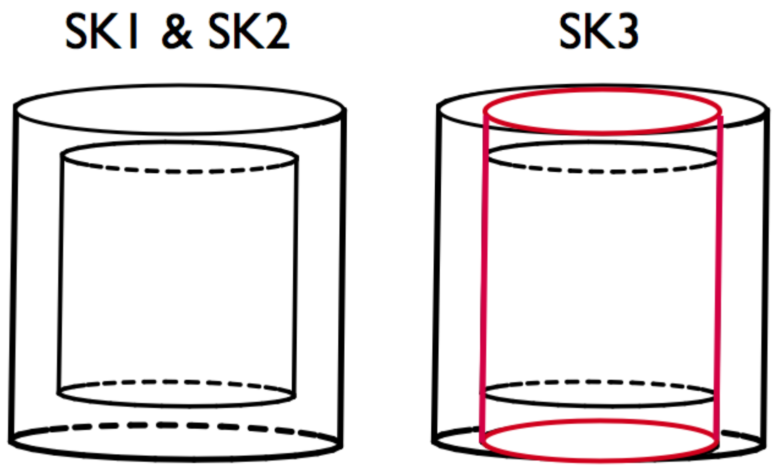

Figure A.1: Schematic view of the OD segmentation (red lines) added in SK3

The top figure is for SK2 and the bottom figure is for SK3. In both cases we keep events which do not have a high number of hits in both the wall and the end-caps, since such events are very likely to be corner clipper events. It is clear that adding the OD segmentation cleaned the region around the cut shown in Fig. A.2 and denoted by the red line. As a result, the cut is more efficient. Since this cut is applied very early in the PC reduction process, adding the OD segmentation allowed us to loosen some of the cuts applied later in the PC reduction process and to gain efficiency in PC reduction

A.2 Modifications to PC reduction for SK3

The purpose of the following modifications was to improve the efficiency of PC reduction. Since the computer facilities for the Super-K detector were upgraded in 2006, we are now able to rely much more on CPU-consuming fitters like `tfafit` used in PC4 and PC5. Some cuts were removed from PC2 and PC3; PC4 was completely redone and is now based mainly on the muon fitter `muboy`. PC5 mainly remains the same as before, but some cuts were added. The definitions of all the old cuts are not repeated here and can be found in Section 6.2.

PC1: No modifications except OD segmentation

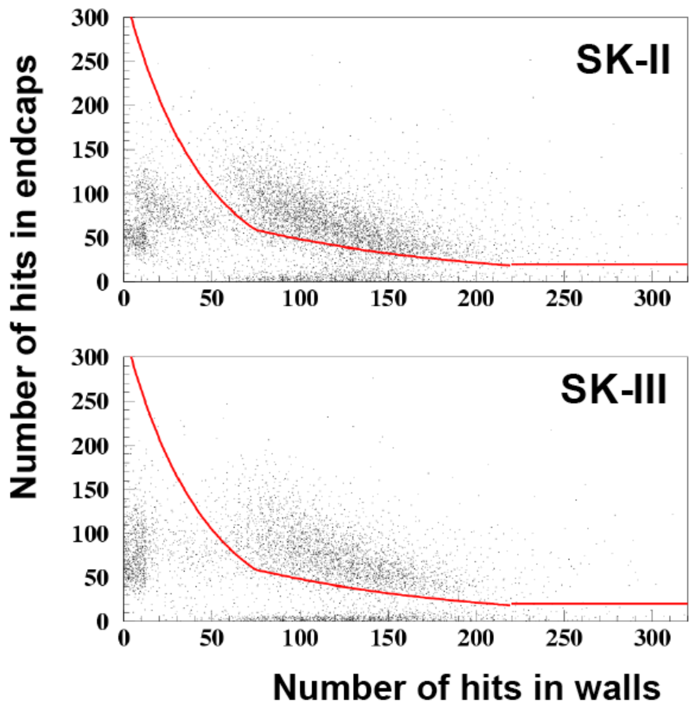

Figure A.2: Number of hits in the OD wall versus number of hits in the OD end-caps before segmentation (SK2, top) and after segmentation (SK3, bottom). Events that are above the red line are corner clippers events and are rejected during PC reduction.

PC2: In PC2, the only modifications were to remove the two cuts that were the biggest causes of inefficiency.

- `numendcap vs numwall` (SK-II): Remains the same.
- `nouter2`: Remains the same.
- `nouter`: This cut was removed.
- `pe200`: This cut was removed.

PC3: The flasher cut is the same as before. The `ehit8m` cut was moved to PC5, see PC5 section for more information.

PC4:

PC4 is now completely based on the muon fitter `muboy`. Since this is a muon fitter, it will not give good results for real PC events, but it is very powerful at identifying cosmic ray muons. One of the features of `muboy` is that it characterizes each event as either, stopping muon, through-going muons, multiple muons or corner clipper muons. 96% of PC Monte Carlo events inside the fiducial volume are classfied as multiple muons, whereas 97% of background events are classified as either stopping or through-going muons. We will take advantage of this fact by asking an event to fulfill different conditions depending on what its `muboy` classification was. We defined 6 variables which use the `muboy` information as defined below.

- `muboy angle:` This is the angle between the `muboy` fitted direction and the vector between the `pfit` vertex and the center of the highest charge OD cluster. If `muboy angle` is less that $90°$ then the event passes the cut. This cut is designed to remove cosmic ray muon which stop in the tank.

- `muboy dotprod:` This cut is similar to `muboy angle` but instead of using the center of the highest charged OD cluster, we use the earliest saturated ID pmt. This is designed to remove both stopping and through-going cosmic ray muons. If `muboy dotprod`> -0.8 then an event passes the cut.

- `muboy track length:` This is the length of the muon track given by `muboy`. Very long track length hints toward cosmic ray muons, so events with `muboy track length`< 1750 pass this cut.

- `muboy goodness:` This is the goodness of fit given by `muboy`. A good fit points toward a cosmic ray muon, so events with `muboy goodness`< 0.52 pass this cut.

- `muboy corner:` This is the distance between the `muboy` entry point and the corners of the tank. We ask an event to have `muboy corner`≥ 300 to pass this cut.

- `muboy ehit8m`: This is similar to the PC3 `ehit8m` cut, but we use the `muboy` entry point instead of the entrance point extrapolated using `pfit`. An event passes this cut if `muboy ehit8m`≤ 10.

If an event is classified as **through-going** by `muboy` then it has to pass four out of the following 5 cuts: `Muboy angle, Muboy dotprod, Muboy tracklength, muboy goodness and muboy corner`. If an event is classified as **stopping** by `muboy` then it also has to pass four out of the same set of 5 cuts, but in addition it has to pass the `muboy dotprod` cut, and it has to pass either the `muboy ehit8m` cut or have a `muboy goodness`< 0.5. If the event is classified as something else than stopping or through-going then it only needs to pass two of the set of 5 cuts defined earlier.

Finally we kept the cut on the total ID charge in PC4 but we changed the value of the cut.

- `qismsk`: Total charge in the inner detector. This is to remove events with too little energy in the ID. The cut is now set at 2900.

PC5:

The fast cuts in PC5 remained the same. Most of the slow PC5 cuts remained the same, but we now classify them between hard cuts and soft cuts. Hard cuts, are cuts that an event is *required* to pass in order to be kept. Soft cuts are part of an "all-but-one" setup. An event may fail zero or one soft cut in order to be kept. This was implemented in order to improve efficiency, but new cuts had to be introduced in order to remove background events.

Hard cuts:

- `Bye Bye cut`
- `No ID`
- `Ano OD`

- `Veto cut`
- `Angle` The value of this cut was change from 90° to 75°. The same cut is applied for the results of both fitter, `apfit` and `msfit`.
- `Geji cut`
- `dcorn:` (New) This is a new cut which removes an event if the precise fitter (`apfit`) vertex is at more than 150 cm from the corner of the tank.
- `nncluster cut:` (New) This cut uses the `nncluster` algorithm to count the number of clusters found in the OD. This cut is used only for very energetic events (`apevis` > 20000). In that case, if `nncluster` finds 2 clusters, the event is rejected.

Soft cuts:

- `Cluster cut:` (Modified) We modified the cut values to `nhit1st`< 10 and `nhit2nd`$<$ 17 .
- `Through mu`
- `New evis`
- `Stop mu`
- `St cone`
- `Evis`
- `Hits:` (Modified) We look at the number of OD hits within 8m of the reconstructed entry point and in a 500ns time window. The PC5 cut uses `apfit` to reconstruct the entry point and the PC3 cut uses `pfit`. We compared the entry point given by both fitters and if they are within 1500 cm of each other, we only apply the PC5 version of the cut. If the fitters disagree by more than 1500 cm, then an event has to pass both the PC3 and the PC5 cuts.

- `Muboy angle:` (New) Since the PC4 criterion is very loose for events which are not classified as stopping or through-going muons, we use `muboy angle` again in PC5.

- `Mue decay:` (New) For events of very high energy (`evis` > 25000) we look at the number of decay electrons found. If no decay electron is found, we reject the event.

A.3 New PC reduction results

The SK3 dataset goes from run 30857 to run 35165, which covers 549.7 days of data. We also used 60 years of PC Monte Carlo generated with the version of the NEUT library tagged as 02b. The flux model was used to generate the MC as the 2001 version of the Honda flux (honda01) but we reweighted the Monte Carlo so that it matched the predictions of the 2003 version of the Honda flux (honda03). We ran PC reduction using the version of Super-Kamiokande libraries tagged as 07d. Finally the parameters related to the outer detector needed by the detector simulated `skdetsim` were tuned in May 2007. These parameters were retuned in winter 2009.. A better tuning of the OD parameters in `skdetsim`, can decrease systematic uncertainty.

Efficiencies:

After all the modifications described above, Table A.1 shows the old and new PC reduction efficiencies, using the SK-III dataset and Monte Carlo, and Table A.2 shows the detail of the final dataset.

PC data:

For the SK3 PC dataset, the final event rate is 0.66 ± 0.03 events per day. The event rate after each reduction step is shown in Fig. A.3. It is flat which shows that data taking was running smoothly. The up/down ratio is 0.51 ± 0.07 and the zenith angle plot is shown in Fig. A.4.

	SK-III (550 days)		
	Old Eff. (June 07)	New Eff (April 08)	Data (New reduction)
PC1	99.7%	99.7%	12178704
PC2	94.2%	99.2%	4699463
PC3	92.8%	99.2%	4692857
PC4	85.4 %	98.5%	80417
PC5	84.0%	97.1%	663
PC5(FV)	78.8%	90.1%	366

Table A.1: PC reduction efficiencies for old and new PC reduction

550 days of data	PC	BG
Inside FV	360	6
Outside FV	232	65

Table A.2: SK-III Dataset for 551 days of data

BG contamination:

By eye-scanning the final dataset, we found 6 BG events and 366 PC events inside the fiducial volume in 550 days of data. This corresponds to a BG contamination of $1.6 \pm 0.67\%$

In order to estimate the BG contamination inside the FV, we fit an exponential to the `dwall` (distance from vertex to the wall) distribution of BG events in the whole SK volume (not only the fiducial volume). The sample of BG events was obtained by eye-scanning the final data sample, with the `corner cut` removed in PC5. We had to remove that cut in order to have a correct estimate of the number of event very close to the wall. Fig. A.5 shows this fit. Using this method we estimate a BG contamination of 1.9 BG event inside the fiducial volume and therefore a BG contamination of $0.5 \pm 0.4\%$.

A.4 PC reduction systematics uncertainty

In order to compute the systematic uncertainty on the efficiency of PC reduction, we searched for systematic shifts between data and Monte Carlo in the cut variables.

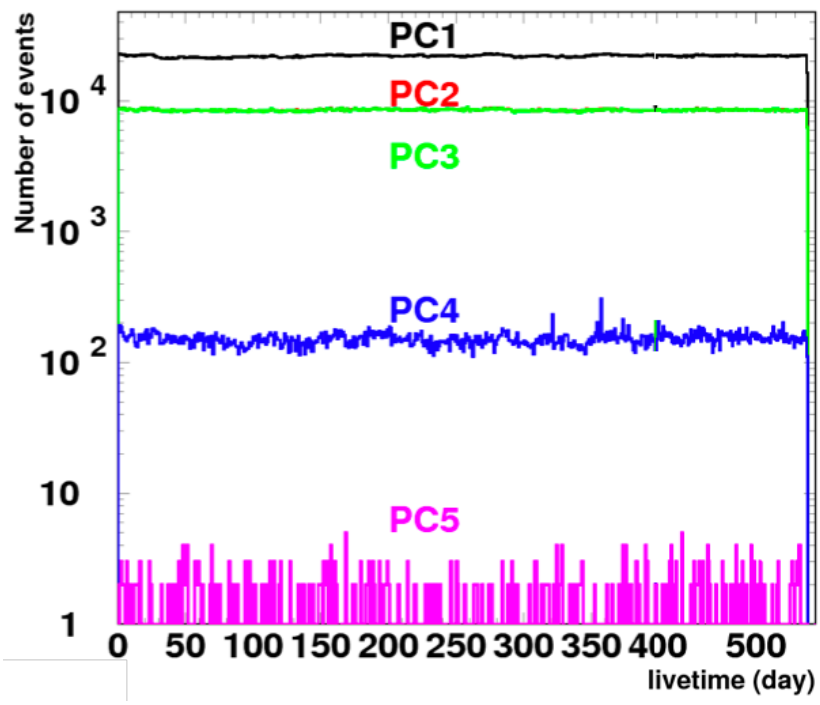

Figure A.3: Event rate for PC SK3 data

In PC2, the only variables that presented a shift was the number of hits in the wall (`numwall`). After shifting the cut value to account for the difference between data and Monte Carlo, and running PC reduction with this new cut value, we obtain a systematic uncertainty of 0.04%. There was no uncertainty in PC3 since the only active cut in PC3 is the flasher cut.

In PC4, all of the variables presented small shifts between data and Monte Carlo. Out of 5 variables, 4 had a shift that would decrease the PC efficiency, and one had a shift that would increase it. We modified the cut variables slightly separately for those two sets and ran PC reduction again with these modifications to estimate the systematic uncertainties due to each set. The set of cuts that decreased the efficiency gave a systematic uncertainty of 0.14%, the set that increased it, gave negligible uncertainty.

For PC5, we treated hard and soft cut differently. For hard cuts, we looked at each cuts individually and found that only the `angle cut` had a difference between data

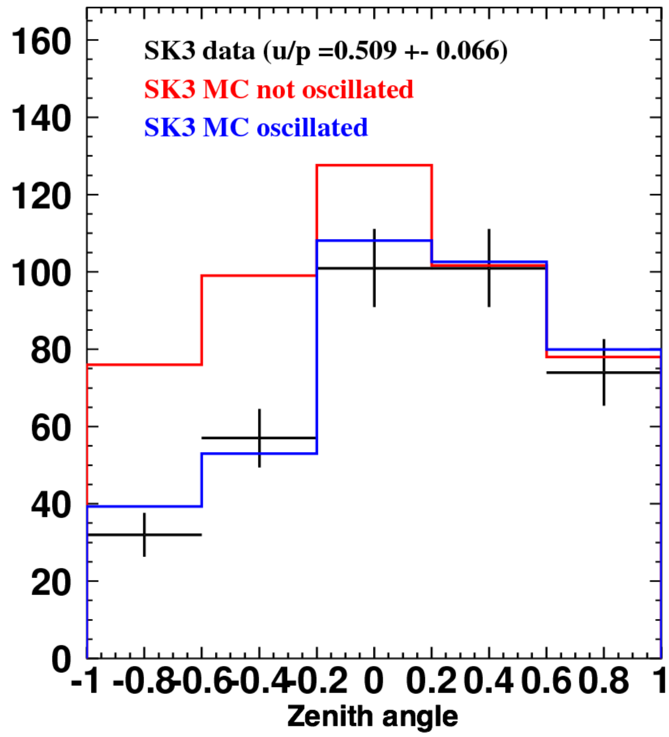

Figure A.4: Zenith angle for PC SK3 data (black), oscillated MC (blue), unoscillated MC (red).

and Monte Carlo, and the systematic associated with this cut was 0.21%. For soft cuts, we checked the systematic uncertainty associated with all the cuts that increase efficiency and obtained 0.01%. The systematic uncertainty associated with all the cuts that decrease efficiency was found to be 0.09%.

In addition to the reduction efficiency, we also computed the uncertainty on the `nhitac` (number of hits in the OD) variable, since it is this variable that we use to decide if an event is fully-contained (`nhitac`< 16) or partially-contained (`nhitac`≥ 16). We found a systematic uncertainty of 0.99% in `nhitac`. This is the dominant systematic uncertainty in PC reduction.

Finally adding these systematic uncertainties in quadrature gives a final PC systematic uncertainty of $\sqrt{0.04^2 + 0.14^2 + 0.09^2 + 0.21^2 + 0.99^2} = 1.03\%$.

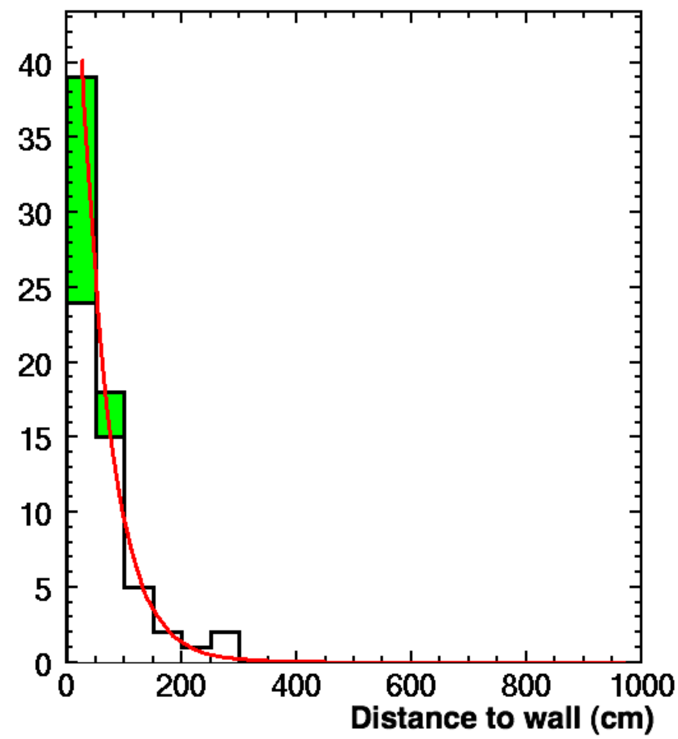

Figure A.5: Distance to the wall (cm) for BG events accepted by PC reduction. The green shaded area contains events which are added when we remove the `corner cut` in PC5.

Appendix B

Distributions of reconstructed variables

In this Appendix, I will present several sets of distributions concerning each of the reconstructed variables. This is important to make sure that we understand the detector and the Monte Carlo simulation correctly. Since we already know that neutrino oscillate, it is reasonable to compare our data with a set of what we call "oscillated" Monte Carlo. The "oscillated" Monte Carlo, is a Monte Carlo which includes our current understanding of neutrino oscillation. The oscillation parameters used in this Monte Carlo are $(\sin^2 2\theta, \Delta m^2) = (1.00, 2.5 \times 10^{-3} eV^2)$.

B.1 Vertex distributions

When we reconstruct a neutrino event, we are interested in where the interaction took place in the detector. The description of how the vertex is found is in Section 7.4. We expect neutrino interaction to happen uniformly across the detector and therefore any unexpected cluster of events would indicate that our understanding of either the detector or software tools (reduction and reconstruction) is faulty. In particular, an

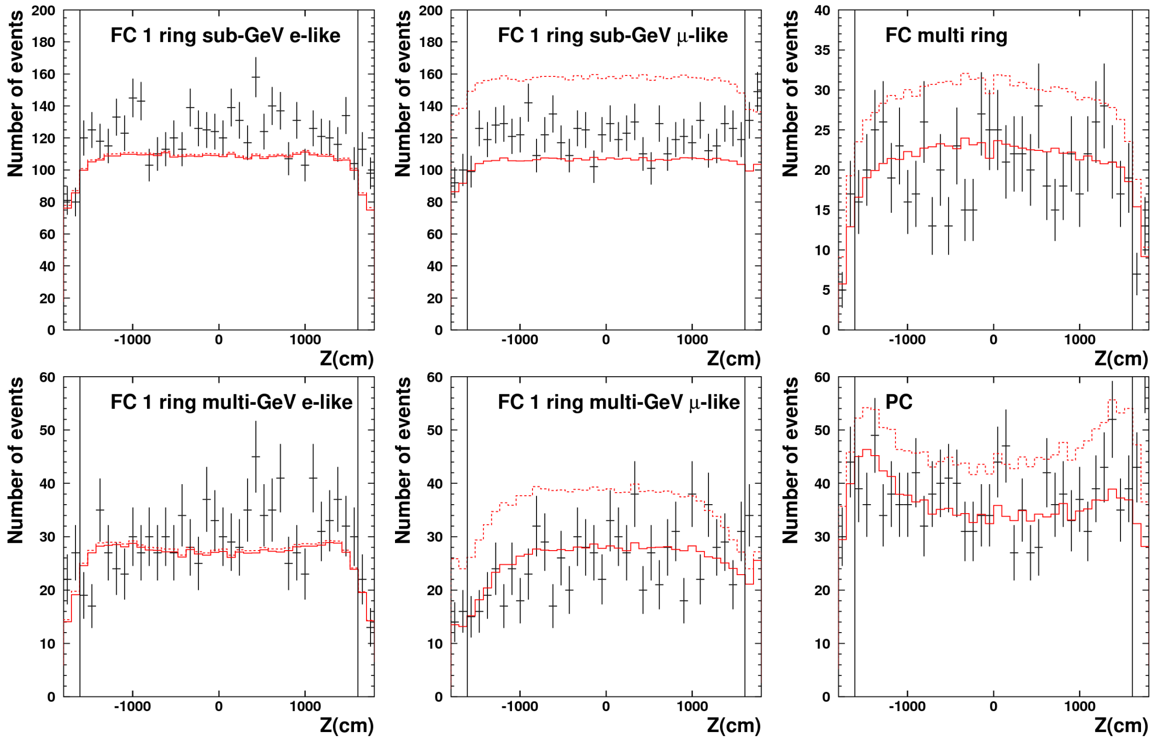

Figure B.1: Vertex for SK1 (Z). Black dots are data, red solid line is oscillated Monte Carlo assuming 2 flavor $\nu_\mu \rightarrow \nu_\tau$ oscillation with $(\sin^2 2\theta, \Delta m^2) = (1.00, 2.5 \times 10^{-3} eV^2)$, red dashed line is unoscillated MC. Top row: FC Sub-GeV 1ring e-like, FC Sub-GeV 1ring μ-like, FC multi-ring μ-like. Bottom row: FC Multi-GeV 1-ring e-like, FC Multi-GeV 1ring μ-like, PC

accumulation of events in the top of the detector would indicate that our rejection of cosmic ray background event is not done properly. Fig. B.1 and Fig. B.3 show the Z distributions for SK1 and SK2 respectively. Similarly Fig. B.2 and, Fig. B.4 show the R^2 distributions for SK1 and SK2 respectively.

B.2 Number of ring distributions

The distribution of the number of rings is an important check of our reconstruction software and of our Monte Carlo simulation. Figure B.5 and Figure B.6 show the number of ring distributions for SK1 and SK2 respectively.

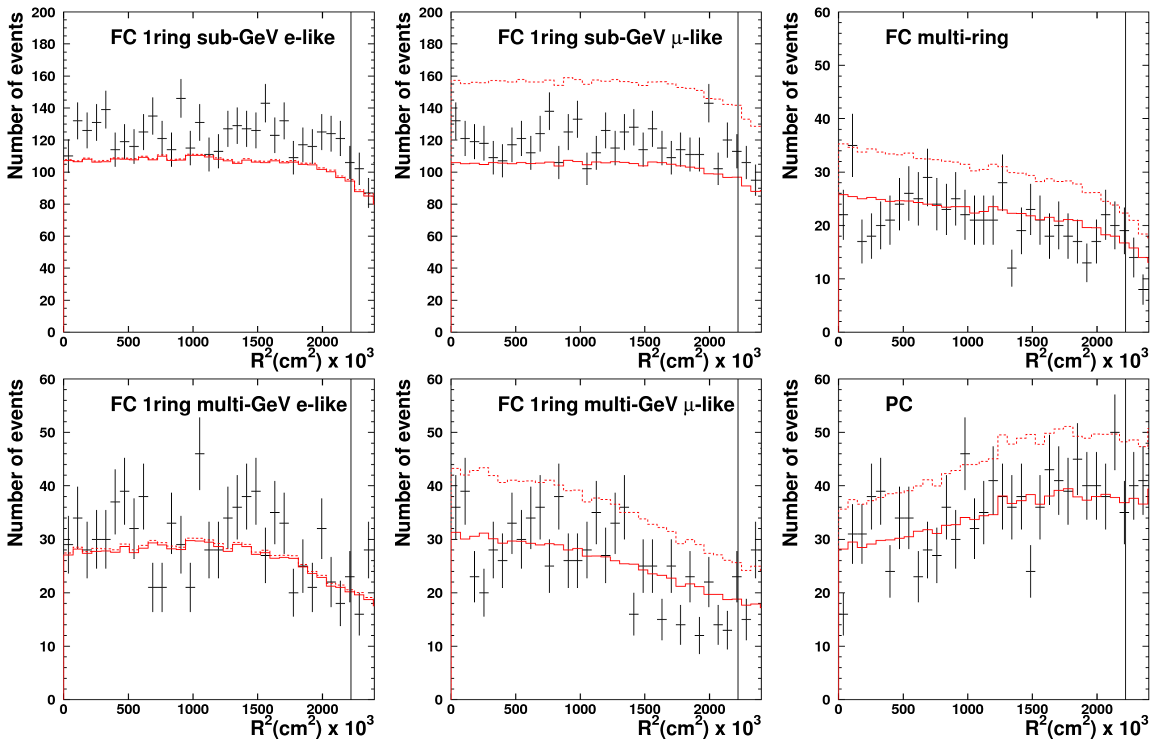

Figure B.2: Vertex for SK1 (R^2). Black dots are data, red solid line is oscillated Monte Carlo assuming 2 flavor $\nu_\mu \to \nu_\tau$ oscillation with $(\sin^2 2\theta, \Delta m^2) = (1.00, 2.5 \times 10^{-3} eV^2)$, red dashed line is unoscillated MC. Top row: FC Sub-GeV 1ring e-like, FC Sub-GeV 1ring μ-like, FC multi-ring μ-like. Bottom row: FC Multi-GeV 1-ring e-like, FC Multi-GeV 1ring μ-like, PC

B.3 PID distributions

Since the L/E analysis studies the oscillation of ν_μ into ν_τ, it is crucial to understand our ability to distinguish muon-like events from electron-like events. Comparing the distribution of the PID parameter for each sample is a check of our reconstruction software and our Monte Carlo simulation. As you can see in Fig. B.7 and Fig. B.8, the separation between e-like and μ-like events is very good for single-ring events. For multi-ring events, it is more challenging. Most of PC events are CCν_μ events so we do not use the PID for PC events.

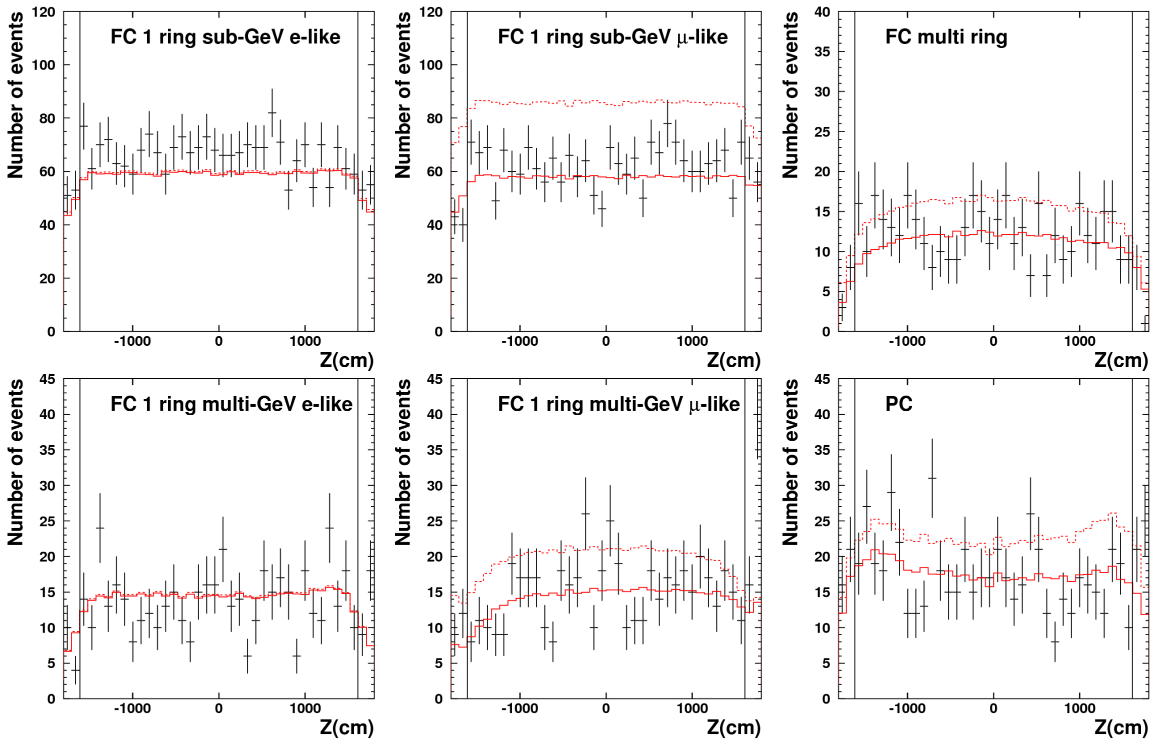

Figure B.3: Vertex for SK2 (Z). Black dots are data, red solid line is oscillated Monte Carlo assuming 2 flavor $\nu_\mu \rightarrow \nu_\tau$ oscillation with $(\sin^2 2\theta, \Delta m^2) = (1.00, 2.5 \times 10^{-3} eV^2)$, red dashed line is unoscillated MC. Top row: FC Sub-GeV 1ring e-like, FC Sub-GeV 1ring μ-like, FC multi-ring μ-like. Bottom row: FC Multi-GeV 1-ring e-like, FC Multi-GeV 1ring μ-like, PC

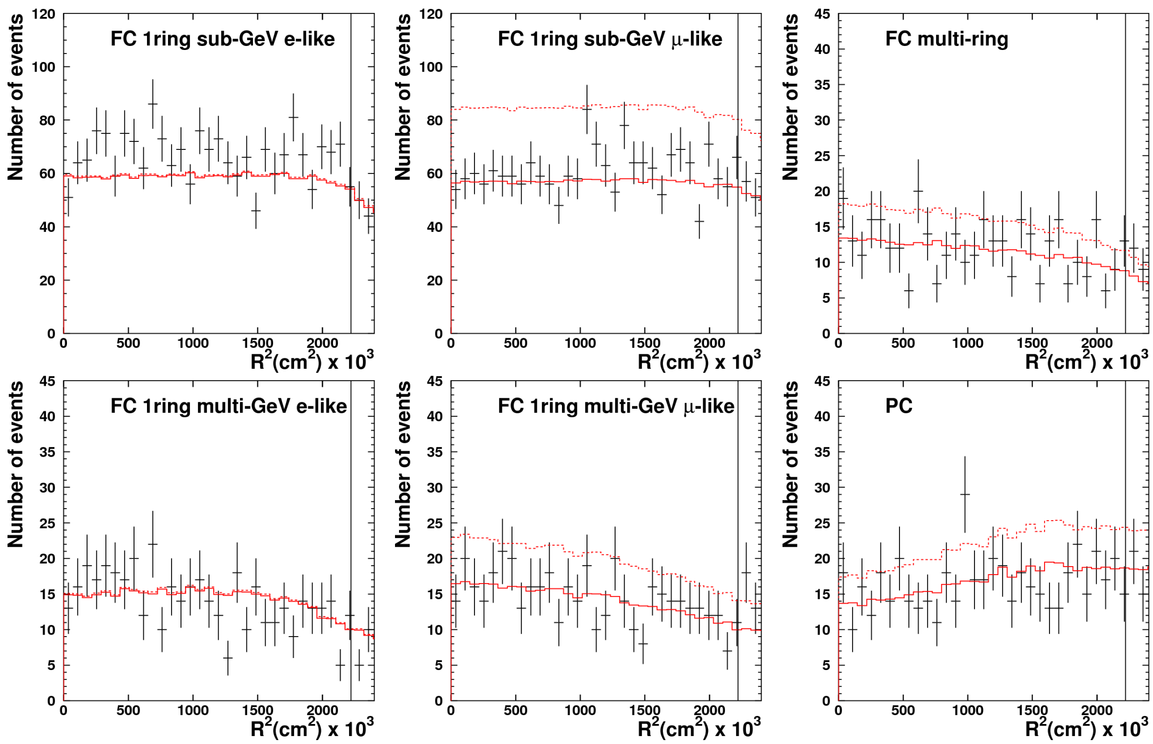

Figure B.4: Vertex for SK2 (R^2). Black dots are data, red solid line is oscillated Monte Carlo assuming 2 flavor $\nu_\mu \to \nu_\tau$ oscillation with $(\sin^2 2\theta, \Delta m^2) = (1.00, 2.5 \times 10^{-3} eV^2)$, red dashed line is unoscillated MC. Top row: FC Sub-GeV 1ring e-like, FC Sub-GeV 1ring μ-like, FC multi-ring μ-like. Bottom row: FC Multi-GeV 1-ring e-like, FC Multi-GeV 1ring μ-like, PC

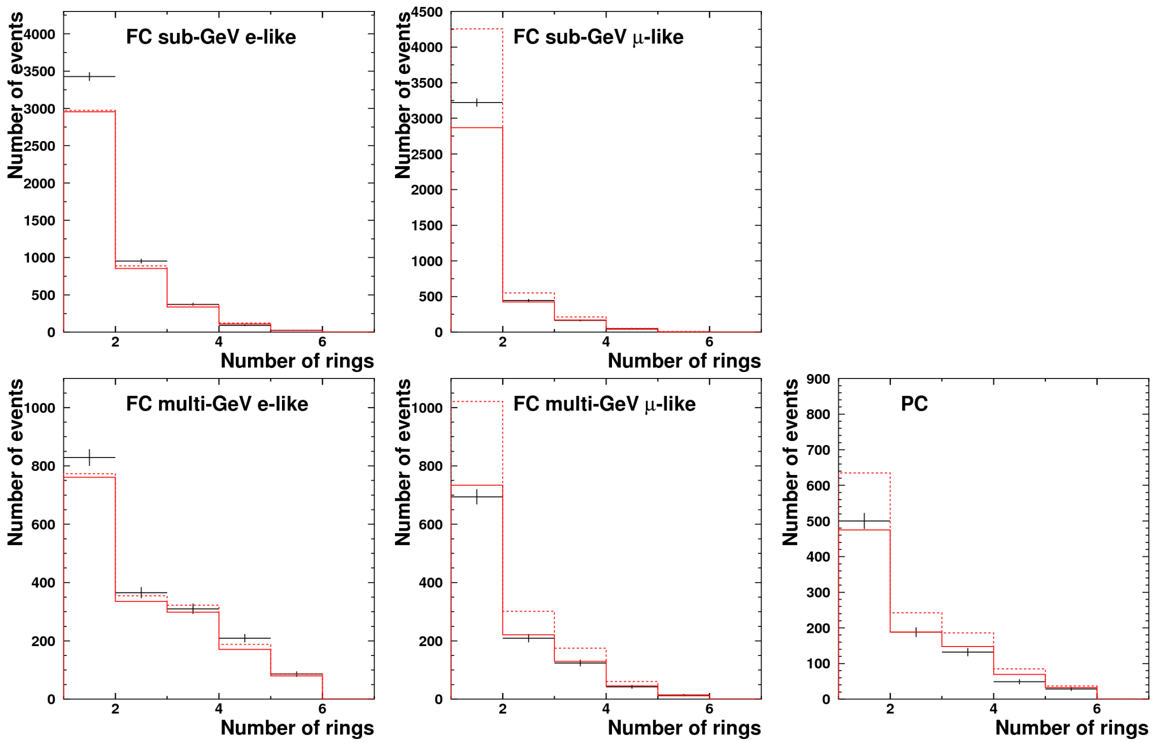

Figure B.5: Number of rings for SK1 . Black dots are data, red solid line is oscillated Monte Carlo assuming 2 flavor $\nu_\mu \rightarrow \nu_\tau$ oscillation with $(\sin^2 2\theta, \Delta m^2) = (1.00, 2.5 \times 10^{-3} eV^2)$, red dashed line is unoscillated MC. Top row: FC Sub-GeV 1ring e-like, FC Sub-GeV 1ring μ-like, FC multi-ring μ-like. Bottom row: FC Multi-GeV 1-ring e-like, FC Multi-GeV 1ring μ-like, PC

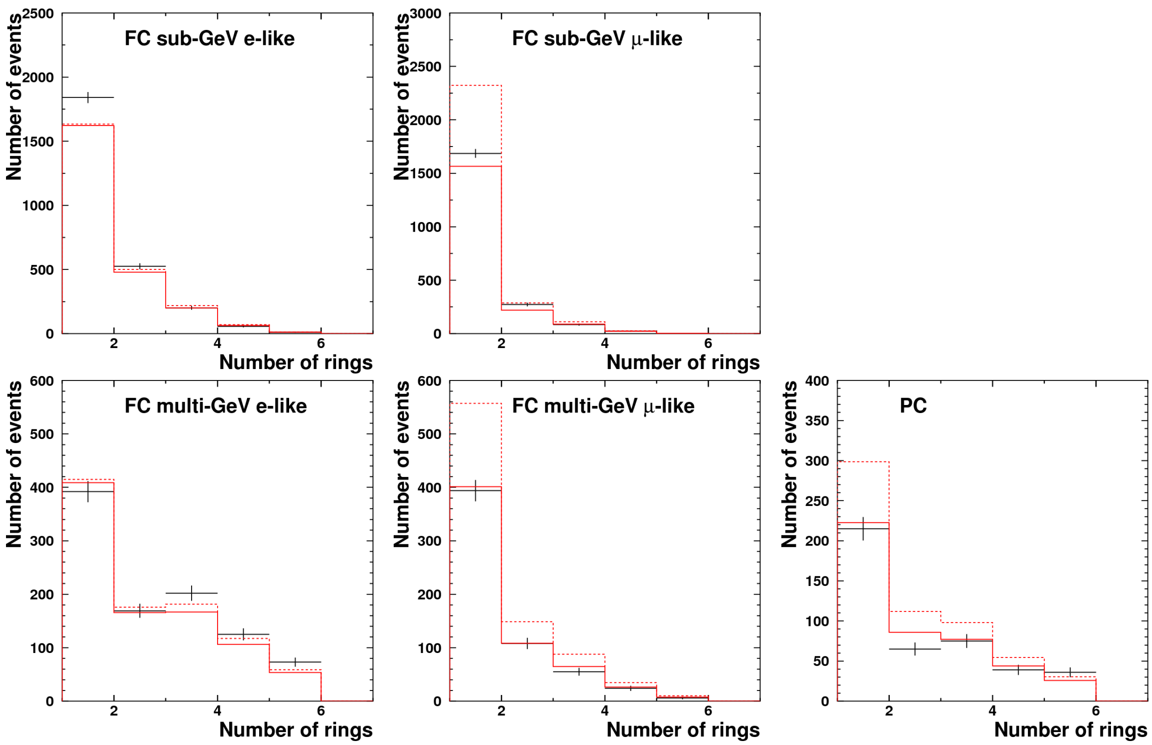

Figure B.6: Number of rings for SK2 . Black dots are data, red solid line is oscillated Monte Carlo assuming 2 flavor $\nu_\mu \rightarrow \nu_\tau$ oscillation with $(\sin^2 2\theta, \Delta m^2) = (1.00, 2.5 \times 10^{-3} eV^2)$, red dashed line is unoscillated MC. Top row: FC Sub-GeV 1ring e-like, FC Sub-GeV 1ring μ-like, FC multi-ring μ-like. Bottom row: FC Multi-GeV 1-ring e-like, FC Multi-GeV 1ring μ-like, PC

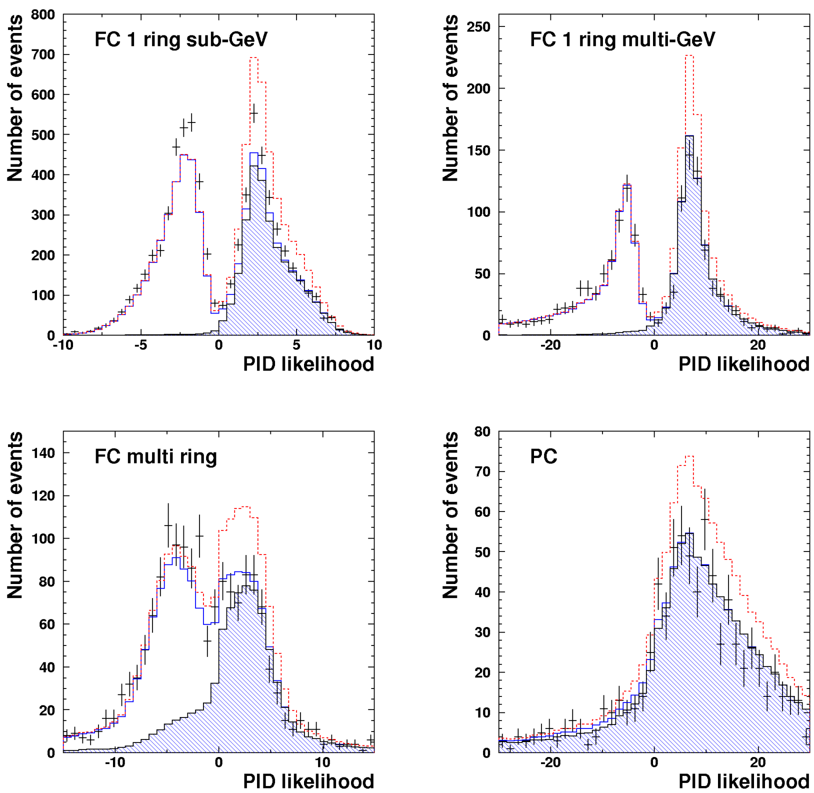

Figure B.7: PID likelihood for SK1 . Black dots are data, blue solid line is oscillated Monte Carlo assuming 2 flavor $\nu_\mu \rightarrow \nu_\tau$ oscillation with $(\sin^2 2\theta, \Delta m^2) = (1.00, 2.5 \times 10^{-3} eV^2)$, blue hatched are true $\mathrm{CC}\nu_\mu$ from oscillated MC, red dashed line is unoscillated MC. Top left: FC single rine sub-GeV. Top right: FC single ring multi-GeV. Bottom left: FC multi-ring, Bottom right: PC.

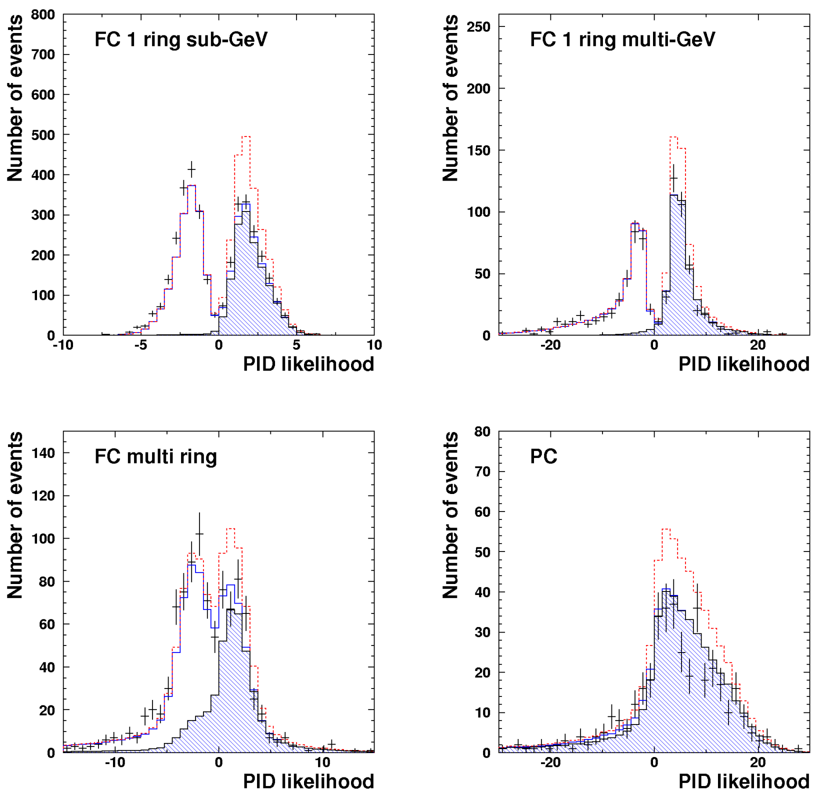

Figure B.8: PID likelihood for SK2 . Black dots are data, blue solid line is oscillated Monte Carlo assuming 2 flavor $\nu_\mu \to \nu_\tau$ oscillation with $(\sin^2 2\theta, \Delta m^2) = (1.00, 2.5 \times 10^{-3} eV^2)$, blue hatched are true CCν_μ from oscillated MC, red dashed line is unoscillated MC. Top left: FC single rine sub-GeV. Top right: FC single ring multi-GeV. Bottom left: FC multi-ring, Bottom right: PC.

Appendix C

Proof that binned and unbinned likelihood are equivalent

The goal of this Appendix is to show that using a binned or unbinned likelihood is identical if the same binned MC is used.

In our L/E analysis we use a binned likelihood which can be written as a reduced χ^2 (as in Eq. 9.2, Section 9.1):

$$\chi^2 = \sum_{i=1}^{nbin} \left[2(N_i^{exp}(1+\sum_{j=1}^{nsys} f_j^i \cdot \epsilon^j) - N_i^{obs}) - 2N_i^{obs} \ln \left(\frac{N_i^{obs}}{N_i^{exp}(1+\sum_{j=1}^{nsys} f_j^i \cdot \epsilon^j)} \right) \right] + \sum_j^{nsys} (\frac{\epsilon^j}{\sigma_j^{sys}})^2. \tag{C.1}$$

By assuming that the parameter ϵ^j are small, we can do a linear expansion of the χ^2 as a function of ϵ^j and this leads to the following set of linear equations (as in Eq. 9.3, where we kept only the linear terms):

$$\sum_{i=1}^{nbin} (N_i^{obs} - N_i^{exp}) f_k^i = \sum_{j=1}^{nsys} (\frac{\delta_{jk}}{\sigma^2} + \sum_{i=1}^{nbin} N_i^{obs} f_j^i f_k^i) \epsilon_k. \tag{C.2}$$

If instead of using a binned likelihood we wanted to use an unbinned likelihood, the definition of $\ln L$ is the following:

$$\begin{aligned}\ln L &= \left(\sum_{i}^{N^{obs}} \ln(N^{exp} \cdot P(x_i|\alpha))\right) - N^{exp}\\ &= \left(\sum_{i}^{N^{obs}} \ln(Q(x_i|\alpha))\right) - N^{exp},\end{aligned} \tag{C.3}$$

where Q is the non-normalized version of P. If our p.d.f P (and Q) are estimated using Monte Carlo, they will be binned. And if the binning of the Monte Carlo is the same as the binning that was applied to the data in the previous case then the following is true. We first apply the pull terms method to the unbinned likelihood and we get that: $Q_i = (1 + \sum_{i=k}^{nsys} f_k^i \cdot \epsilon^k) Q_i^0$. Then using the fact that the p.d.f Q is binned we can rewrite N^{exp} as follows:

$$\begin{aligned}N^{exp} &= \sum_{i=ibin}^{nbin} Q_{ibin}\\ &= \sum_{i=ibin}^{nbin} (1 + \sum_{i=k}^{nsys} f_k^{ibin} \cdot \epsilon^k) Q_{ibin}^0.\end{aligned} \tag{C.4}$$

So if we plug that back into Eq. C.3 and add the pull term $-\frac{1}{2}\sum_{k=1}^{nsys} \frac{\epsilon_k^2}{\sigma^2}$, we get

$$\ln L = \left[\sum_{i=1}^{Nobs} \ln(1 + \sum_{k=1}^{nsys} f_i^k \epsilon_k) + \ln Q_i^0\right] - \sum_{bin=1}^{nbin} (1 + \sum_{j=1}^{nsys} f_j^{bin} \epsilon_j) Q_{bin}^0 \tag{C.5}$$

$$- \frac{1}{2}\sum_{k=1}^{nsys} \frac{\epsilon_k^2}{\sigma^2}, \tag{C.6}$$

which leads to the following set of linear equations if we apply the same linear expansion as before:

$$\sum_{i=1}^{nobs} f_k^i - \sum_{bin=1}^{nbin} f_{bin}^k Q_{bin}^0 = \sum_{j=1}^{nsys} \Big(\frac{\delta_{jk}}{\sigma^2} + \sum_{i=1}^{nobs} f_j^i f_k^i)\epsilon_k. \tag{C.7}$$

Now since $Q_i^0 = N_i^{exp}$ and since you can write

$$\sum_{i=1}^{nobs} = \sum_{bin=1}^{nbin} \sum_{i=1}^{nobs} \delta_{i,bin} = \sum_{bin=1}^{nbin} N_{bin}^{obs}, \tag{C.8}$$

then the set of linear equation for the log likelihood becomes:

$$\sum_{bin=1}^{nbin} N_{bin}^{obs} f_k^{bin} - \sum_{bin=1}^{nbin} f_k^{bin} N_{bin}^{exp} = \sum_{k=1}^{nsys} \Big(\frac{\delta_{jk}}{\sigma^2} + \sum_{bin=1}^{nbin} N_{bin}^{obs} f_j^{bin} f_k^{bin})\epsilon_k, \tag{C.9}$$

which is the same as the set of linear equations obtained with the binned data and presented in Eq. C.2.

Appendix D

Use of a fully reconstructed charged current quasi-elastic (CCQE) sample

For quasi-elastic charged current interaction $\nu + n \rightarrow p + e^-$, our accuracy on the reconstruction of the energy and the flight length of the neutrino is limited by the fact that in most cases we do not see the recoiling proton coming from a neutrino interaction. If we were able to see the recoiling proton, our reconstruction of the energy and flight length would be more accurate. In some cases, the recoil proton is above Cherenkov threshold and if it is properly identified, we can collect a sample of events for which all the kinematics variables are known. In that case, the energy and the flight length of the incoming neutrino can be fully reconstructed. We call this sample the CCQE sample. Events with one or two rings are used in the CCQE event search. The tools used to identify the recoiling proton are based on Maxim Fechner's work [76].

D.1 Selecting the CCQE sample

For two rings events, in 97% of cases, it was found that the first ring found is the lepton and the second is the proton. We apply the following set of cuts to select the two-ring CCQE sample:

- First, we select events inside the L/E fiducial volume, with 2 fully-contained rings and with $100 < E_{vis} < 4000$ MeV.

- Then we use a cut designed to remove background from charged pions. By applying a linear cut on the proton-like momentum (momentum computed assuming that the particle is a proton) and track lengths: $A < P < B \times L(m) + C$ with $A = C =$ 1.1 GeV and $B = 7/6$ GeV/c/m, we can remove charged pions which typically have true momenta between 200 and 300 MeV/c and a proton-like momenta of 1.6 GeV/c, because their fitted path lengths are short ($\approx 20\ cm$) due to pion interactions.

- We then require that the opening angle of the second ring be less than 34° to select particle with low β.

- Then, we use a specific pattern likelihood. We ask that $\log(L_{lepton+proton}) - \log(L_{lepton+muon})$ be greater than zero.

- At this stage, there are still non-CCQE events coming from mis-identified pions. To remove these, we apply a kinematic cut. We ask that the quantity V^2 (where $V = P_p + P_l - P_n$) be around zero, since for a true CCQE event V is the 4-momentum of the neutrino and V^2 is the invariant mass of the neutrino. P_p, P_l, P_n are the 4-momenta of the proton, lepton and neutron respectively. We therefore select events which peak at $V^2 = 0$ by asking $-0.75 < V^2 < 1.5$ GeV/c^2.

Monte Carlo studies show that, for some events, the proton is missed by the standard fitter even if it is above Cherenkov threshold. These events only have one ring corresponding to the lepton track. We found that in these cases, the proton ring is weak but visible by eye-scan, and a dedicated ring finding algorithm was developed to find such events. Using this new ring algorithm and the pattern likelihood, we can build the estimator ΔL to decide whether an event is a true single-ring event, or if a proton above Cherenkov threshold was missed ($\Delta L = \log[\log(L_{lepton+proton}) - \log(L_{lepton\ alone})]$). A high value of the estimator corresponds to a proton track. To select the single-ring CCQE sample, we apply the following cuts:

- First, we select events inside the L/E fiducial volume, with 1 fully-contained ring and with $100 < E_{vis} < 4000$ MeV.
- Using the output of the proton pattern fitter on the new ring candidate, we apply $A < P < B \times L(m) + C$ with $A = C = 1.1$ GeV and $B = 7/6$ GeV/c/m. We also require that the track length L be greater than 2 m.
- The estimator Q_{dens} is based on the light distribution along the edge of a ring. It is used to decide if a ring was well fitter or not. We ask $\log Q_{dens} > 0$ to select good ring candidates.
- We ask that the ΔL pattern ID estimator be larger than 3.
- Finally, we ask that the V^2 quantity defined above be larger than 0.75 GeV/c^2.

D.2 Energy and flight length reconstruction for the CCQE sample

Once the selection of the CCQE sample is completed, we can fully reconstruct the energy and flight length using the kinematics of the interaction. We can then test if this fully reconstructed energy and flight length are more accurate than the standard reconstruction. In Fig. D.1 we present the reconstruction of the energy and the flight length and in Fig. D.2 we present the resulting L/E reconstruction. We can see that the energy of the single-ring events is usually reconstructed too low with the standard tools, as expected from missing the proton, and that this is very much improved when using the full CCQE reconstruction. The flight length reconstruction is also significantly improved by using the full kinematic reconstruction.

D.3 Statistics of the CCQE sample

We tested the use of the CCQE sample only on 100 years of SK1 MC. In Table D.1 we present the events that are identified as CCQE events and can be used in the L/E analysis. Out of the events that are found to be CCQE and inside the fiducial volumed defined for the L/E analysis and after we applied an energy cut on the 2-rings sample, if we select μ-like events, we expect 41 events in the 1-ring sample and 12 events in the 2-rings sample. For the 1-ring sample, out of the 41 events, 20 were passing the L/E resolution cut and were already included in the L/E analysis but with a worse energy and flight length reconstruction. The 21 other events are events that were not used before as they were failing the resolution cut. They can now be added since the energy and flight length resolution of the CCQE sample is much better. The same is true for the 2-rings sample, and 7 events are expected to be added. At this point it is important to notice that the identified CCQE sample account for only 2% of all L/E events, and therefore the effect of using this sample is expected to be very small, if even visible.

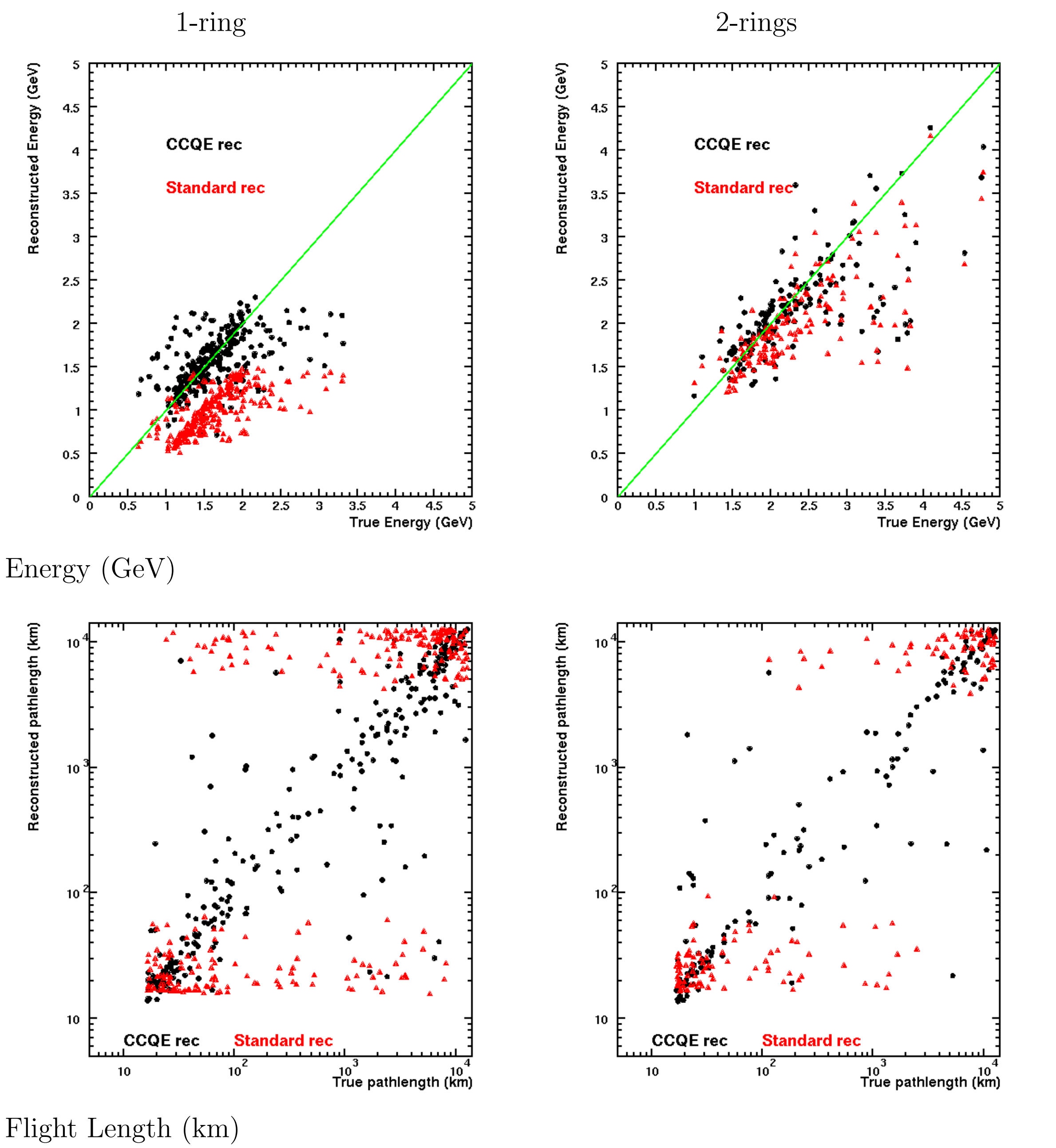

Figure D.1: Reconstructed versus true energy (top) and flight length (bottom) for events identified as CCQE and passing the L/E resolution cut. Black circles are events reconstructed with the CCQE full kinematics, while red triangles are the same events reconstructed with the standard L/E tools. The first column is for the 1-ring sample, while the second column is for the 2-rings sample.

1-ring 2-rings

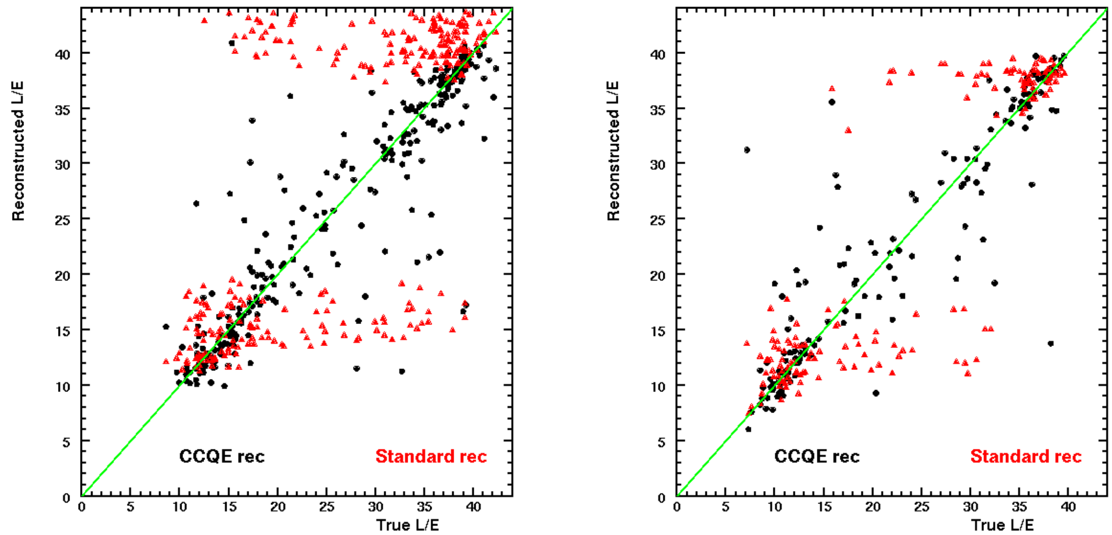

L/E bins

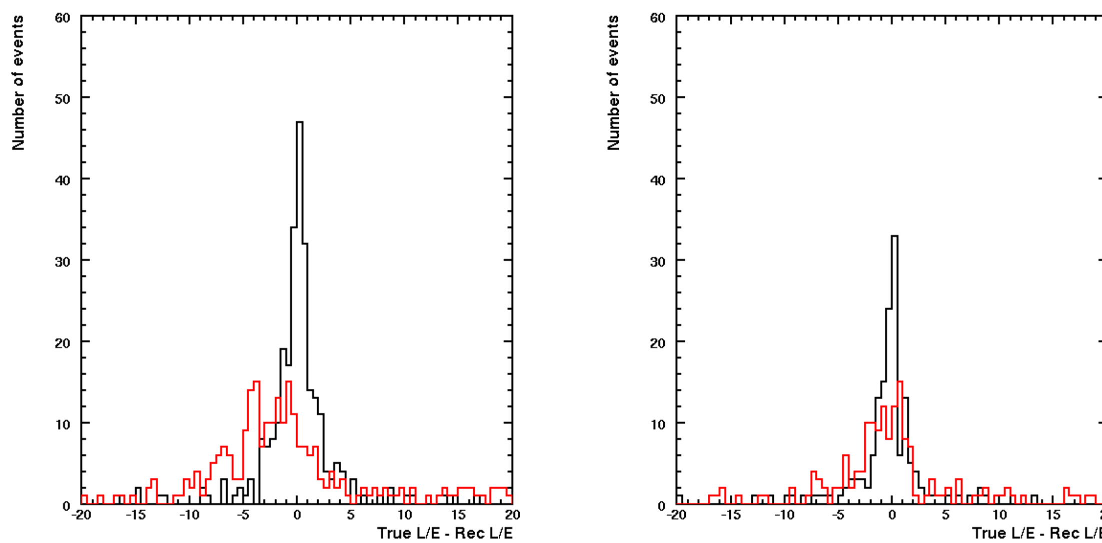

Resolution

Figure D.2: The top row is the reconstructed L/E bin versus the true L/E bin for events identified as CCQE and passing the L/E resolution cut. Black circles are events reconstructed with the CCQE full kinematics, while red triangles are the same events reconstructed with the standard L/E tools. The first column is for the 1-ring sample, while the second column is for the 2-rings sample. The bottom row is the true L/E bin minus the reconstructed L/E bin for the CCQE reconstruction (black) and the standard reconstruction (red).

	1-ring sample (MC)	2-rings sample (MC)
CCQE (FV for L/E)	58.99	52.67
$evis > 600$		21.92
μ-like	41.10	12.44
resolution cut < 0.7	19.68	6.61
total L/E events	2084.55	634.17

Table D.1: CCQE sample statistics, MC is normalized to 1489 days of livetime, and is not oscillated.

D.4 Testing the sensitivity of the CCQE sample

In order to test if adding the CCQE sample to the L/E analysis is useful, we compute a sensitivity curve for the regular L/E analysis and the L/E analysis with the CCQE sample. To compute the sensitivity curve, we create a set of fake data which agrees perfectly with an oscillated Monte Carlo and with the SK1 livetime. Such a set can be seen in Fig. D.3.

Then we apply the χ^2 fit to this set of fake data. Of course the value of the best fit χ^2 will be very low, but the contours represent the sensitivity achievable by the analysis. We applied this method to both the standard L/E analysis and the CCQE L/E analysis, where the events identified as CCQE have been reconstructed using the full kinematics of the interaction and for which the resolution cut was not applied. As you can see in Fig. D.4, the sensitivity of the CCQE L/E analysis is not distinguishable from the contours obtained with the standard L/E analysis. It was therefore decided not to add the CCQE sample to the L/E analysis.

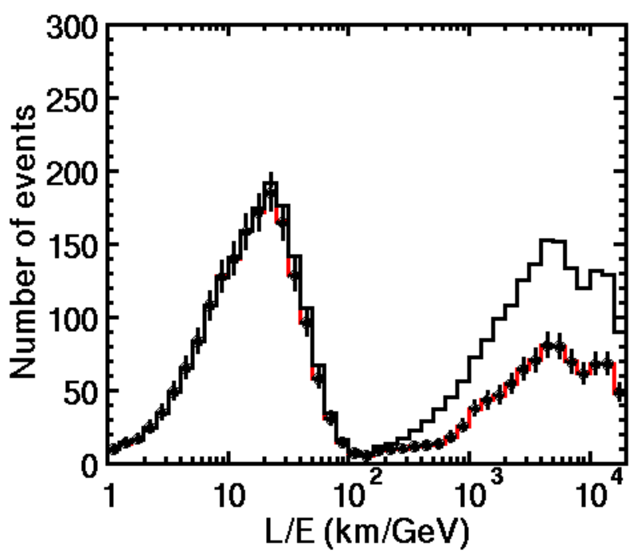

Figure D.3: Example of fake dataset (black dots) which agree perfectly with the oscillated Monte Carlo (red solid line). The unoscillated MC is also shown (black solid line).

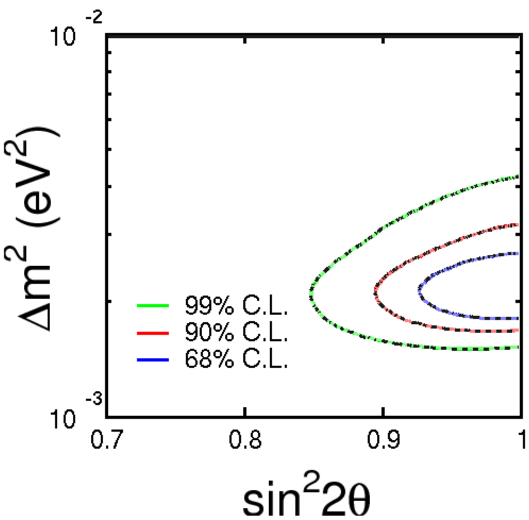

Figure D.4: Dashed lines are the results of the standard L/E analysis on the fake dataset, and colored lines are the results of the CCQE L/E analysis. No difference is observed.

List of Journal Abbreviation

Ann. Phys. .... Annals of Physics

AIP Conf. Proc .... American Institute of Physics Conference Proceedings

Astropart. Phys .... Astroparticle Physics

Astrophys. J. .... Astrophysical Journal

CERN .... Conseil Européen pour la recherche nucléaire

Eur. Phys. J. .... European Physical Journal

JHEP .... Journal of High Energy Physics

Los Alamos Sci. .... Los Alamos Scientific

New J. Phys. .... New Journal of Physics

Nucl. Instrum. Meth. .... Nuclear Instruments and Methods

Nucl. Phys. .... Nuclear Physics

Nucl. Phys. Proc. Suppl .... Nuceal Physics - Proceedings Supplements

Phys. Rept .... Physics Reports

Phys. Rev. .... Physical Review

Phys. Rev. Lett. .... Physical Review Letters

Prog. Theor. Phys .... Progress of Theoretical Physics

Rev. Mod. Phys .... Review of Modern Physics

Sov. Phys. JETP ... Soviet Physics, Journal of Experimental and Theoretical Physics

World Sci. Lect. Notes Phys. .... World Scientific Lectures Notes in Physics

Bibliography

[1] Super-Kamiokande, Y. Ashie *et al.*, hep-ex/0501064.

[2] Z. Maki, M. Nakagawa, and S. Sakata, Prog. Theor. Phys. **28**, 870 (1962).

[3] B. Pontecorvo, Sov. Phys. JETP **26**, 984 (1968).

[4] T. Schwetz, M. Tortola, and J. W. F. Valle, New J. Phys. **10**, 113011 (2008), 0808.2016.

[5] Y. Fukuda *et al.*, Nucl. Instrum. Meth. **A501**, 418 (2003).

[6] G. Mituska, *Study of non-standard neutrinos interactions with atmospheric neutrino data in Super-Kamiokande*, PhD thesis, University of Tokyo, 2009.

[7] W. Pauli, Letter to the physical society of tubingen (1930), reproduced in *physics today*, **31**,(9):23, 1978.

[8] F. Reines and C. L. Cowan, Phys. Rev. **90**, 492 (1953).

[9] G. Danby *et al.*, Phys. Rev. Lett. **9**, 36 (1962).

[10] DONUT, K. Kodama *et al.*, Phys. Lett. B **204**, 218 (2001), hep-ex/0012035.

[11] B. T. Cleveland *et al.*, Astrophys. J. **496**, 505 (1998).

[12] J. N. Bahcall and R. K. Ulrich, Rev. Mod. Phys. **60**, 297 (1988).

[13] Kamiokande-II, K. S. Hirata *et al.*, Phys. Lett. B **280**, 146 (1992).

[14] R. Becker-Szendy *et al.*, Nucl. Phys. Proc. Suppl. **38**, 331 (1995).

[15] F. Halzen and A. D. Martin, *Quarks and leptons: an introductory course in modern particle physics* .

[16] S. L. Glashow, in *Quarks and Leptons, Cargese 1979*, p. 707, 1980.

[17] M. Gell-Mann, P. Ramond, and R. Slansky, *Supergravity* (, 1979).

[18] R. N. Mohapatra and G. Senjanović, Phys. Rev. Lett. **44**, 912 (1980).

[19] T. Yanagida, Horizontal symmetry and masses of neutrinos, in *Proceedings of the Workshop on Unified Theory and the Baryon Number of the Universe*, p. 95, KEK, Japan, 1979.

[20] B. Kayser, F. Gibrat-Debu, and F. Perrier, World Sci. Lect. Notes Phys. **25**, 1 (1989).

[21] R. Slansky, S. Raby, J. T. Goldman, and G. Garvey, Los Alamos Sci. **25**, 28 (1997).

[22] N. Cabibbo, Phys. Rev. Lett. **10**, 531 (1963).

[23] M. Kobayashi and T. Maskawa, Progress of Theoretical Physics **49**, 652 (1973).

[24] F. Boehm and P. Vogel, *Physics of Massive Neutrinos* (Cambridge University Press, 1992).

[25] A. G. Cohen, S. L. Glashow, and Z. Ligeti, (2008), arXiv 0810.4602.

[26] R. N. Mohapatra and W. Rodejohann, Phys. Rev. **D72**, 053001 (2005), hep-ph/0507312.

[27] MINOS, P. Adamson *et al.*, Phys. Rev. Lett. **101**, 131802 (2008), 0806.2237.

[28] CHOOZ, M. Apollonio *et al.*, Phys. Lett. **B466**, 415 (1999), hep-ex/9907037.

[29] T2K, Y. Itow *et al.*, (2001), hep-ex/0106019.

[30] Double Chooz, F. Ardellier *et al.*, (2006), hep-ex/0606025.

[31] M. Ishitsuka, T. Kajita, H. Minakata, and H. Nunokawa, Phys. Rev. **D72**, 033003 (2005), hep-ph/0504026.

[32] V. Barger *et al.*, Phys. Rev. **D74**, 073004 (2006), hep-ph/0607177.

[33] J. E. Campagne, M. Maltoni, M. Mezzetto, and T. Schwetz, JHEP **04**, 003 (2007), hep-ph/0603172.

[34] LSND, A. Aguilar *et al.*, Phys. Rev. **D64**, 112007 (2001), hep-ex/0104049.

[35] MiniBooNE, A. A. Aguilar-Arevalo *et al.*, Phys. Rev. Lett. **100**, 032301 (2008), 0706.0926.

[36] Super-Kamiokande, S. Fukuda *et al.*, Phys. Rev. Lett. **86**, 5656 (2001), hep-ex/0103033.

[37] SNO, Q. R. Ahmad *et al.*, Phys. Rev. Lett. **89**, 011301 (2002), nucl-ex/0204008.

[38] Borexino, C. Arpesella *et al.*, Phys. Lett. **B658**, 101 (2008), 0708.2251.

[39] KamLAND, S. Abe *et al.*, Phys. Rev. Lett. **100**, 221803 (2008), 0801.4589.

[40] K2K, E. Aliu *et al.*, Phys. Rev. Lett. **94**, 081802 (2005), hep-ex/0411038.

[41] R. Claus *et al.*, Nucl. Instrum. Meth. **A261**, 540 (1987).

[42] R. Becker-Szendy *et al.*, Nucl. Instrum. Meth. **A324**, 363 (1993).

[43] Hamamatsu website `http://www.hamamatsu.com/`.

[44] M. Honda, T. Kajita, K. Kasahara, S. Midorikawa, and T. Sanuki, Phys. Rev. **D75**, 043006 (2007), astro-ph/0611418.

[45] G. Battistoni, A. Ferrari, T. Montaruli, and P. R. Sala, Astropart. Phys. **19**, 269 (2003), hep-ph/0207035.

[46] G. D. Barr, T. K. Gaisser, P. Lipari, S. Robbins, and T. Stanev, Phys. Rev. **D70**, 023006 (2004), astro-ph/0403630.

[47] M. Ishitsuka, *L/E analysis of the atmospheric neutrino data from Super-Kamiokande*, PhD thesis, University of Tokyo, 2004.

[48] Y. Hayato, Nucl. Phys. Proc. Suppl. **112**, 171 (2002).

[49] G. Mitsuka, AIP Conf. Proc. **981**, 262 (2008).

[50] G. Mitsuka, AIP Conf. Proc. **967**, 208 (2007).

[51] C. H. Llewellyn Smith, Phys. Rept. **3**, 261 (1972).

[52] R. A. Smith and E. J. Moniz, Nucl. Phys. **B43**, 605 (1972).

[53] D. H. Perkins, *Introduction to high energy physics* , Reading 1972, 353p.

[54] K2K, R. Gran *et al.*, Phys. Rev. **D74**, 052002 (2006), hep-ex/0603034.

[55] X. Espinal and F. Sanchez, AIP Conf. Proc. **967**, 117 (2007).

[56] J. Reich *et al.*, Nucl. Instrum. Meth. **A440**, 535 (2000).

[57] D. Rein and L. M. Sehgal, Ann. Phys. **133**, 79 (1981).

[58] M. Gluck, E. Reya, and A. Vogt, Eur. Phys. J. **C5**, 461 (1998), hep-ph/9806404.

[59] A. Bodek and U. K. Yang, (2003), hep-ex/0308007.

[60] T. Sjostrand, CERN-TH-7112-93.

[61] D. Rein and L. M. Sehgal, Nucl. Phys. **B223**, 29 (1983).

[62] K2K, M. Hasegawa *et al.*, Phys. Rev. Lett. **95**, 252301 (2005), hep-ex/0506008.

[63] D. Rein and L. M. Sehgal, Phys. Lett. **B657**, 207 (2007), hep-ph/0606185.

[64] Geant detector description and simulation tool, 1993, CERN Program Library Long Writeup W5013.

[65] C. Zeitnitz and T. A. Gabriel, Nucl. Instrum. Meth. **A349**, 106 (1994).

[66] Y. Takenaga, *Atmospheric neutrino oscillation analysis with solar terms in Super-Kamiokande*, PhD thesis, University of Tokyo, 2008.

[67] W. Wang, *Study of non-standard effects in neutrino oscillations at Super-Kamiokande*, PhD thesis, Boston University, 2007.

[68] E. R. Davies, *Machine Vision: Theory, Algorithms, Practicalities* (Morgan Kaufmann Publishers Inc., San Francisco, CA, USA, 2004).

[69] S. T. Clark, *Searches for proton decay with the Super-Kamiokande detector*, PhD thesis, Boston University, 2007.

[70] Soudan 2, M. C. Sanchez *et al.*, Phys. Rev. **D68**, 113004 (2003), hep-ex/0307069.

[71] V. D. Barger, J. G. Learned, S. Pakvasa, and T. J. Weiler, Phys. Rev. Lett. **82**, 2640 (1999), astro-ph/9810121.

[72] D. A. Krakauer *et al.*, Phys. Rev. **D44**, 6 (1991).

[73] E. Lisi, A. Marrone, and D. Montanino, Phys. Rev. Lett. **85**, 1166 (2000), hep-ph/0002053.

[74] G. L. Fogli, E. Lisi, A. Marrone, D. Montanino, and A. Palazzo, Phys. Rev. **D66**, 053010 (2002), hep-ph/0206162.

[75] Particle Data Group, R. M. Barnett *et al.*, Phys. Rev. **D54**, 1 (1996).

[76] Super-Kamiokande, M. Fechner *et al.*, (2009), arXiv 0901.1645.

Curriculum Vitae

Fanny Dufour

590 Commonwealth Avenue	**Mobile:** + 1-617-888-0075
Department of Physics, Boston University	**Office:** + 1-617-353-6040
Boston, MA 02215, U.S.A.	**E-mail:** fdufour@bu.edu

EDUCATION

- Boston University, Boston, U.S.A.
  - **Ph.D.** in Physics, expected in May 2009
- Université Libre de Bruxelles, Brussels, Belgium
  - **Bachelor of Science** in Physics, June 2003, *La plus grande Distinction*

RESEARCH EXPERIENCE

- Super-Kamiokande
  - Detector hardware work: Installation of outer detector reflector
  - Monte Carlo work: tuning of the outer detector simulation; generation of 60 years of Nuance MC
  - Data processing: reduction of partially contained neutrino events and studies of associated systematic uncertainties
  - Physics analysis: L/E oscillation analysis
- T2KK and Long baseline neutrino experiments

- Physics analysis: Likelihood study to remove neutral pion background events from electron neutrino appearance signal; Study of off-axis sensitivity of the Korean detector in the T2KK framework
- Physics analysis: Comparison of the T2KK setup and the FNAL wide-band beam proposal, using the same analysis framework.

PRESENTATIONS

- **Sensitivity of the JPARC-Kamioka-Korea setup with 2 Water Cerenkov detectors**

  CHIPP 2008

  Zurich, Switzerland, Nov 17 - 18, 2008

- **T2KK**

  NOW 2008

  Lecce, Italy, Sept 6 - 13, 2008

- **CP Violation Physics at a J-PARC Beam - Water Cherenkov Detector Case**

  NP08

  Mito, Japan, March 5 - 7, 2008

- **Wide-band beam studies for T2KK**

  3rd International Workshop on a Far Detector in Korea for the J-PARC Neutrino Beam

  Tokyo University, Tokyo, Japan, Sept 30 - Oct 1, 2007

- **T2KK and Examination of Water Detector Capability**

  FNAL/BNL joint study group for long baseline neutrino experiments,

  Fermilab, U.S.A., September 16 - 17, 2006

- **T2KK sensitivity as a function of off-axis angle**

  2nd International Workshop on a Far Detector in Korea for the J-PARC Neutrino Beam

  Seoul National University, Seoul, Korea, July 13 - 14, 2006

- **Signal and background separation with 20 and 40% photo coverage of a large Cherenkov detector**

  2nd International Workshop on a Far Detector in Korea for the J-PARC Neutrino Beam

  Seoul National University, Seoul, Korea, July 13 - 14, 2006

SELECTED PUBLICATIONS

- **Study of the T2KK setup with several off-axis angles of the Korean detector and new systematic errors**

  F. Dufour, T. Kajita, E. Kearns and K. Okumura

  In preparation

- **Report of the US long baseline neutrino experiment study**

  V. Barger *et al.*

  arXiv:0705.4396 [hep-ph].

OTHER PUBLICATIONS

as a member of the Super-Kamiokande collaboration

- **Solar neutrino measurements in Super-Kamiokande-II**

  J. P. Cravens *et al.*

  Phys. Rev. D **78**, 032002 (2008)

  arXiv:0803.4312 [hep-ex]

- **Search for Matter-Dependent Atmospheric Neutrino Oscillations in Super-Kamiokande**

K. Abe *et al.*

Phys. Rev. D **77**, 052001 (2008)

arXiv:0801.0776 [hep-ex]

- **Study of TeV Neutrinos with Upward Showering Muons in Super-Kamiokande**

  S. Desai *et al.*

  Astropart. Phys. **29**, 42 (2008)

  arXiv:0711.0053 [hep-ex]

- **Search for Supernova Neutrino Bursts at Super-Kamiokande**

  M. Ikeda *et al.*

  Astrophys. J. **669**, 519 (2007)

  arXiv:0706.2283 [astro-ph]

- **Search for neutral Q-balls in Super-Kamiokande II**

  Y. Takenaga *et al.*

  Phys. Lett. B **647**, 18 (2007)

  arXiv:hep-ex/0608057

- **A measurement of atmospheric neutrino flux consistent with tau neutrino appearance**

  K. Abe *et al.*

  Phys. Rev. Lett. **97**, 171801 (2006)

  arXiv:hep-ex/0607059

- **Search for diffuse astrophysical neutrino flux using ultra-high energy upward-going muons in Super-Kamiokande I**

  M. E. C. Swanson *et al.*

Astrophys. J. **652**, 206 (2006)

arXiv:astro-ph/0606126

TEACHING EXPERIENCE

- Boston University, Boston, U.S.A.
  - Discussion session tutor of college physics, September 2003 – June 2004
- Université Libre de Bruxelles, Brussels, Belgium
  - Office hours teaching assistant physics, September 2002 – December 2002

HONORS AND AWARDS

- **Gertrude and Maurice Goldhaber Prize**, Boston University, Boston, U.S.A., 2005
- **BAEF fellowship** for Belgian Graduate Students in the U.S.A., Brussels, Belgium, 2003

ORGANIZATIONS

- Member of the Physics Graduate Students Committee of Boston University, 2005-2009
- Founding member of the Women in Physics association at Boston University, 2006-2009

REFERENCES

- Professor Edward Kearns
  Department of Physics, Boston University
  E-mail: kearns@budoe.bu.edu; Office Phone: + 1-617-353-3425

- Professor Kate Scholberg

  Department of Physics, Duke University

  E-mail: schol@phy.duke.edu ; Office Phone: + 1-919-660-2962

- Professor Takaaki Kajita

  Institute for Cosmic Ray Research, University of Tokyo

  E-mail: kajita@icrr.u-tokyo.ac.jp ; Office Phone: + 81-4-7136-3100